

Novel Concepts for Functional High Resolution Microscopy

THÈSE N° 5177 (2011)

PRÉSENTÉE LE 30 SEPTEMBRE 2011

À LA FACULTÉ SCIENCES ET TECHNIQUES DE L'INGÉNIEUR

LABORATOIRE D'OPTIQUE BIOMÉDICALE

PROGRAMME DOCTORAL EN PHOTONIQUE

ÉCOLE POLYTECHNIQUE FÉDÉRALE DE LAUSANNE

POUR L'OBTENTION DU GRADE DE DOCTEUR ÈS SCIENCES

PAR

Matthias GEISSBÜHLER

acceptée sur proposition du jury:

Prof. C. Moser, président du jury

Prof. T. Lasser, directeur de thèse

Dr L. Bonacina, rapporteur

Dr C. Eggeling, rapporteur

Prof. J.-E. Moser, rapporteur



ÉCOLE POLYTECHNIQUE
FÉDÉRALE DE LAUSANNE

Suisse
2011

I do not know what I may appear to the world,
but to myself I seem to have been only like a boy
playing on the sea-shore, and diverting myself in
now and then finding a smoother pebble or a
prettier shell than ordinary, whilst the great ocean
of truth lay all undiscovered before me.

Sir Isaac Newton (1642 - 1727)

Abstract

Functional imaging of biological cells and organs is one of the key techniques that drives new discoveries in life science research and medicine. In this thesis novel concepts for functional imaging at high spatial and temporal resolution are presented. In the first part, an imaging modality named Triplet Lifetime Imaging is developed. The technique allows oxygen consumption within single cells to be monitored at sub-cellular resolution. Measurement of tissue and cell oxygenation is important in order to understand cell metabolism. The method exploits oxygen induced triplet lifetime changes. The technique is applied to a biological cell system, employing as reporter a cytosolic fusion protein of β -galactosidase SNAP-tag labeled with TMR. Oxygen consumption in single smooth muscle cells A7r5 during an [Arg⁸]-vasopressin (AVP) induced contraction is measured. The results indicate a consumption leading to an intracellular oxygen concentration that decays mono-exponentially with time. The proposed method has the potential to become a new tool for investigating oxygen metabolism at the single cell and sub-cellular level. The method is further applied to various other biological systems, demonstrating its versatility and the usefulness of this novel imaging modality.

In the second part of this thesis, a concept for optical spectroscopy named nonlinear correlation spectroscopy (NLCS) is developed. The method allows monitoring of diffusing and flowing nanoparticles made of nonlinear optical material. NLCS is a method related to fluorescence correlation spectroscopy (FCS), but instead of fluorescence intensity fluctuations, NLCS analyses coherent field fluctuations of the second and third harmonic light. In bulk material, the third harmonic contribution vanishes due to the destructive interference of the third harmonic light generated in front of and behind of the focal field (Guoy phase shift). On the other hand, nanoparticles with dimensions comparable or smaller than the focal volume can generate strong higher harmonic signals. Particles based on non-centrosymmetric non-linear materials such as KNbO₃ have been found to show a strong second and third harmonic signal. The method and the theory are introduced and NLCS results for diffusing polystyrene spheres (PS) as well as KNbO₃ particles are presented. These spectroscopic results open the door for future extension into imaging concepts.

Keywords: Microscopy; *in vivo* imaging; functional imaging; fluorescence; triplet state lifetime; Modulated Excitation; Triplet Lifetime Imaging; Transient State Imaging (TRAST); oxygen

concentration; oxygen consumption; super-resolution; optical spectroscopy; fluorescence correlation spectroscopy (FCS); nonlinear correlation spectroscopy (NLCS); third-harmonic generation (THG); second-harmonic generation (SHG); nonlinear optics

Zusammenfassung

Funktionelle Bildgebung von biologischen Zellen und Organen ist eine der wichtigsten Techniken, die neue Entdeckungen in der biowissenschaftlichen Forschung und Medizin unterstützt. In dieser Doktorarbeit werden neue Konzepte für die funktionelle Bildgebung in hoher räumlicher und zeitlicher Auflösung beschrieben. Im ersten Teil wird ein bildgebendes Verfahren namens „Triplet Lifetime Imaging“ entwickelt. Die Technik ermöglicht den Sauerstoffverbrauch in einzelnen Zellen mit subzellulärer Auflösung zu ermitteln. Die Messung der Sauerstoffversorgung von Geweben und Zellen ist wichtig, um den Zellstoffwechsel besser zu verstehen. Das Verfahren nutzt Sauerstoff-induzierte Triplettlebensdauer Veränderungen. Die Technik wurde auf eine biologische Zelle angewandt, wobei als Sensor ein cytosolisches Fusionsprotein (β -Galactosidase) eingesetzt wurde, welches mittels SNAP-tag mit TMR markiert wurde. Der Sauerstoffverbrauch in einzelnen glatten Muskelzellen A7r5 wurde während einer [Arg⁸]-Vasopressin (AVP) induzierten Kontraktion gemessen. Die Ergebnisse zeigen, dass auf Grund des Verbrauches, die Sauerstoffkonzentration mono-exponentiell mit der Zeit abnimmt. Die vorgeschlagene Methode hat das Potenzial, ein neues Werkzeug für die Untersuchung vom Sauerstoff-Stoffwechsel in der Zelle und auf sub-zellulärer Ebene zu werden. Um die Vielseitigkeit und den Nutzen dieses neuartigen bildgebenden Verfahrens zu zeigen, wurde das Verfahren ausserdem auf verschiedene andere biologische Systeme angewandt.

Im zweiten Teil dieser Arbeit wird ein Konzept für die optische Spektroskopie genannt nichtlineare Korrelations-Spektroskopie (NLCS) entwickelt. Die Methode ermöglicht die Diffusion fließender Nanopartikel aus nichtlinearen optischen Materialien zu ermitteln. NLCS ist eine Methode, die im Zusammenhang mit Fluoreszenz-Korrelations-Spektroskopie (FCS) steht. Anstatt der Fluktuationen in der Fluoreszenzintensität werden mit NLCS Fluktuationen des kohärenten Feldes des frequenz verdoppelten sowie frequenz verdreifachten Lichts analysiert. Die dritte Harmonische, verschwindet normalerweise beim Fokussieren in grössere optische Objekte aufgrund der destruktiven Interferenz des frequenzverdreifachten Lichtes, welches vor und hinter dem Fokusfeld generiert wird (Guoy Phasenverschiebung). Nanopartikel erzeugen hingegen starke frequenzvervielfachte Signale, falls ihre Abmessungen vergleichbar oder kleiner sind als das fokale Volumen. Für den Fall von Partikeln aus nicht-zentrosymmetrischen nicht-linearen Materialien wie KNbO_3 konnte eine starke Frequenzverdoppelung sowie auch -verdreifachung gemessen werden. Die Methode und die Theorie werden eingeführt und

NLCS Ergebnisse für die Diffusion von Polystyrol-Kugeln (PS) sowie KNbO_3 Partikeln gezeigt. Diese spektroskopischen Ergebnisse erschliessen zukünftige Erweiterungen in Bildgebungsverfahren.

Stichworte: Mikroskopie; *in vivo* Bildgebung; funktionelle Bildgebung; Fluoreszenz; Triplett Lebensdauer; Modulierte Anregung; Triplet Lifetime Imaging; Transient State Imaging (TRAST); Sauerstoffkonzentration; Sauerstoffverbrauch; hochauflösende Mikroskopie; optische Spektroskopie; Fluoreszenz-Korrelations-Spektroskopie (FCS); nichtlineare Korrelations-Spektroskopie (NLCS); Frequenzverdoppelung; Frequenzverdreifachung; nichtlineare Optik

Résumé

L'imagerie fonctionnelle de cellules biologiques et d'organes est l'une des techniques clés qui amène de nouvelles découvertes dans la recherche en sciences de la vie et en médecine. Dans cette thèse sont présentés de nouveaux concepts d'imagerie fonctionnelle à haute-résolution spatiale et temporelle. Dans la première partie, une méthodologie d'imagerie appelée « Triplet lifetime Imaging » est développée. Cette technique permet de visualiser la consommation d'oxygène au sein de cellules individuelles à une résolution sub-cellulaire. La mesure de l'oxygénation des tissus et des cellules est importante afin de comprendre le métabolisme cellulaire. Cette méthode utilise les variations de la durée de vie de l'état triplet induit par la concentration d'oxygène. La technique est appliquée à un système de cellules biologiques, employant en tant que capteur une protéine de fusion cytosolique β -galactosidase avec SNAP-tag marqué avec TMR. La consommation d'oxygène de cellules musculaire lisse A7r5 est mesurée durant une contraction induite par la molécule [Arg⁸]-vasopressine (AVP). Les résultats indiquent une consommation menant à une concentration intracellulaire d'oxygène qui décroît de manière mono-exponentielle au court du temps. La méthode proposée a le potentiel de devenir un nouvel outil pour étudier le métabolisme de l'oxygène au niveau cellulaire et sub-cellulaire. La méthode est en outre appliquée à divers autres systèmes biologiques, démontrant sa polyvalence et l'utilité de cette nouvelle modalité d'imagerie.

Dans la deuxième partie de cette thèse, un concept pour la spectroscopie optique est développé, appelé spectroscopie non-linéaire par corrélation (NLCS). Cette méthode permet de mesurer la diffusion et le flux de nanoparticules issues de matériau optique non linéaire. NLCS est une méthode liée à la spectroscopie par corrélation de fluorescence (FCS), mais au lieu de fluctuations d'intensité de fluorescence, NLCS analyse les fluctuations du champ cohérent de la lumière de deuxième et troisième harmonique. Normalement en focalisant dans de la matière optique, la contribution de la troisième harmonique disparaît à cause de l'interférence destructive de la troisième harmonique générée à l'avant et à l'arrière du champ focal (déphasage Guoy). D'autre part, les nanoparticules avec des dimensions comparables ou plus petits que le volume focal peuvent générer de forts signaux d'harmonies supérieures. Des particules basées sur des matériaux non-centrosymétrique non-linéaire tels que le KNbO_3 ont démontré un signal fort de deuxième ainsi que de troisième harmonique. Après l'introduction

de la méthode et la théorie, nous montrons des résultats NLCS pour la diffusion de sphères de polystyrène (PS) ainsi que des particules de KNbO_3 . Ces résultats spectroscopiques ouvrent la porte à de futurs développements de concepts d'imagerie.

Mots-clés : microscopie ; imagerie *in vivo* ; imagerie fonctionnelle ; fluorescence ; temps de vie de l'état triplet ; excitation modulée ; tétraméthylrhodamine (TMR) ; Triplet Lifetime Imaging ; Imagerie d'états transitoires (TRAST) ; concentration d'oxygène ; consommation d'oxygène ; haute résolution ; spectroscopie optique ; spectroscopie par corrélation de fluorescence (FCS) ; spectroscopie non linéaire par corrélation (NLCS) ; génération d'harmoniques supérieurs ; optique non linéaire

Contents

Abstract (English/Français/Deutsch)	v
Table of contents	xiii
List of figures	xvi
List of tables	xvi
1 Introduction	1
1.1 Triplet Lifetime Imaging	2
1.2 Non-linear correlation spectroscopy (NLCS)	4
I Triplet Lifetime Imaging	7
2 Molecular fluorescence under modulated excitation	9
2.1 Photochemistry of fluorescent molecules	9
2.1.1 Triplet state vs Singlet state	11
2.1.2 Interaction with molecular oxygen	12
2.2 Simplified three state model	15
2.2.1 Derivation of an analytical model	16
2.3 Fluorescence emission under modulated excitation	18
2.4 The ideal fluorophore	19
2.4.1 Discussion	23
3 Triplet lifetime imaging: The method	27
3.1 Setup	27
3.1.1 AOM	28
3.1.2 Phase contrast	30
3.1.3 Bleaching	31
3.1.4 Image acquisition parameters	32
3.2 Image processing	34
3.2.1 Image display	36
3.3 Model system: TMR on cover slide	37

Contents

4	Triplet lifetime imaging applications	39
4.1	Oxygen consumption imaging	39
4.1.1	Calibration experiment: triplet lifetime versus oxygen concentration . . .	40
4.1.2	Smooth muscle cells from rat thoracic aorta (A7r5)	42
4.1.3	Averaging of the data	43
4.1.4	Triplet lifetime results	44
4.2	Assessing the cellular uptake mechanism	49
4.2.1	Materials and Methods	49
4.2.2	Results and discussion	51
4.3	Fluorophore-DNA-complexes	54
4.3.1	Materials and Methods	54
4.3.2	Results and discussion	56
5	Triplet SOFI - superresolution based on modulated excitation	57
5.1	Theory	58
5.2	The ideal fluorophore	59
5.3	Conclusion	60
II	Nonlinear correlation spectroscopy	63
6	Nonlinear correlation spectroscopy: Theory	65
6.1	Non-linear optics	65
6.1.1	Higher harmonic generation by a focussed beam	66
6.1.2	Second and third harmonic generation by small particles	70
6.2	Coherent correlation spectroscopy	72
6.2.1	Coherent correlation spectroscopy with flow components	76
6.2.2	Estimation of flow velocities due to optical forces	78
7	Nonlinear correlation spectroscopy (NLCS) - Setup and Experiments	81
7.1	Mode-locked Cr:forsterite laser	81
7.2	Nonlinear correlation spectroscopy setup	83
7.3	Nonlinear correlation spectroscopy (NLCS) results	87
7.3.1	Materials	87
7.3.2	NLCS artifact removal	87
7.3.3	Polystyrene spheres diffusion	88
7.3.4	KNbO ₃ -nanoparticle diffusion observed in SHG and THG	90
7.3.5	Conclusion	92
III	Afterword	93
8	Conclusion and Outlook	95
8.1	Triplet Lifetime Imaging	95

8.2 Nonlinear correlation spectroscopy	96
9 Acknowledgements	99
 IV Appendix	 103
A Triplet lifetime imaging: Derivation of average fluorescence intensity	105
B Nonlinear correlation spectroscopy - Autocorrelation theory	111
B.1 Solution for pure diffusion ($V = 0$)	116
B.2 Solution for diffusion with flow ($V \neq 0$)	118
C Colormaps (Lookup-tables)	121
Bibliography	124
Curriculum Vitae	139

List of Figures

1.1	Schematic drawing of an eukaryotic animal cell	3
2.1	Jablonski diagram (complete).	10
2.2	Fluorescence emission and absorption spectra of TMR	11
2.3	Jablonski diagram of molecular oxygen O ₂	13
2.4	Simplified Jablonski diagram for a dye with three states.	16
2.5	Evolution of the electronic state populations upon modulated excitation.	18
2.6	Evolution of the electronic state populations upon modulated excitation with different pulse widths.	19
2.7	Fluorescence emission for different pulse widths.	20
2.8	Variation of excitation power - effect on P_T^{eq} and the triplet imaging contrast . . .	21
3.1	Triplet lifetime imaging setup	27
3.2	Switching speed limitations imposed by the AOM	29
3.3	Phase contrast principle	30
3.4	Phase contrast image vs fluorescence intensity image	31
3.5	Triplet contrast when varying the pulse period T_p	33
3.6	Modified 4-states jablonski diagram	34
3.7	Image processing in triplet lifetime imaging	35
3.8	Excitation profile estimation in triplet lifetime imaging	36
3.9	Displaying triplet lifetime imaging: three channels of information	37
3.10	Typical triplet imaging result: TMR fixed on coverslide	38
4.1	Dissolved O ₂ vs triplet lifetime	41
4.2	Smooth muscle cell from rat thoracic aorta (A7r5) - Phase contrast image	42
4.3	Principle of the SNAP-tag labeling technique	43
4.4	Induced contraction: Images of oxygen consumption for two experiments	45
4.5	Induced contraction: Evolution of oxygen consumption for five experiments . . .	46
4.6	Triplet lifetime image of A7r5 with varying cellular organelle density	47
4.7	Triplet lifetime image of A7r5 with a NLS marker (nucleus)	48
4.8	Triplet lifetime unmixing	51
4.9	Triplet lifetime images of transferrin recycling	52
4.10	Graph of transferrin recycling	53
4.11	TMR-DNA interaction measured by the triplet lifetime imaging setup	55

List of Figures

5.1	Triplet SOFI: Schematic drawing of the idea	58
6.1	Non-linear $E \rightarrow P$ relation	66
6.2	Gaussian beams. Fundamental vs q th harmonic	67
6.3	Gaussian Volumes: comparison of fundamental, SHG, THG profiles	68
6.4	Gaussian Volumes: profile comparison of fundamental, SHG, THG profiles	69
6.5	Higher harmonic generation from a single particle	70
6.6	Optical interaction with a small sphere with a different refractive index	71
6.7	Size dependant higher harmonic generation from small particles (spheres)	73
6.8	NLCS model - plot of $1/G_0$ vs N	76
6.9	NLCS model - plot of the respective G-terms	77
6.10	NLCS model with flow components	78
6.11	NLCS model with radiation pressure induced flow	79
7.1	Spectrum of the Cr:F laser output in mode-locked mode	81
7.2	Cr:F laser cavity used for higher harmonic generation	82
7.3	Interferometric autocorrelation of the Cr:F laser pulse	83
7.4	Interferometric autocorrelator for pulse length characterizations	84
7.5	Nonlinear correlation spectroscopy setup	85
7.6	Flow-cell setup with aspheric lenses with Zemax PSF	86
7.7	NLCS measurement artifact removal	88
7.8	NLCS: Power dependancy of PS diffusion	89
7.9	Power dependency of the THG intensity and N	90
7.10	NLCS measurements of PS spheres with different sizes	91
7.11	NLCS of KNbO_3 -particle diffusion in SHG and THG	92
A.1	Model for the evolution of the electronic state populations upon modulated excitation.	105
C.1	Colormap: iso-luminescence	122
C.2	Colormap: rainbow	122
C.3	Colormap: jet	123
C.4	Colormap: fire (print optimized)	123

List of Tables

2.1	Typical electronic transition times	10
2.2	Oxygen diffusion constants in various media at a temperature of 25°C	14
2.3	Selected fluorophores and fluorescent proteins and their spectroscopic properties	24
2.4	The ideal triplet lifetime imaging fluorophore: a comparison	25
5.1	The ideal triplet SOFI fluorophore: a comparison	61
6.1	Linear phase factor for water and an ideal dispersion-free solution	74
7.1	Cr:F laser components	82
7.2	Cr:F laser characteristics	83

1 Introduction

Microscopy is one of the major inventions in science because it initiated a wide variety of new fields of research and applications that would not have been imaginable without it. As early as in the 17th century, Antoni van Leeuwenhoek founded the field of microbiology with the help of the light microscopes that he invented. He was able to see for the first time cells and bacteria due to the high magnification and resolution capacity of his microscopes [1]. But today, microscopes are not only employed in life science, they are also essential tools for medicine and material science.

In the history of microscopy, Ernst Abbe contributed significantly to the field, by relating the resolution limit of microscopes to the wavelength of light λ . His formulation states a fundamental physical limitation for the resolvable object size due to the diffraction of light [2]

$$d = \frac{1.22\lambda}{2n \sin \alpha} \quad (1.1)$$

Where n is the index of refraction of the imaging medium and α is the half-angle of the cone of detection of the employed objective lens.

In recent years, major efforts have been concentrated to overcome this resolution limit by developing super-resolution microscopy techniques, or *nanoscopy* techniques [3–5]. Among the established methods are stimulated emission depletion (STED) [6–9], stochastic optical reconstruction microscopy (STORM) [10], photoactivation localization microscopy (PALM) [11], super-resolution optical fluctuation imaging (SOFI) [12], 4Pi [13], I⁵M [14] and various techniques based on structured illumination methods proposed by several independent groups [15–20].

The field of microscopy is not limited to resolving small objects. Major advances in the field of life science and medicine have been possible by *functional imaging*, which means in a broad sense observation of the functioning of living organisms and their evolution in time in

contrast to *structural imaging*. The first time-lapse imaging has been introduced by Gastou and Comandon in 1909 [1]. Nowadays the functional aspect includes also monitoring of specific molecules in time (such as calcium [21–23] and oxygen [24, 25]), imaging of blood flow [26–28], molecular motors [29], imaging of the many facets of cellular metabolism [30] and many other applications.

In addition, spectroscopic (non-imaging) techniques allow to assess additional functional and structural aspects. Among these methods are Fluorescence correlation spectroscopy (FCS) [31, 32], coherent anti-Stokes Raman spectroscopy (CARS) [33], dynamic light-scattering (or photon correlation spectroscopy) [34, 35] and Raman correlation spectroscopy (RLS) [36] to name just a few.

This thesis aims to develop and apply a novel concept for functional high resolution microscopy, named *triplet lifetime imaging*. In a second part of the thesis a novel concept for spectroscopy has been developed based on the non-linear optical interaction of a femto-second laser pulse with nanoparticles. This techniques has been termed *non-linear correlation spectroscopy (NLCS)*.

1.1 Triplet Lifetime Imaging

Oxygen is a key molecule involved in almost every energy cycle within a cell [37] and is responsible for regulating signalling pathways. Measurement techniques addressing partial oxygen pressure pO_2 or even directly the concentration of oxygen $[O_2]$ in vivo are of great interest because they provide us with information for deeper and more complete understanding of cell metabolism [38].

Many methods exist for local oxygen sensing at the cell level. In 1972 Knopp and co-workers attempted to demonstrate intracellular oxygen levels using fluorescence intensity quenching. However, it was only 15 years later, that a technique emerged to overcome the previous limitations and lead to more reliable measurements by using lifetime quenching of various phosphorescence emitting probes [24, 39]. Meanwhile, many probes based on luminescence and phosphorescence quenching have been proposed [40–44]. A more recent approach towards highly localized sensing has been proposed by Finikova in 2008 by using two-photon excited phosphorescence probes [45, 46]. Alternatively Koo et al. [47] proposed insertion of specifically engineered PEBBLE (probes encapsulated by biologically localized embedding) with a diameter of 120nm into the cells resulting in highly sensitive and specific nanosensors for dissolved oxygen based on phosphorescence quenching. Alternative probes for dissolved oxygen measurements include colorimetric probes [48], methods based on fluorescence lifetime measurements of the very long-living fluorophore RTDP [49, 50] and endogenous protoporphyrin IX probes that emit a characteristic delayed fluorescence signal [51, 52]. The

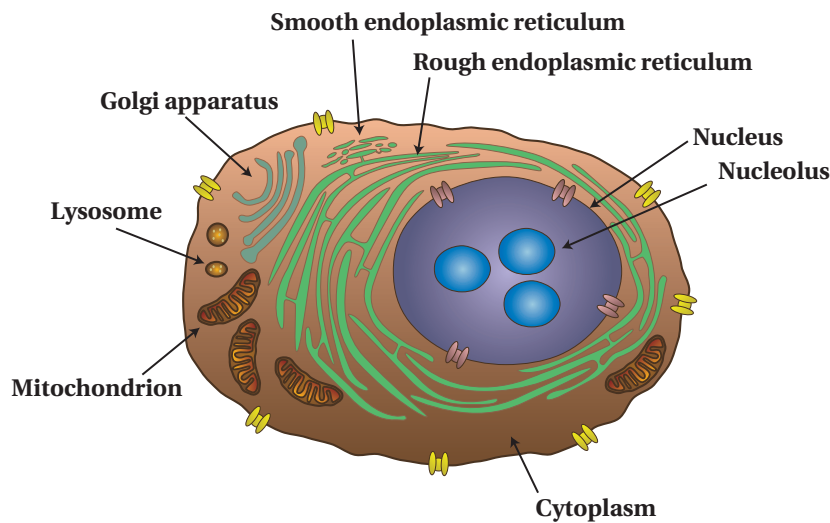


Figure 1.1: Schematic drawing of an eukaryotic animal cell with some organelles (Adapted from [56])

latter has been employed recently *in vivo* to measure the mitochondrial oxygen tension of the heart bringing this non-invasive technique closer to clinical application [53].

However, most of these techniques are based on low-intensity signals which make it difficult to simultaneously achieve high spatial resolution at the cellular level and high-speed to monitor oxygen kinetics. They either allow non-localized ensemble measurements or spatially resolved time-averaged signals. We present a spatio-temporally resolved oxygen measurement at the single cell level based on a fluorescence signal. The method is compatible with almost any fluorophore having a (non-radiative) triplet state that is quenched by diffusing oxygen. The method can be used with many of the different labeling protocols available.

Our experimental concept is described in detail in chapter 3. It is based on a modulated excitation leading to a variation of their triplet state population. The method has been initially validated and published as a spectroscopic method by T. Sandén et al. [54]. Recently, the same team showed the first images based on triplet lifetimes taken with a laser scanning microscope [55]. Although this approach is easy to implement, the method is still limited due to long acquisition times; i.e., approximately 3 min are required to make a single image recording. Here we present a wide-field approach that allows triplet lifetime acquisition within 2 seconds, which is well suited for monitoring oxygen metabolism cycles in living cells which typically span some seconds.

As described in chapter 4, the technique has been applied to measure the oxygen consumption of a single smooth muscle cell upon induced contraction. In contrast to earlier work on oxygen kinetics employing extra-cellular phosphorescence lifetime measurements in a sealed

chamber [57], our method provides spatio-temporal resolution at the intra-cellular and sub-cellular level.

Further on we have successfully applied the technique to detect the presence of DNA, leading to a strong signal that has the potential to be exploitable for imaging purposes as well. In a last experiment we have also shown that the cellular uptake pathway can be assessed by triplet lifetime imaging to reveal further details of the underlying processes.

1.2 Non-linear correlation spectroscopy (NLCS)

Many important questions in life science and medicine request a sensitivity at the single molecule level. This can be readily offered by fluorescence correlation spectroscopy. FCS is a very popular and versatile tool that can be used to study a multitude of problems such as kinetics of enzymes [58], RNA hybridization [59], conformational changes of DNA [60, 61], chemical reaction kinetics [62], studies of phases and other membrane properties (in cellular and model membranes) [63–66], diffusion regimes in microchannels [67], photophysics of fluorophores [68] and many more [62].

However in confined volumes, where there is no renewal of fluorophores, FCS has the fundamental limitation of being sensitive to photobleaching of the fluorescent dye under observation. This makes long-time observations difficult in confined spaces such as cells. To overcome this limitation, techniques such as Raman correlation spectroscopy (RLS) [36] and coherent anti-stokes Raman scattering correlation spectroscopy (CARS-CS) [69, 70] have been developed. In a second part of this thesis, a novel technique named *non-linear correlation spectroscopy (NLS)* is presented that is also free from photobleaching and has the potential to become a very valuable tool for spectroscopy measurements.

In bulk material, the third harmonic contribution vanishes due to the destructive interference of the third harmonic generation in front of and behind of the focal field (Gouy phase shift). On the other hand, nanoparticles with dimensions comparable or smaller than the focal volume can generate strong higher harmonic signals. NLCS relies on these non-linear effects. Our approach is based on a Cr:forsterite laser, which emits fs-pulsed light at a wavelength of $\lambda_0 = 1250$ nm. As a result both the second- as well as third-harmonic generation light is at wavelengths that can be easily assessed with standard optics (625 nm and 417 nm, respectively). This is in contrast to experimental setups based on Ti:Sapphire lasers, where the resulting third-harmonics is in the deep-ultraviolet (DUV) at ≈ 260 nm which is absorbed by most of the standard glasses employed in microscope objectives.

We have studied different types of nanoparticles. Particles based on non-centrosymmetric non-linear materials such as KNbO_3 have been found to show a strong second as well as third harmonic signal.

Chapter 6 gives an overview of the theory of the method and the higher harmonic generation principle and in chapter 7 the setup and some first results on polystyrene spheres (PS) and KNbO_3 are presented.

These spectroscopic results open the door for future extension into imaging concepts.

Triplet Lifetime Imaging **Part I**

2 Molecular fluorescence under modulated excitation

Light microscopy as it is employed today relies heavily on exploiting the high sensitivity and specificity offered by labeling the structures of interest with fluorescent molecules (fluorophores). This basic principle of tagging a macromolecule with a molecule that emits light when being excited by light at a shorter wavelength allows to specifically study localizations, interactions as well as trafficking of the macromolecule of interest. Further on, besides allowing for a readout of the position of the label, a multitude of fluorophores allows further on to report in a quantitative measure environment specific parameters such as ion concentrations (i.e. Ca^{2+}), membrane potentials, pH and many more.

In this thesis we have exploited a concept based on a modulated excitation that allows to "play" with the photophysics of fluorescent molecules. In order to develop the formalism required for the analytical analysis of the resulting measurements, let us review quickly the basic principles of photochemistry. However for a more complete introduction to photochemistry, the interested reader is referred to any textbook on the subject such as books from B. Valeur [71] or N. Turro et al. [72].

2.1 Photochemistry of fluorescent molecules

The wide usability of fluorescence based techniques relies on the Stokes-shift, the physical effect that the light emitted by a fluorophore is of longer wavelength than the absorbed light used to excite the molecule [73]. This allows a spectral separation of excitation and fluorescence light resulting in a high sensitivity; a requirement when looking at single molecules.

An important contribution on the understanding of the various molecular electronic configurations and the transitions between the respective energy levels leading to fluorescence emission under certain conditions, has been done by A. Jablonski [74]. Figure 2.1 shows the Jablonski diagram including the involved electronic states as well as the possible transitions

between them. S_0 , S_1 and S_2 denote singlet states of increasing energy and T_1 and T_2 denote triplet states. Table 2.1 gives an overview of the transition times.

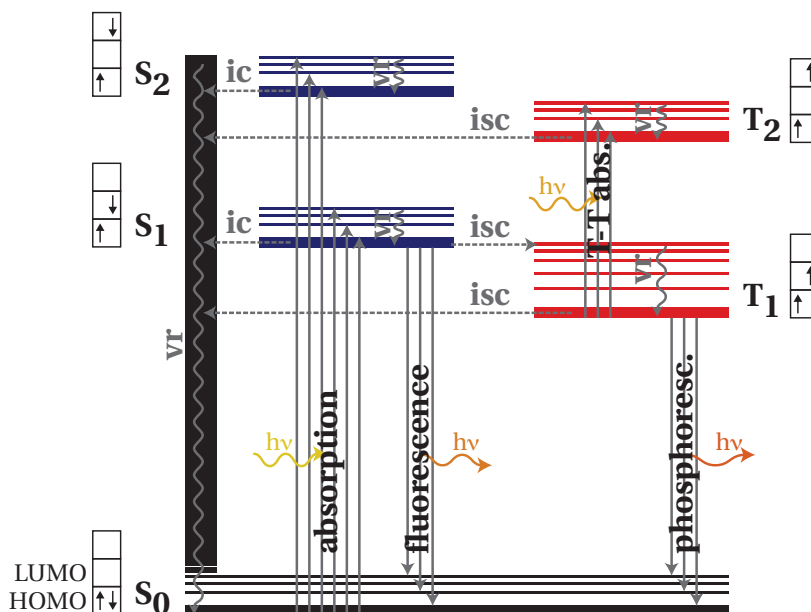


Figure 2.1: Jablonski diagram visualizing the different electronic states and their related vibrational levels as well as all the possible transitions between them: Absorption, fluorescence, phosphorescence, internal conversion (ic), intersystem crossing (isc) and vibrational relaxation (vr). The arrows in the boxes indicate the spin directions: a simplified visualization of the quantum mechanical principle that singlet states correspond to a case where there is no net spin (because of the opposing spins) and while for triplet states there is a net spin (due to parallel spins). This model does not include anionic radical states: see the discussion in chapter 3.1.4 and Fig. 3.6 for further details on this.

The fluorophore can be excited by a photon. During this process an electron of the highest occupied molecular orbital (HOMO), eg the ground state, is excited to a higher state, for example to the lowest unoccupied molecular orbital (LUMO). The excitation usually starts from the lowest vibrational level of the ground state S_0 , because at room temperature the majority of the molecules reside in this state. This brings the molecule to any of the vibrational

Table 2.1: Electronic transitions: Characteristic times [71, 75]

Absorption	10^{-16} s	
Vibrational relaxation (vr)	$10^{-12} - 10^{-10}$ s	non-radiative
Internal conversion (ic)	$10^{-11} - 10^{-9}$ s	non-radiative
Fluorescence	$10^{-10} - 10^{-7}$ s	radiative
Intersystem crossing (isc)	$10^{-10} - 10^{-6}$ s	non-radiative
Phosphorescence	$10^{-4} - 10^2$ s	radiative

levels of the higher energetic singlet states S_1 and S_2 depending on the energy of the exciting photon. Fast vibrational relaxation quickly leads them down to the lowest vibrational level of the respective state. From there, the molecule can also undergo an internal conversion (ic) to higher vibrational levels of the states below it. However the process of interest, is the fluorescence emission, where the molecule undergoes a transition accompanied by the emission of a photon from the lowest vibrational level of S_1 to any of the vibrational levels of the ground state. As visible by comparing the "length" of the arrows of the absorption to them of the fluorescence emission: the radiative transitions from S_1 to S_0 are of lower energy than the absorption: this is called the Stokes-shift. It can also be seen clearly on the absorption and emission spectrum of the fluorophore of interest. Figure 2.2 shows the absorption and fluorescence emission spectra of tetramethylrhodamine (TMR), the fluorophore that has been most widely used in this thesis.

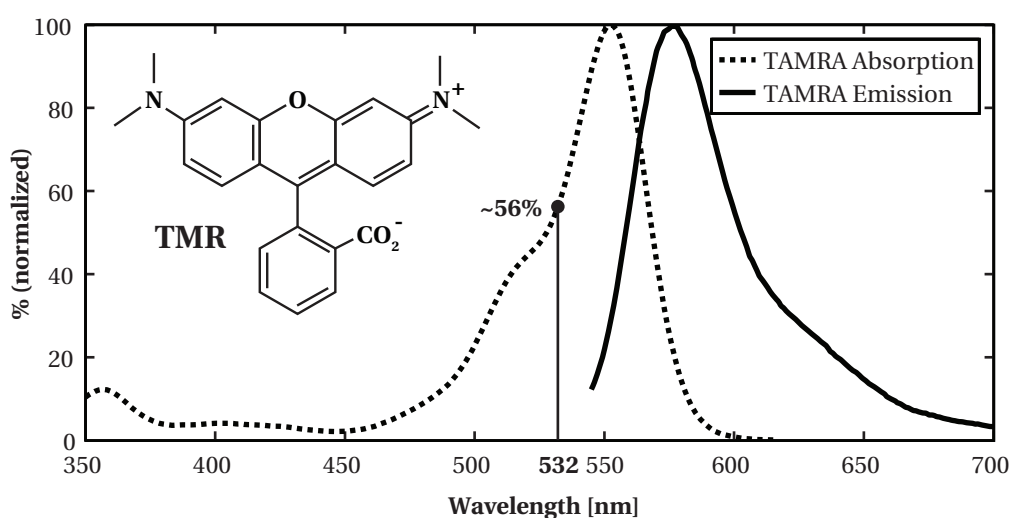


Figure 2.2: Normalized absorption and fluorescence emission spectra of Invitrogen's carboxytetramethylrhodamine (TAMRA) which is the protonated form of tetramethylrhodamine (TMR) in pH 7.0 buffer. The inset shows the chemical structure of TMR.

2.1.1 Triplet state vs Singlet state

The molecular quantum mechanical wave function Ψ is a combination of the electron configuration (eg orbitals), the nuclear configuration as well as the spin configuration. Although there is no classic equivalent to the quantum mechanical spin, for the sake of simplicity, the spin can be understood as the angular momentum of a rotating negatively charged sphere (eg an electron) around an axis. Unless in classical angular momentums, in the quantum mechanical description of the molecule, the electron spin s can have only discrete values of either $s = +1/2$ or $s = -1/2$. The Pauli exclusion principle states that no more than two electrons may occupy the same electronic orbital and only if their spins are in opposite directions. As a result, if two electrons occupy the same orbital, they have a total spin of $S = \sum_i s_i = +1/2 - 1/2 = 0$ and hence

the number of possible orientations of the spin angular momentum corresponding to a given S value, is $M = 2S + 1 = 1$ for singlet states. On the other hand, triplet states correspond to excited states, where the excited electron has the same spin as the electron of the correspondingly lower orbital. As a result, triplet states have a total spin of $S = \sum_i s_i = +1/2 + 1/2 = 1$ and correspondingly a spin multiplicity of $M = 2S + 1 = 3$. This means that for a triplet state there are three (*triplet*) possible spin states denoted $M_S = 0$, $M_S = +1$ and $M_S = -1$, while for the singlet state case there is only one possible spin state $M_S = 0$ (*singlet*) [72].

The probability of transitions between different configurations can be described with the help of the transition dipole moment that takes into account the differences of the respective quantum mechanical wave functions of the initial and final state. From this, the so-called selection rules can be derived that state certain conditions that have to be maintained when passing from one state to another. Among those selection rules, transitions that include a spin-flip are considered "forbidden", in other words the magnetic momentum has to be conserved during a transition. This means transitions between the same spin configurations such as $S_0 \rightarrow S_1$, $S_1 \rightarrow S_2$ as well as $T_1 \rightarrow T_2$ are *allowed*, while transitions where the electron needs to flip its spin such as $S_1 \rightarrow T_1$ and $T_1 \rightarrow S_0$ are *forbidden*.

However the movement of electrons on large orbitals can lead to a spin-orbit coupling which relaxes the selection rules and makes spin-flip related transitions *possible*. In comparison, the probability for such spin-forbidden transitions is still much lower than for spin-allowed transitions. This can also be observed directly when looking at their typical transition times (See table 2.1) [71, 72, 75].

2.1.2 Interaction with molecular oxygen

Molecular oxygen O_2 is a very special molecule in terms of photochemistry: its a very prominent participant in photochemical interactions and reactions as well as an exception to many of the established principles that are valid for other organic molecules [72]. The O_2 ground state is a triplet state (usually symbolized with $^3\Sigma$) and the lowest available excited energetic state is a singlet state ($^1\Delta$), which is the opposite of the vast majority of organic molecules, where the ground state is a singlet configuration and the lowest excited level is a triplet configuration [72]. Figure 2.3 shows the three lowest energy levels of molecular oxygen and the corresponding energies required for transitions between them. The energy gap between the ground state and the first excited state is rather small (corresponding to the energy of a photon with $\lambda = 1270\text{nm}$). Besides the spin-flip requirement, the transition is hence readily available for energy transfers from the excited states of almost all fluorophores in the visible and near-infrared.

The first excited state S_1 of molecular oxygen ($^1\Delta$) is also called *singlet oxygen*, a highly reactive compound known for many years to be involved in oxidation [76]. There are also many

chemical synthesis based reactions with singlet oxygen [75–78], requiring so called photosensitizer for singlet oxygen (usually fluorophores with high triplet yields such as eosine or rose bengal) [77]. A particular field of application for singlet oxygen is photodynamic therapy: controlled production of singlet oxygen leads to oxidative stress and tissue damage [79].

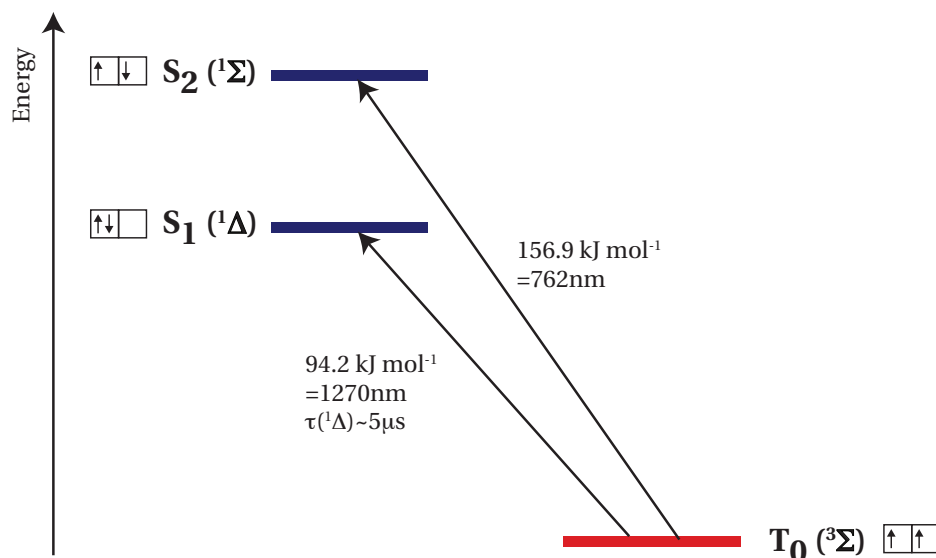


Figure 2.3: Jablonski diagram of molecular oxygen O_2 showing the ground state (a triplet configuration) as well as the two lowest excited energy levels (singlet states) with the corresponding transition energies. In water, the first excited state has a typical lifetime of $5\mu\text{s}$ [72, 75].

In water at standard conditions (temperature of 25°C and pressure of 1 atm) the concentration of molecular oxygen is roughly $[O_2] \approx 8.3\text{mg/l} \approx 0.3\text{mM}$. Further on, molecular oxygen has a diffusion constant at standard conditions of $D = 19.6 \times 10^{-6} \text{ cm}^2\text{s}^{-1}$ [80] which is about 5 times faster than typical diffusion constants of standard fluorophores, such as Rhodamine 6G with $D = 4.0 \times 10^{-6} \text{ cm}^2\text{s}^{-1}$ [81]. Additionally in tissue and membranes the diffusion coefficient of oxygen remains rather fast, indicating that none of these materials provide a diffusion-barrier to oxygen. Table 2.2 gives an overview of oxygen diffusion values in different media.

All of the above features of molecular oxygen – the low energy gap between the ground state and the first excited state, the rather high concentration at normal condition as well as the rather fast diffusion constant – are reasons why oxygen plays an important role for fluorescence in the context of microscopy, where in general the employed concentrations and amounts of fluorescent molecules can be considered lower compared to the amount of oxygen present in the same solution.

Oxygen plays two important roles in the interaction with fluorescent molecules: as a quencher as well as a reaction partner leading to photobleaching of the fluorophore via oxidation. The main quenching potential is related to the triplet state of the fluorophore: molecular oxygen

Chapter 2. Molecular fluorescence under modulated excitation

Table 2.2: Oxygen diffusion constants in various media at a temperature of 25°C. The values can be compared to the diffusion constant of Rhodamine 6G in water where $D = 4.0 \times 10^{-6} \text{ cm}^2\text{s}^{-1}$

Material	D [$10^{-6} \text{ cm}^2\text{s}^{-1}$]	References
Water	19.6	[80]
Saline water	20.7	[82]
Gas phase	336.0	[82]
Skeletal muscle	13.0	[82]
Erythrocyte plasma membrane	22.0	[82]
"Apparent" diffusion in a cell	2.0-4.0	[78]
Dimyristoyl lecithin	4.7	[82]
PDMS	9.75	[83]
Silicone	0.67	[84]
Fluran	<0.002	

(in its ground state) can accept an energy transfer from this state. For fluorescein it was possible to demonstrate that in a carefully deoxygenated solution, the triplet state lifetime can be as long as 20ms, while at standard conditions, the presence of oxygen shortens it to some 0.1 to 1 μs [85, 86]. In this thesis, the deoxygenation was investigated using TMR, which allowed to demonstrate that the triplet lifetime can be prolonged at least by a factor of 2 to 3, when removing the dissolved oxygen with the help of an oxidation assay. However experimental limitations did not lead to similarly deoxygenated conditions as in the above study with fluorescein. We would hence expect that the triplet lifetime for TMR in the absence of oxygen would be much higher as well. Both of these experiments demonstrate hence the importance of oxygen as a triplet state quencher. However not only the excited triplet state can be quenched by oxygen, also the intersystem crossing is influenced directly by oxygen, acting hence as a quencher for the excited singlet state as well. For Rhodamine 6G, Gregor et al. showed a linear relation between the quencher concentration (oxygen) and the triplet relaxation rate (τ_T^{-1}) as well as the intersystem crossing rate (τ_{isc}^{-1}) according to the Stern-Volmer prediction for quenching assays [87].

Similarly oxygen plays a role in the photo-bleaching of the fluorescent compounds leading to the undesired irreversible loss of the fluorescent emission. In a study on fluorescein, Song et al. demonstrated that the removal of oxygen using argon flushing will reduce the photobleaching by more than a factor of 2 [88]. However they also noticed that, since no singlet oxygen scavenger had considerable effects on the photobleaching rates, "it may not be the major cause of photobleaching of fluorescein" [88]. In more recent work, Renn et al. looked the photostability at the single molecule level where they made even more striking conclusions: "Surprisingly, we find an improvement of photostability in the presence of oxygen for ionic dyes (DiI, TMR, Rh6G, Alexa 546), suggesting that oxygen quenches the photoactive triplet state, but it only indirectly contributes to photochemistry" [89]. However in their study, they embed the fluorescent molecules in a rigid PMMA matrix in order to be able to study stationary

single molecules. Whether the conclusions that can be drawn from this rigid matrix can be applied directly to the case of fluorphores in water (where they are free to rotate and move) needs further investigation.

2.2 Simplified three state model

The complete Jablonski diagram in figure 2.1 is very helpful for the understanding of all the involved processes. However it is too complex to provide a basis for an analytical model. A simplification is required in order to be able to predict for an ensemble of fluorescent molecules the mean number on each of the electronic states. The following simplifications and approximations are made:

1. Vibrational transitions are very fast: the vibrational bands of each state can hence be simplified to a single level.
2. The sample is illuminated by a well defined laser wavelength: we neglect absorptions onto higher singlet states.
3. The lifetime of the triplet state T_1 is much longer than a cycle through the higher triplet state T_2 by triplet-triplet absorption and relaxation since they are quantum mechanically allowed. The Triplet states can hence be simplified to a single level.
4. Internal conversion to vibrational levels of the lower energetic states combined with vibrational relaxation can be simplified by an additional non-radiative pathway with a typical rate of $k_{non-rad.}$.
5. The lifetime of the excited singlet state S_1 is a combination of all relaxation pathways that depopulate it: non-radiative transition ($k_{non-rad.}$), fluorescence emission ($k_{rad.}$) as well as intersystem crossing ($k_{isc.}$). Since the latter term is small compared to the other two terms, the lifetime of the state can be expressed as $\tau_S = (k_{non-rad.} + k_{rad.})^{-1}$
6. The absorption, eg the time it takes the molecule to reach the excited state such as depicted in figure 2.1, is very fast. The effective excitation rate τ_{ex} is hence only limited by the illumination intensity and the absorption cross-section of the molecule.

As a consequence of these approximations, we continue the development with a simplified three state model for the fluorophore as shown in figure 2.4.

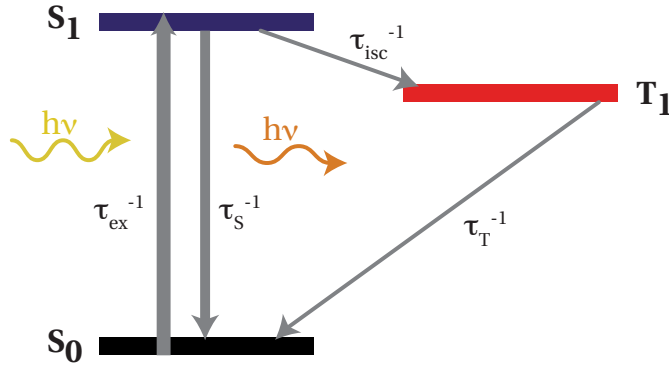


Figure 2.4: Simplified Jablonski diagram for a fluorescent dye molecule with three states.

2.2.1 Derivation of an analytical model

This simplified model can now be used as a basis to derive an analytical model starting from the rate equations

$$\frac{d}{dt} \begin{bmatrix} P_0 \\ P_I \\ P_T \end{bmatrix} = \begin{bmatrix} \frac{P_I}{\tau_S} + \frac{P_T}{\tau_T} - \frac{P_0}{\tau_{ex}} \\ -\frac{P_I}{\tau_S} - \frac{P_I}{\tau_{isc}} + \frac{P_0}{\tau_{ex}} \\ \frac{P_I}{\tau_{isc}} - \frac{P_T}{\tau_T} \end{bmatrix} \quad (2.1)$$

where P_0 , P_I and P_T are the respective populations of the singlet states and the triplet state, τ_S is the lifetime for the singlet state relaxation, τ_{isc} is the intersystem crossing lifetime from the excited singlet state to the triplet state, τ_T is the triplet state lifetime and τ_{ex} is the excitation lifetime, which is a measure for the incoming intensity taking into account the absorption cross section of the molecule (τ_{ex} is often also denoted as α^{-1} where α is the excitation rate).

The fluorescence quantum yield is generally defined as the ratio of the emission rate (fluorescence) over the total relaxation rate. Hence we write

$$\Phi_F = \frac{k_{rad.}}{k_{rad.} + k_{non-rad.} + k_{isc}} \approx \frac{k_{rad.}}{\tau_S^{-1}}. \quad (2.2)$$

In a similar way we can define a triplet quantum yield, which is a measure for the efficiency of passing onto the triplet state, by

$$\Phi_T = \frac{k_{isc}}{k_{rad.} + k_{non-rad.} + k_{isc}} \approx \frac{\tau_S}{\tau_{isc}}. \quad (2.3)$$

Including a constant total population

$$P_0 + P_I + P_T = 1$$

and employing again that $\tau_S^{-1} + \tau_{isc}^{-1} \approx \tau_S^{-1}$, we can rewrite the rate equation 2.1 in a second order differential equation in P_T

$$\tau_S \tau_T \frac{d^2 P_T}{dt^2} + \left(\tau_S + \tau_T + \frac{\tau_S \tau_T}{\tau_{ex}} \right) \frac{dP_T}{dt} + \left(1 + \frac{\tau_S}{\tau_{ex}} + \frac{\Phi_T \tau_T}{\tau_{ex}} \right) P_T = \Phi_T \tau_T \frac{1}{\tau_{ex}} \quad (2.4)$$

In order to solve this equation for the case of a modulated excitation, we separate two different excitation cases, an *on* and an *off* case. We start from an Ansatz of the form

$$P_T = a \exp(kt) + b \quad (2.5)$$

By identification of constant coefficients in equation 2.4 we can identify b to be

$$b = \frac{\Phi_T \tau_T}{\tau_{ex} + \tau_S + \Phi_T \tau_T} = P_T^{\text{eq}} \quad (2.6)$$

This is the relative triplet population for a constant excitation at equilibrium (for $t \rightarrow \infty$).

With the help of this Ansatz, we can now derive an expression for the average fluorescence intensity for an iso-dosis of light exposure. The full derivation is given in appendix A on page 105. This leads to the following equation:

$$\overline{I_F(\vec{r})} = \gamma(\vec{r}) \left(1 - \frac{\tau_T P_T^{\text{eq}} \left(1 - \exp\left(-\frac{(T_p - t_p)}{\tau_T}\right) \right)}{1 - \exp\left(-\frac{(T_p - t_p)}{\tau_T}\right) + k_2 t_p} \times \frac{(\exp(k_2 t_p) - 1)}{t_p} \right) \quad (2.7)$$

where k_2 describes the population rate of the triplet state after onset of excitation and $\gamma(\vec{r})$ is a scaling factor depending on the concentration of fluorophores and the detection efficiency; they are given as:

$$k_2 = - \left(\frac{\tau_{ex} + \tau_S + \Phi_T \tau_T}{\tau_T (\tau_{ex} + \tau_S)} \right) = - \left(\tau_T (1 - P_T^{\text{eq}}) \right)^{-1} \quad (2.8)$$

$$\gamma(\vec{r}) = \eta \Gamma(\vec{r}) \frac{\Phi_F}{\tau_{ex} + \tau_S + \Phi_T \tau_T}$$

where t_p denotes the pulse width, T_p the repetition rate and τ_S , τ_T and τ_{ex} express the respective lifetimes as used in equation (2.1); further, $\Gamma(\vec{r})$ is the local concentration of fluorophores, η is a conversion factor between the emitted intensity and the digital readout of the camera. The rate equations above can be used to simulate the response to a modulated excitation (see Fig. 2.5) using typical rate constants of a given fluorophore (TMR). In the figure, the entities from the above equations 2.6 and 2.8 are also indicated graphically for better understanding.

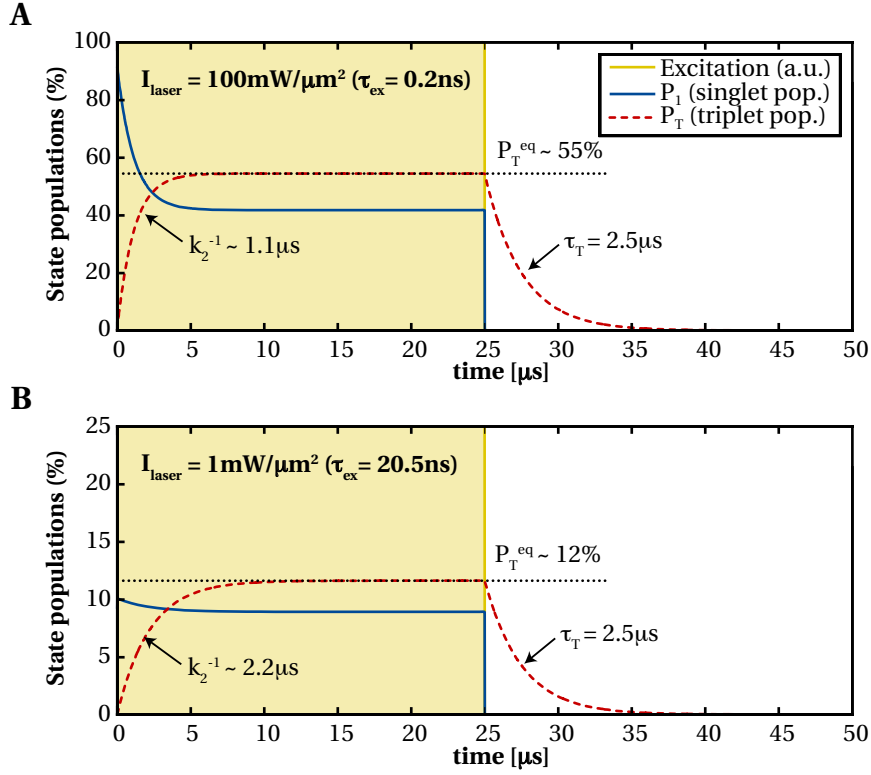


Figure 2.5: Evolution of the electronic state populations upon modulated excitation with typical relaxation and buildup times for tetramethylrhodamine for two different laser intensities. Typical values for TMR (excited at 532nm) were used: $\tau_s = 2.3 \text{ ns}$, $\tau_T = 2.5 \mu\text{s}$, $\Phi_T = \tau_s / \tau_{\text{isc}} = 0.12\%$ and $\sigma(\lambda = 532 \text{ nm}) = 1.82 \times 10^{-16} \text{ cm}^2$ resulting in $\tau_{\text{ex}} = 20.5 \text{ ns}$ (for the illumination intensity of $1 \text{ mW}/\mu\text{m}^2$).

2.3 Fluorescence emission under modulated excitation

Using the rate equations for our simplified three-level system, we can now simulate the behavior of the emission for different pulse widths (see Fig. 2.6). The result of the simulation shows an increase of the triplet state population for longer pulse widths, which decreases the number of molecules available for the singlet states. Since the fluorescence intensity is proportional to the excited singlet state population, we expect a correspondingly lower signal for longer pulse widths – besides the linear increase due to the increased pulse width. The contrast for this effect is greatly improved when using an iso-dosis of light exposure. Additionally in practice this allows for better signal quality without the need for a very high dynamic range of the camera. The result for the simulation for the two illumination types can be seen in Fig. 2.7.

It is worth mentioning that although we are using this effect to add an environment sensitivity to fluorescence microscopy, it is also beneficial for standard microscopy: since the signal is correspondingly higher for short pulses, it seems obvious that we should get higher signal

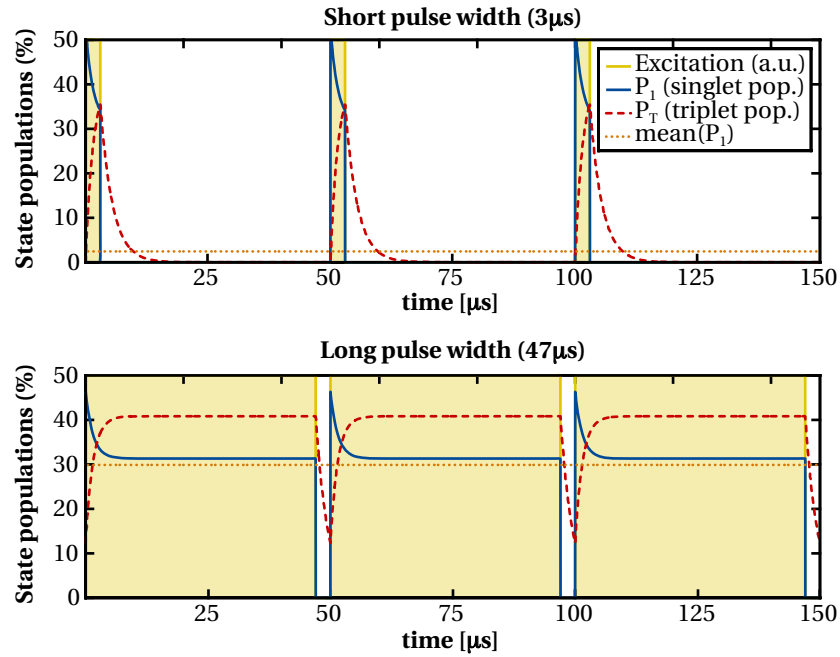


Figure 2.6: Evolution of the electronic state populations upon modulated excitation for two different rectangular pulses of $3\mu\text{s}$ and $47\mu\text{s}$ respectively and $50\mu\text{s}$ period. Typical values for TMR (excited at 532nm) were used: $\tau_s = 2.3\text{ ns}$, $\tau_T = 2.5\mu\text{s}$, $\Phi_T = \tau_s/\tau_{isc} = 0.12\%$ and $\tau_{ex} = 2.1\text{ ns}$ (corresponding to an illumination intensity of $10\text{mW}/\mu\text{m}^2$).

intensities when using a pulsed excitation that leaves time for a triplet state population relaxation compared to a continuous excitation. This idea has been published under the name of "T-rex" (triplet relaxation modality) by Donnert et al. [90, 91].

2.4 The ideal fluorophore

Table 2.3 on page 24 gives an overview of parameters for many fluorophores. In order to find the optimal fluorophore for triplet lifetime imaging, we first want to define what we mean by *ideal*:

- The goal of triplet imaging is to be sensitive to the environment. The sensitivity is increased if the probability to interact with the environment is increased. This translates in two things: the triplet lifetime should be long and the fluorophore should be physically accessible to the environment we want to sense (no shielding).
- The whole technique builds on fluorescence intensity differences arising from different populations of the electronic states for varying pulse widths. This contrast can be defined as the difference between the relative triplet population for a short pulse and the maximum triplet population.

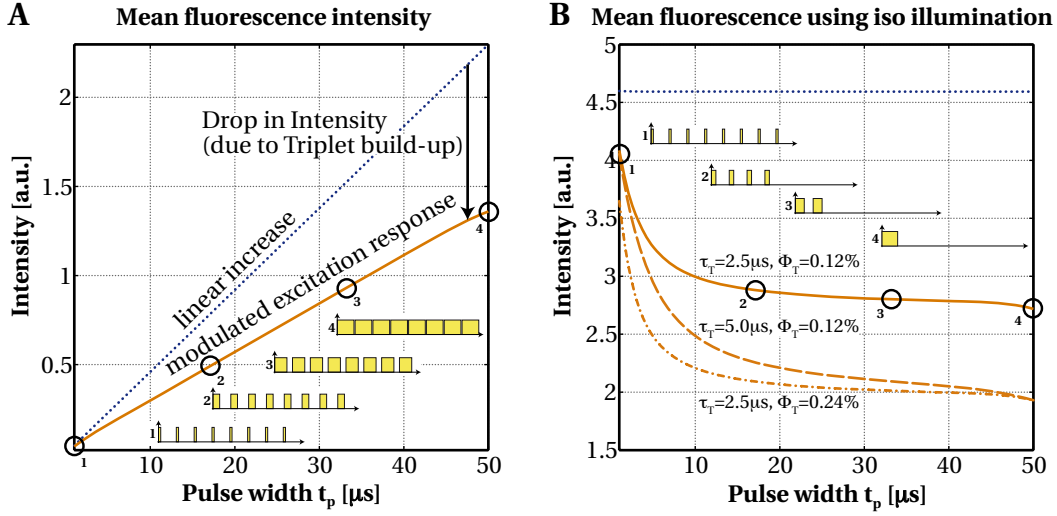


Figure 2.7: (A) Fluorescence emission for different pulse widths. (B) Fluorescence emission when using an iso-dosis of light illumination removing the linear increase. Three different cases of τ_T and Φ_T are shown. For all curves $\tau_s = 2.3 \text{ ns}$, and $\tau_{ex} = 2.1 \text{ ns}$ (corresponding to an illumination intensity of $10 \text{ mW}/\mu\text{m}^2$ for TMR).

- We observe the fluorescence intensity, so if there is an important non-radiative component in the relaxation from the singlet state S_1 , the efficiency of the emission is decreased. This translates in the requirement of a high fluorescence quantum yield Φ_F .

Then let us define the following practical limitations

- The fluorophore will have to be excited by a modulated light pulse. Realistically this can only be done in the required switching speeds for sharp laser lines. Let us hence focus the consideration to some of the most common lasers used in light microscopy: an argon laser (488nm and 514nm), a frequency-doubled Nd:YAG (or similar laser types leading to the same wavelength of 532nm) as well as a Helium Neon (633nm)
- In practice there will always be a laser output power limitation. In order to compare the respective fluorophores irrespectively of the laser type used, let us define that every laser has the power to excite the sample with $1 \text{ mW}/\mu\text{m}^2$. Most of the interesting parameters (P_T^{eq} , R^{eq} and C_{max}) scale with the laser intensity in the same way as the % Saturation (as shown in Fig. 2.8). This makes it easy to estimate the upper theoretical limits to investigate if it is worth changing the setup to reach higher illumination intensities.
- The technique is based on differences between the shortest and longest pulse widths. In order to calculate an "available" contrast, let us define the shortest pulse width to be $1 \mu\text{s}$ and the longest to be $50 \mu\text{s}$. This corresponds to what has typically been used as pulse width spreading during this whole thesis. Note that the main limitation here is

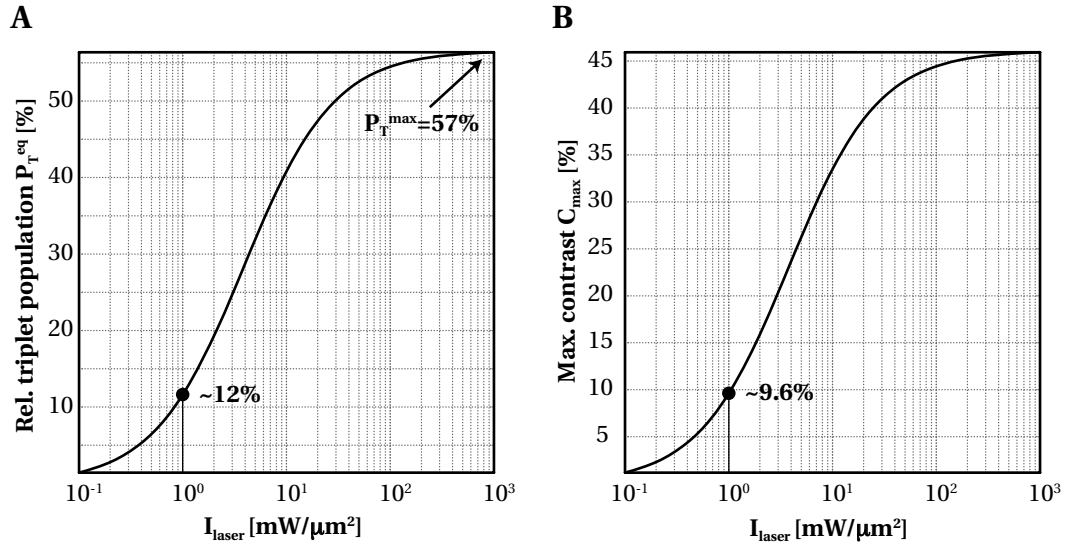


Figure 2.8: Variation of the excitation power and its effect on P_T^{eq} and the triplet imaging contrast C_{max} . The simulation has been done with standard values for TMR excited at 532nm. An indicator shows the $1\text{mW}/\mu\text{m}^2$ case that has been used in table 2.4 to find the ideal fluorophore. The value is also close to what has been used for the imaging setup.

certainly the shortest pulse width and it might be shorter when using different switching mechanisms.

Having defined the boundary of our quest, we can now investigate for each fluorophore where the data is available, the following parameters:

- τ_T The triplet lifetime. The longer the better.
- Φ_F The fluorescence quantum yield. The higher the better.
- P_T^{eq} Relative triplet population at equilibrium according to equation 2.6 for each laser wavelength taking into account the different absorption cross sections for each wavelength.
- P_T^{max} Maximum relative triplet population. This is for the hypothetical case that we would have an "infinitely" strong excitation leading to a case where $\tau_{\text{ex}} = 0$. It gives a measure for the upper limitation of the % of molecules that can be pumped onto the triplet state for this fluorophore.
- % Sat The percentage of saturation we are achieving which gives a quantification on how much better we could get for this fluorophore when using a more confined area of illumination or a higher laser power. It is calculated simply as the ratio between the relative triplet population at equilibrium and the maximum triplet population: % Sat = $P_T^{\text{eq}}/P_T^{\text{max}}$.

Chapter 2. Molecular fluorescence under modulated excitation

R^{eq} The photon emission rate at equilibrium (steady-state case) where the triplet state is populated by P_T^{eq} .

C_{max} The typical intensity contrast we can expect for this fluorophore. According to equation 2.7 for the average fluorescence intensity, we calculate $\overline{I_{F,1}}$ and $\overline{I_{F,50}}$ for pulse widths of respectively $t_p = 1\mu\text{s}$ and $t_p = 50\mu\text{s}$ and define

$$C_{\text{max}} = \frac{\overline{I_{F,1}} - \overline{I_{F,50}}}{\overline{I_{F,1}}}. \quad (2.9)$$

In order to calculate the respective entitites we must calculate the excitation rate τ_{ex} . The molar extinction coefficient ϵ_{max} at the absorption peak λ_{max} in $[\text{L mol}^{-1} \text{ cm}^{-1}]$ and the molecular absorption cross-section σ_{max} in $[\text{cm}^2]$ are related as follows [71]:

$$\sigma_{\text{max}} = \frac{2.303 \times \epsilon_{\text{max}}}{N_A} = 3.825 \times 10^{-21} \times \epsilon_{\text{max}} \quad (2.10)$$

Let us define a *relative* absorption constant

$$A(\lambda) = \begin{cases} 1 & \text{for } \lambda = \lambda_{\text{max}}, \text{ the wavelength of maximum absorption} \\ 0 \dots 1 & \text{according to the relative absorption at the given wavelength.} \end{cases}$$

We can now write the effective cross section for the given wavelength as

$$\sigma(\lambda) = A(\lambda) \times \sigma_{\text{max}} \quad (2.11)$$

We have defined that the laser intensity is $I_{\text{laser}} = 1\text{mW}/\mu\text{m}^2 = 1 \times 10^9 \text{ W/m}^2$ and hence we find as excitation time

$$\tau_{\text{ex}} = \alpha^{-1} = \left(\frac{I_{\text{laser}} \sigma(\lambda)}{\frac{hc}{\lambda}} \right)^{-1} = \frac{hc}{\lambda I_{\text{laser}} \sigma(\lambda)} \quad (2.12)$$

To find the rate of photon emission per molecule, we first must find the amount of molecules on the singlet state. From the rate equations 2.1 we can rewrite the last line for the steady case ($\frac{dP_T}{dt} = 0$), hence

$$P_I^{\text{eq}} = \frac{\tau_{\text{isc}}}{\tau_T} P_T^{\text{eq}} \quad (2.13)$$

The rate of photons emitted per second for each molecule for the steady case can be calculated as

$$R^{\text{eq}} = \frac{\Phi_F P_I^{\text{eq}}}{\tau_S} = \frac{\Phi_F \tau_{\text{isc}} P_T^{\text{eq}}}{\tau_T \tau_S} = \frac{\Phi_F}{\Phi_T} \frac{P_T^{\text{eq}}}{\tau_T} \quad (2.14)$$

Using the fluorophore data from table 2.3, we can now compile a list with the above mentioned values for the different laser lines. The result is given in table 2.4 on page 25.

2.4.1 Discussion

Table 2.3 serves as a guideline. Values for the spectral properties and the extinction coefficient are usually very well defined. Similarly the singlet lifetime and quantum yield can be determined to a good precision for the given solvents. However the triplet lifetime of most fluorophores is mainly determined by the oxygen content of the solvent and its viscosity. In principle the same holds true for the intersystem crossing (or triplet yield). Additionally the data for triplet lifetime and -yield is not independent of the method that has been used to assess it. As an example the triplet lifetime and -yield of Rhodamine 110 has been determined by Menzel et al. using time-resolved laser-scanning-microscopy [97]. They measured values of $\tau_{T, Rh\ 110, Menzel} = 5.0\ \mu s$ and $k_{isc, Rh\ 110, Menzel} = 0.53\ \mu s^{-1}$. The same fluorophore has been measured by Blom et al. using confocal fluorescence correlation spectroscopy (FCS) [94]. They measured values of $\tau_{T, Rh\ 110, Blom} = 2.2\ \mu s$ and $k_{isc, Rh\ 110, Blom} = 1.0\ \mu s^{-1}$. Both values differ by a factor of 2. However it is interesting to notice that the *product* of the two values is nearly identical for the measurements of both groups. In our own findings with triplet lifetime imaging (yet another method), we have found it difficult to determine both the triplet lifetime and -yield (which is $\propto k_{isc}$) completely independently. Figure 4.11 shows an example of the dependancy between the two values. Both values are describing non-radiative relaxation rates and in order for the fluorophore to cycle from the bright to the dark state and back, it needs to pass both pathways and is hence also affected by both relaxation rates. As a result it seems plausible that there could indeed be link between the measurements of the two parameters for methods assessing the parameters with the help of the fluorescence emission. Further investigations should be done to clarify the exact nature of the link between both parameters assessed by various methods.

Nevertheless table 2.3 compiles important photo physical values for many of the most commonly used fluorophores and can be used as a basis to figure out the *ideal* triplet lifetime imaging fluorophore based on the subsequent table 2.4. Although our method can be employed with almost any fluorophore, there are more suitable candidates. For the case of excitation with a laser at 532 nm, the fluorophore that we have employed mostly in this work, Tetramethylrhodamine (TMR), gives an expected contrast of below 10 % with a photon-emission rate of about 11MHz. In future studies, it would be interesting to switch to Rhodamine 6G, since the latter is expected to show a five-fold higher emission rate and a three-fold higher contrast for the same excitation power. Both values have similar triplet lifetimes and -yields, the improvements stem from the higher quantum yield and also from the stronger absorption at 532 nm.

Chapter 2. Molecular fluorescence under modulated excitation

Table 2.3: Selected fluorophores and fluorescent proteins and their spectroscopic properties

	Abs./Em. ^a	Φ_F^b	ϵ^c	τ_S^d	τ_T^e	k_{isc}^f	Φ_T^g	References
Fluorophore								
TMR	554/573	28 ^{C1}	85 ^{C1}	2.3 ^{C1}	2.5 ³	0.54	(0.12) ^{1,3}	MP, [86, 92]
AlexaFluor 488	494/519	92 ^{C1}	65 ^{C1}	4.1 ^{C1}				MP, ISS
AlexaFluor 532	530/555	61 ^{C1}	81 ^{C1}	2.5 ^{C1}				MP, [86]
AlexaFluor 555	555/565	10 ^{C1}	155 ^{C1}	0.3 ^{C1}				MP, [86]
CY3	554/568	14	130	0.3 ^{C1}				ISS, [86]
CY5	652/672	18	200	1.0 ^{C1}	2 ^{C4}	1.1	(0.11) ^{C4}	ISS, [86, 93]
Fluorescein	490/520	71	67	4.16	1.89	11.1	(4.6)	MP, [86, 94, 95]
Rhodamine 6G	530/558	95	116 ^{C1}	3.9	2.56	0.73	(0.28) ¹	OC, [92, 96]
Rhodamine 123	511/534	90	85	4.0	1.89	1.0	(0.4)	[94–96]
Rhodamine 110	505/534	94	81	4.0 ^{C4}	5.0	0.53	(0.21)	MP, ISS, [97]
Rhodamine B	562/583	53	106 ⁵	1.68 ^{C4}	6.0	0.53	(0.09)	ISS, OC, [97, 98]
Texas Red	589/615	51	85	4.2 ^{C4}				ISS, [86]
Atto 488	501/523	80 ^{C4}	90 ^{C4}	4.0 ^{C4}	4.0 ^{C1}	1.5	(0.6) ^{C1}	AT, [94, 95]
Atto 520	516/538	90 ^{C4}	110 ^{C4}	3.8 ^{C4}				AT
Atto 532	532/553	90 ^{C4}	115 ^{C4}	3.8 ^{C4}				AT
Eosine Y	515/540 ^{C4}	22 ^{C4}	11.7	1.55 ^{C4}	0.001 ^{C4}	(0.8M)	80 ^{C4}	[99, 100]
Rose Bengal	556/572	5 ^{C2}	90.4	2.79 ^{C6,4}	0.4 ^{C6}	(143.4)	40 ^{C6}	OC, ISS, [101–103]
Fluorescent proteins								
EGFP	489/508	60	55	2.5				[86, 104, 105]
EYFP	514/527	61	84					[86, 104]
mRFP	584/607	25	44					[106]
DsRed	558/583	68	72.5	2.8 ²				[86, 104, 105]
mCherry	587/610	22	72	1.4				[107]
mOrange	548/562	69	71					[108]

^a Absorption / Emission maxima wavelengths [nm]

^b Fluorescence quantum yield [%]

^c Extinction coefficient ϵ for the wavelength of the absorption maxima [$\times 1000 \text{ L mol}^{-1} \text{ cm}^{-1}$]

^d Lifetime of first excited singlet state S_1 [ns]

^e Lifetime of first excited triplet state T_1 [μs]

^f Intersystem crossing rate ($S_1 \rightarrow T_1$) [μs^{-1}] - Values in brackets are calculated.

^g Triplet quantum yield [%] - Values in brackets are calculated.

¹ The value has been calculated by $\Phi_T = \tau_S / \tau_{isc} = \tau_S \times k_{isc}$

² The value decreased to 1.5ns in aged cell cultures (several days)

³ In our own study we have found slightly different values: $\tau_T = 3.1 \mu\text{s}$ and $\Phi_T = 0.2\%$ [109]

⁴ In another source, for a different measurement condition they found significantly different lifetime of 519ns^{C3}

⁵ There seems to be a reliable source for this measurement. It has been found on the OC webpage.

^{C1} Measurement conditions: pH7, PBS

^{C2} Measurement conditions: EtOH

^{C3} Measurement conditions: MeOH

^{C4} Measurement conditions: Water

^{C5} Measurement conditions: pH8

^{C6} Measurement conditions: air saturated acetonitrile

MP stands for Molecular Probes <http://www.invitrogen.com/>

ISS <http://www.iss.com/>

AT stands for Atto-Tec GmbH <http://www.atto-tec.com/>

OC stands for Oregon Medical Laser Center <http://omlc.ogi.edu/>

2.4 The ideal fluorophore

Table 2.4: The *ideal* triplet lifetime imaging fluorophore: a comparison of relevant parameters when excited by three different lasers: Argon (488nm and 514nm), frequency doubled Nd:YAG (532nm) as well as Helium-Neon laser (633nm) each with a resulting sample illumination intensity of 1mW/ μm^2 .

	$A(\lambda)$ [%]	τ_T [μs]	Φ_F [%]	P_T^{eq} [%]	P_T^{max} [%]	% Sat.	R^{eq} [MHz]	C_{max} [%]
488nm								
TMR	12	2.5	28	2.8	56.6	5	2.6	2.3
Fluorescein	77	1.89	71	77.9	95.4	81.6	6.4	57.3
Rhodamine 6G	23	2.56	95	14.2	64.8	21.9	18.8	11.8
Rhodamine 123	44	1.89	90	18.9	65.4	29	22.5	14.7
Rhodamine 110	84	5	94	34.7	72.4	48	31.1	31.5
Rhodamine B	13	6	53	6.2	76.3	8.2	6.1	5.7
Atto 488	67	4	80	52.5	85.7	61.2	17.5	46.3
Eosine Y	37	0.001	22	0.3	34	0.9	0.9	0
Rose Bengal	6	0.4	5	45	98.3	45.8	0.1	15.2
514nm								
TMR	40	2.5	28	8.6	56.6	15.1	8	7.1
Fluorescein	41	1.89	71	68.2	95.4	71.4	5.6	51.2
Rhodamine 6G	54	2.56	95	26.5	64.8	40.9	35.1	21.9
Rhodamine 123	82	1.89	90	29.1	65.4	44.5	34.6	22.5
Rhodamine 110	35	5	94	20.9	72.4	28.8	18.7	19
Rhodamine B	37	6	53	16.4	76.3	21.5	16.1	15.1
Atto 488	51	4	80	47.8	85.7	55.8	15.9	42.2
Eosine Y	78	0.001	22	0.7	34	2.1	1.9	0
Rose Bengal	26	0.4	5	77.8	98.3	79.2	0.2	23.9
532nm								
TMR	56	2.5	28	11.6	56.6	20.5	10.9	9.6
Rhodamine 6G	99	2.56	95	36.6	64.8	56.5	48.5	30.2
Rhodamine 123	9	1.89	90	5.4	65.4	8.3	6.4	4.2
Rhodamine B	77	6	53	28.4	76.3	37.3	27.9	26.2
Atto 488	5	4	80	10.3	85.7	12	3.4	9.1
Eosine Y	90	0.001	22	0.8	34	2.5	2.3	0
Rose Bengal	27	0.4	5	78.9	98.3	80.3	0.2	24.1
633nm								
CY5	60	2	18	21.8	68.8	31.7	17.8	17.1

On the other hand, fluorophores with strong intersystem crossing due to a presence of heavy atoms within their chemical structure, such as Eosine and Rose Bengal are widely used as photosensitizers for singlet oxygen. For triplet lifetime imaging, they are hence expected to create a contrast even with low illumination intensities, due to their strong intersystem crossing rate. However, the heavy-atoms also shorten the triplet lifetime dramatically. Based on the available data, we can only speculate if the emission rate we would be able to collect and the contrast we would expect for these fluorophores is sufficient for triplet lifetime imaging or not.

3 Triplet lifetime imaging: The method

3.1 Setup

Our triplet lifetime setup was built for maximum acquisition speed in order to access fast kinetic processes related to oxygen consumption in muscle cells. Hence we focussed on a wide-field illumination approach. However, this means that a high-power laser is required in order to reach an illumination intensity at the sample stage which allows to excite the fluorophores close to saturation. For the life-cell imaging, we desired a field of view which allows to get several cells at once in focus, hence we have settled for an approximated area of approximately $300\mu\text{m}$ in diameter. Figure 3.1 shows an overview of our setup. We have used a Millenia Pro

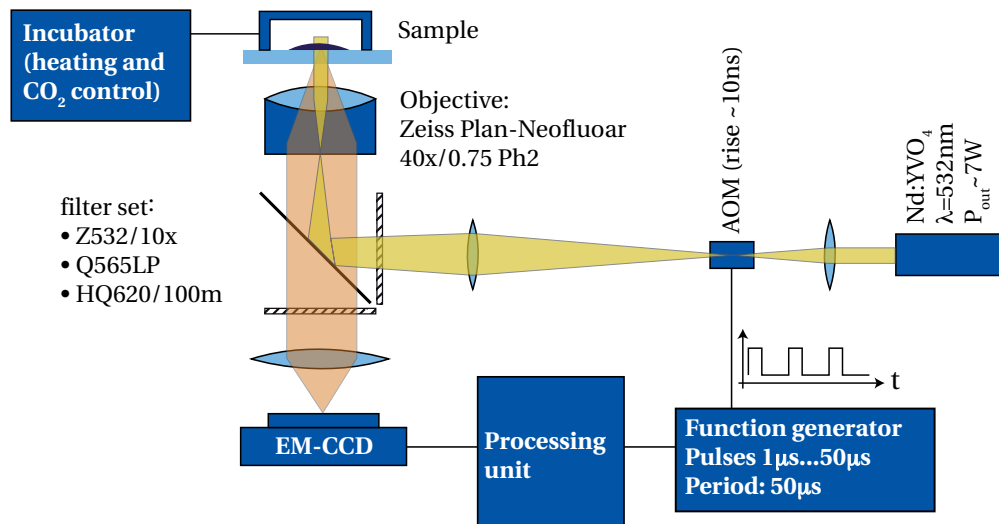


Figure 3.1: Schematic drawing of the triplet lifetime imaging setup. Beamshaping ensured a spot radius of $\approx 175\mu\text{m}$ at the sample plane, resulting in a maximum intensity of $\approx 0.6\text{mW}/\mu\text{m}^2$. The cell-incubator has been employed in a later stage of the thesis for the cellular uptake measurements but not for the oxygen consumption experiments.

Chapter 3. Triplet lifetime imaging: The method

10s Nd:YVO₄ laser ($\lambda = 532$ nm; Newport Spectra Physics) for our experiments. This laser offers up to 10W of output power, which is convenient for our whole field setup. The beam was focused to a radius of ≈ 175 μm in the sample plane, resulting in a maximum intensity of ≈ 0.59 mW/ μm^2 . Fast modulation of the laser beam was achieved by an acousto-optical modulator from Gooch&Housego (AOM M200-4B/E-LD4 with driver A341 for a rise-time of ≈ 10 ns). The pulse sequence was generated with a function generator (Agilent, 33250A 80 Mhz). Splitting and filtering of excitation and emission signals was achieved by filters from Chroma (Z532/10x, Q565LP, HQ620/100m) and the detection was done by an Andor Luca EMCCD camera.

All devices were controlled with a Matlab application enabling convenient and rapid acquisition.

3.1.1 AOM

The switching speed of the excitation modulation is mainly limited by the acousto-optical modulator. Although electro-optical modulators (EOM) can easily reach higher switching speeds (up to GHz), it is difficult and costly to design an electric driver for the EOM, which allows for both short as well as long pulses due to the high voltage requirement for the $\lambda/2$ modulation in the Pockel's cell. We choose an AOM as the more versatile option at a lower cost. The switching capability of the AOM is based on a travelling acoustic wave inside a crystal, which leads to local variations in the index of refraction, which leads to the creation of a diffraction grating along the crystal. The switching speed is hence related to the travelling speed of the acoustic wave. In order to speed up the modulation, one can focus the laser beam inside the AOM to reach transition times that can be of the order of few ns. However the focussing leads to a lower diffraction efficiency, because fewer "acoustic-wave-packages" are involved in diffracting the beam. Further on, the focussing increases drastically the required damage intensity threshold for the crystal. For the above mentioned reasons we have chosen a modulator from Gooch&Housego (AOM M200-4B/E-LD4). Focussing into the AOM results in a beam diameter waist of approximately 90 μm . This should in principle result in a 10ns rise-time for the laser modulation. However we have observed some non-linear effects related to the switching of the light with short pulses. As observed by the camera, it seems that the position of the illumination spot is different for very short pulses compared to pulses of 1 μs and longer. Figure 3.2 shows an overview of the observed effects. The effect is probably related to a slightly lower index jump at the onset of the acoustic wave inside the crystal [110]. But finding and further characterizing the exact physical reason behind the phenomena was out of scope for this thesis. As a conclusion we have limited our studies to pulses above 1 μs .

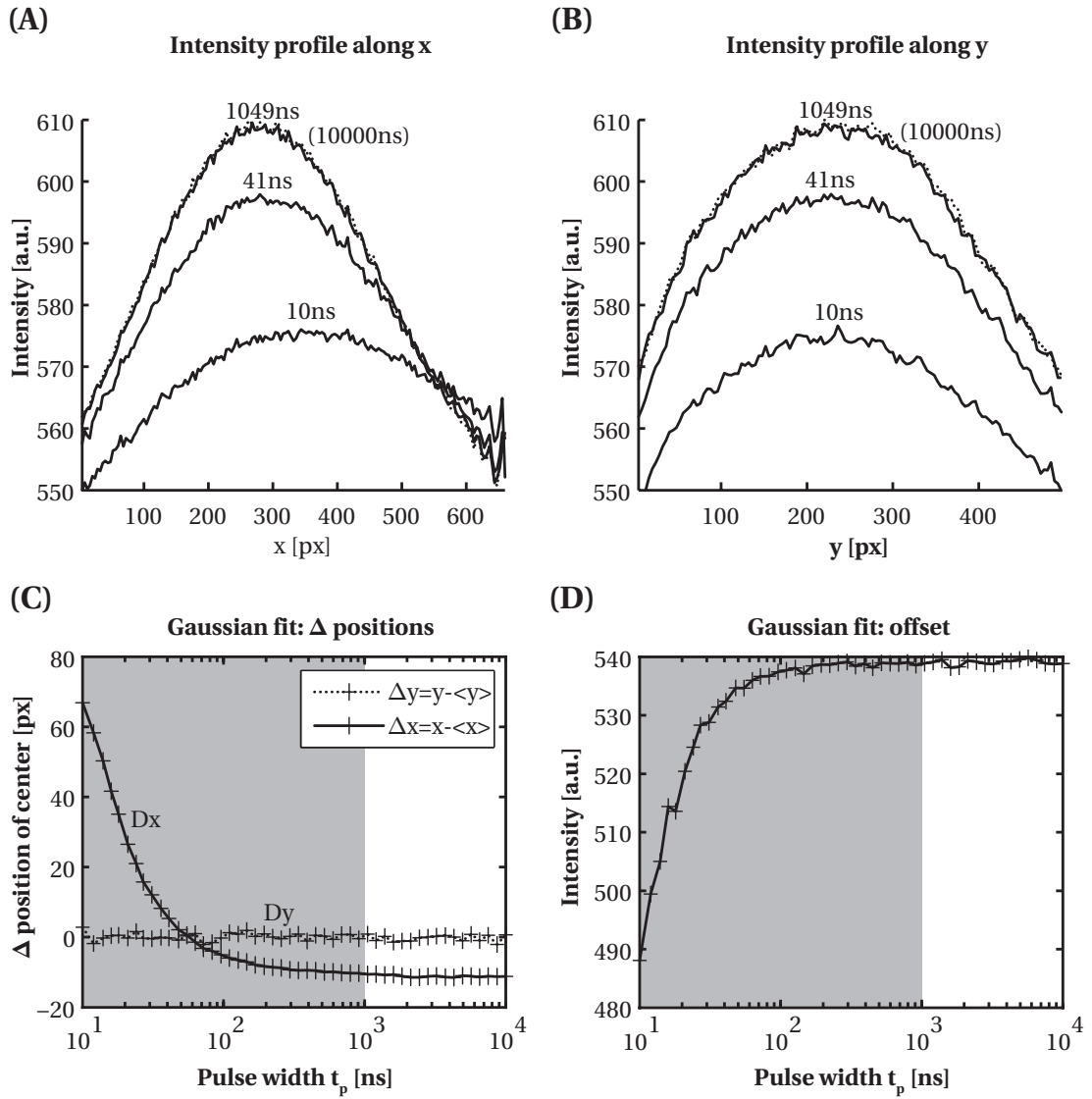


Figure 3.2: Assessment of the fast switching limitations of the acousto optical modulator (AOM). The measurement setup consisted of the laser at its usual employed power (7W) to keep any heat related effects on the AOM at the same level. A grey filter (ND=2) has been added just before the microscope in order to keep the intensity low (not to build up any triplet state of the fluorophores). The sample consisted of a simple droplet of 50nM TMR in H₂O. The AOM has been set to produce pulses of light between 10ns and 10μs with a repetition rate of 10μs. **(A-B)** show profiles of the intensity along the respective axis as seen by the camera. For every pulse length, a two-dimensional gaussian fit has been performed, yielding the position of the gaussian **(C)**, the offset **(D)** as well as the gaussian-width and -amplitude (not shown). As a conclusion from this measurement, we decided to discard any pulse lengths below 1μs as visualized by the grey box.

3.1.2 Phase contrast

The phase contrast method is a simple but powerful method to improve the sensitivity in transmitted light microscopy. An addition of a phase plate in the back aperture of the objective, allows to visualize otherwise transparent cells. The method is based on a ring illumination which is realized by a simple annulus shaped mask that is inserted in the Köhler illumination path at the position of the condenser diaphragm (see Fig. 3.3). The light transmitted directly through the sample is then filtered by a phase-plate. The phase-plate acts both on the phase and on the amplitude of the direct transmitted rays. The light is phase-shifted by a quarter wavelength ($\lambda/4$) – in most of the cases, the phase-plate gives rise to *negative* phase-contrast, which means that the light is *advanced* in phase with regards to the unaltered light, which stems from diffraction by the sample. An additional important effect of the phase-plate is to balance the direct transmitted light to the light intensity of the diffracted light by an annulus shaped neutral-density filter [111]. Figure 3.3 shows a complete simplified drawing of a phase-contrast microscope with the condenser annulus and the two components of the phase plate. In 1953, dutch physicist Frits Zernike, was awarded the nobel price for his invention of the phase contrast microscope [112, 113].

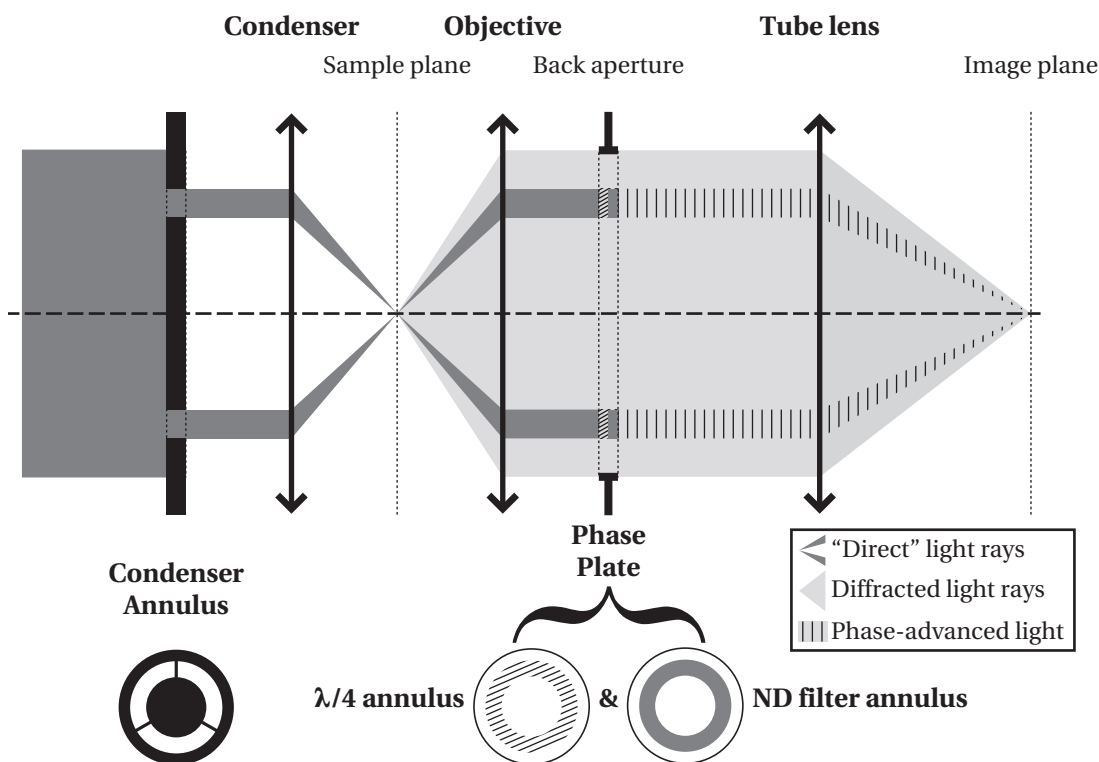


Figure 3.3: Phase contrast principle showing the annulus that is added to the condenser diaphragm to illuminate the sample by a ring-shaped pattern. The direct transmitted light is altered by a phase-plate both in phase and amplitude to create a balanced interference with the diffracted light at the image plane, leading to a contrast based on the phase of the sample [111].

For the triplet lifetime imaging setup, we have included the phase-contrast modality, since it is a very convenient way to get an additional contrast from your sample without adding another fluorescence labeling. In practice it has proven very helpful to find the cells of interest. As example, figure 3.4 demonstrates that the pure fluorescence image can sometimes be misleading, since the signal seen from an artifact *looks* very similar to the signal of an adhering and healthy cell. Only the addition of the phase-contrast allows to tell what we are actually looking at.

We have made two little simple modifications to the phase-contrast modality of our microscope. An emission filter limits the light exciting the sample in transmission to wavelengths that do not excite the fluorophores: this reduces photobleaching during the search for the most suitable cell for imaging. Additionally we have also included a blade that limits the phase-contrast illumination to half of the field-of-view. This allows a half-half image split: on the left the fluorescence image, on the right the phase-contrast image. This mode allows for very quick screening for cells both in phase contrast and fluorescence at the same time without the need of changing any filters or mirrors and proved very helpful for gaining speed during the measurement sessions.

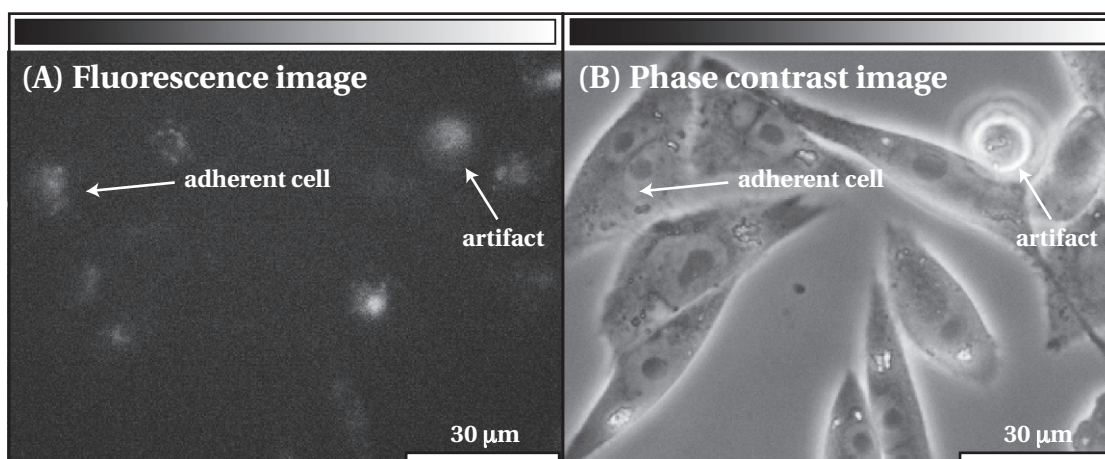


Figure 3.4: Two images of the same area of adherent CHO cells incubated with TMR-labeled transferrin for 10min. **(A)** Fluorescence intensity image and **(B)** phase contrast image. The image demonstrates how it can be difficult to distinguish between artifacts (non-adherent or dead cells) and "healthy" adherent cells just by using the information from the fluorescence image.

3.1.3 Bleaching

Since our method is based on relative differences in intensities, bleaching plays a crucial role, since it will also affect the measured differences: if we are no longer looking at the same number of molecules at the end than we have been observing in the beginning of an acquisition, our perceived difference will be biased. Since we are not looking at a sample in

Chapter 3. Triplet lifetime imaging: The method

solution where there is a continuous refreshment of fluorophores but rather at a more or less stationary labeled cell, the bleaching has to be taken into consideration in our estimation. We did so, by *interlacing* the image acquisition at different pulse widths with measurements at a reference pulse width (the shortest). This gives as a repetitive measure for how many still active fluorophores do we still have in our sample.

3.1.4 Image acquisition parameters

The image acquisition has several parameters that must be defined. Here's a list of all these parameters with the "standard" values employed most of the time followed by a short explanation of how and why we chose them.

t_{ill} The total time of illumination, the cumulated dosis of all pulses per pulse pattern \rightarrow 0.1ms

I_{laser} The laser intensity \rightarrow 7W, resulting in $0.6\text{mW}/\mu\text{m}^2$ at the sample

T_p The length of period from pulse to pulse \rightarrow 50 μs

t_p The range of different pulse lengths \rightarrow 1 to 50 μs

N_{im} The number of images, eg the number of different pulse widths t_p and the distribution type, eg differences between pulses (linear, logarithmic, custom) \rightarrow 11 images with linear spacing

N_{bl} The number of interlaced bleaching assessment images, at the shortest pulse width \rightarrow every fourth image, resulting in 4 bleaching assessment images

The first two parameters are somehow related: the image quality in terms of signal to noise ratio has to be good enough. Keeping the later constant, we can hence expose for a longer time at lower laser intensity, or rather expose for a shorter time at a high laser intensity. As visible on Fig. 2.8 on 21, the contrast we can expect between the image at the shortest pulse length and the image at the longest pulse width is much higher, when using higher laser powers. However we have also discovered that the bleaching is stronger at very strong laser powers, which is why we have settled for a compromise at 7W combined with a total illumination time of 0.1ms.

Figure 3.5 shows an overview of the effect on the available contrast depending on the pulse period T_p that has been employed. Due to this, and due to some simulation tests where we varied the period and looked at the capability of our fitting algorithm to find the correct τ_T for simulated intensity data in noisy conditions, we have settled for a value of $T_p = 50\mu\text{s}$.

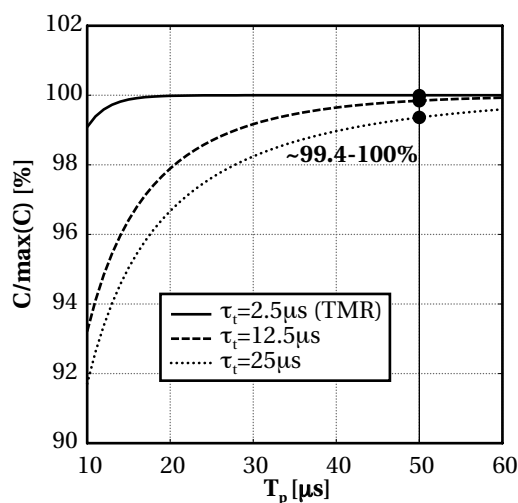


Figure 3.5: Graph demonstrating the available triplet contrast for different pulse periods T_p . The contrast is defined as a ratio between the intensity at the shortest pulse and the intensity at the longest pulse as defined in equation 2.9. The simulation has been done with standard values of TMR and two hypothetical cases where the triplet lifetime would be 5 and 10 times longer than in the TMR case. For each case, T_p has been varied between 2 and 200 μ s, the displayed graph is the calculated contrast divided by the highest available contrast for the respective triplet lifetime, resulting in the percentage of available contrast. This demonstrates why we have settled for a period of 50 μ s in our measurements where we reach more than 99% of the contrast for a broad range of triplet lifetime values.

The pulse widths t_p can be varied from any value between 1 μ s to the full period length T_p resulting in a cw excitation. For our experiments we have mostly employed the full range 1-50 μ s with a linear spacing between the different pulse widths. In order to keep the illumination dosis exactly the same, we modified the number of pulses accordingly. However since for long pulses, the discretization of the number of pulses makes it difficult to achieve a specific light-dosis, we have re-adjusted the exact pulse widths in a second step to match the exactly correct light dosis for the given number of pulses. Our measurement configuration led to a linear increase of the duty cycle. T. Spielmann showed in the continuation of this work that by keeping the duty cycle low and constant and going for even longer pulses (up to several ms), one can assess longer-living transient states of fluorescent molecules, namely the very long-living photo-oxidized radical state [114]. Figure 3.6 shows the modified Jablonski diagram with the added fourth anionic state. These long-living photo-oxidized states are of particular interest for the super-resolution microscopy community. Careful control of the oxidation and reduction rates by chemical buffers allows to make the fluorescent molecules "blink" in the time-scale of the frame-rate of a CCD camera [115, 116]. The concept of super-resolution based on stochastic fluctuations is further explained in chapter 5.

Finally the number of images $N_{im.}$ and bleaching assessment steps $N_{bl.}$ can be chosen rather freely. The more points we measure, the more reliable the fitting is, however the main limitation is the photobleaching of the sample. We have settled for a typically 9-11 images for

the number of different pulse widths as well as interlaced bleaching assessments every fourth image, resulting in typically 4 images.

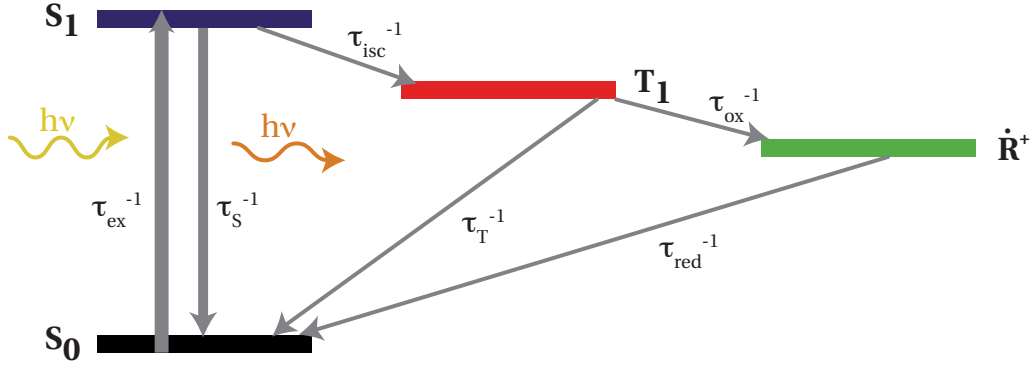


Figure 3.6: Modified 4-states Jablonski diagram including an additional long-living anionic radical state \dot{R}^+ . Triplet lifetime imaging or transient state monitoring (TRAST) allow to measure this long-living states by some small modification in the measurement parameters and the fitting model [114].

3.2 Image processing

In order to extract the triplet lifetime, extensive image processing is necessary as illustrated schematically in Fig. 3.7.

Most importantly, the intensity decrease due to photo-bleaching needs to be clearly separated from the triplet lifetime kinetics related decrease. For this purpose we estimated bleaching by interlaced "bleaching" measurements at the shortest pulse width. The measured photo-bleaching curve (Fig. 3.7, green curve) was modeled by a decaying exponential and fitted using an efficient algorithm based on the Poisson noise assumption [117]. The fitted decay parameters were then used to correct the modulated excitation response curve (Fig. 3.7, blue curve).

The next processing step was a pointwise fitting of the triplet lifetime or a fitting over a region of interest (ROI) of both the triplet lifetime and triplet yield. For the first we fixed the values for the singlet lifetime τ_{10} , the triplet yield Φ_T as well as the excitation rate $\tau_{ex} = \tau_{ex}(\vec{r})$. We assumed τ_{10} and Φ_T to be constant over the whole image. For TMR, we measured $\tau_{10} = 2.3$ ns on a dedicated fluorescence lifetime setup [118] with single photon counting capability (Picoquant Sepia II ps laser LDH-D-C-470; MPD PDM 50ct; Picoquant PicoHarp 300). The same fluorescence lifetime value for TMR was also measured by [92]. The absorption cross section has been estimated using the absorption spectrum (Invitrogen) and a published value for TMR of $\sigma_{10}(\lambda = 515 \text{ nm}) = 1.33 \times 10^{-16} \text{ cm}^2$ [92]. We used an absorption cross section of $\sigma_{10}(\lambda = 532 \text{ nm}) = 1.86 \times 10^{-16} \text{ cm}^2$.

For the cell images, where we fitted the triplet lifetime only, the intersystem crossing rate for a particular experiment was estimated by a global fit over several cells of k_{isc} and τ_T . Since the intersystem crossing rate could vary between different biological cells, we repeated this global fit for every experiment. For improved reliability we took typically 3-5 measurements of a particular cell and k_{isc} was set to the average of these measurements for an experiment. Since the diameter of our excitation spot was smaller than the size of our image, the spatial profile of the excitation rate had to be taken into account. We assumed a gaussian illumination profile whose position and beam width were estimated using a uniform layer of TMR deposited on a cover slide and bound to it. However, fitting a gaussian profile to the measured intensity did not lead to satisfactory results for τ_T over the whole range of the image. Hence an iterative fit of the triplet lifetime was used to optimize the excitation beam profile parameters in order to obtain a homogeneous triplet lifetime, as one would expect in such an experiment. Fig. 3.8 shows the respective cross sections of the assumed excitation shape in comparison with the measured intensity profile. In order to determine not only the shape but also the value of the excitation rate, we measured the optical power transmitted through our system and calculated the maximum excitation rate at the center of the excitation spot.

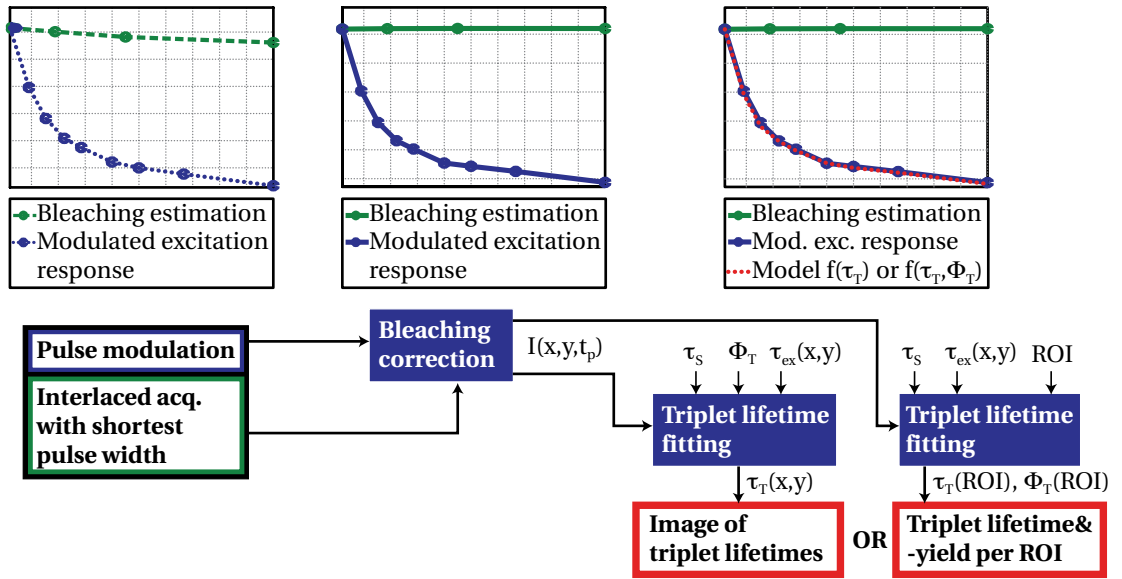


Figure 3.7: Image processing in triplet lifetime imaging. 1 - Photo-bleaching is assessed by fitting a mono-exponential decay to the measured bleaching estimation curve. 2 - All data points are normalized to the non-bleached fraction of fluorophores. 3 - Pixel per pixel, the triplet parameters are extracted from the image stack involving prior knowledge of the lifetimes τ_{10} , τ_{isc} and $\tau_{ex}(x,y)$.

For the pixel-by-pixel triplet lifetime fitting, the fit was reduced to finding two parameters for each individual pixel: the triplet lifetime τ_T and the factor γ , which is proportional to the intensity of a specific region. Fitting these two (non-linear) parameters by a standard optimization technique like the Marquardt-Levenberg algorithm is very slow and hence not suitable for processing an acquisition of 9 images containing 496x658 pixels. We circumvented

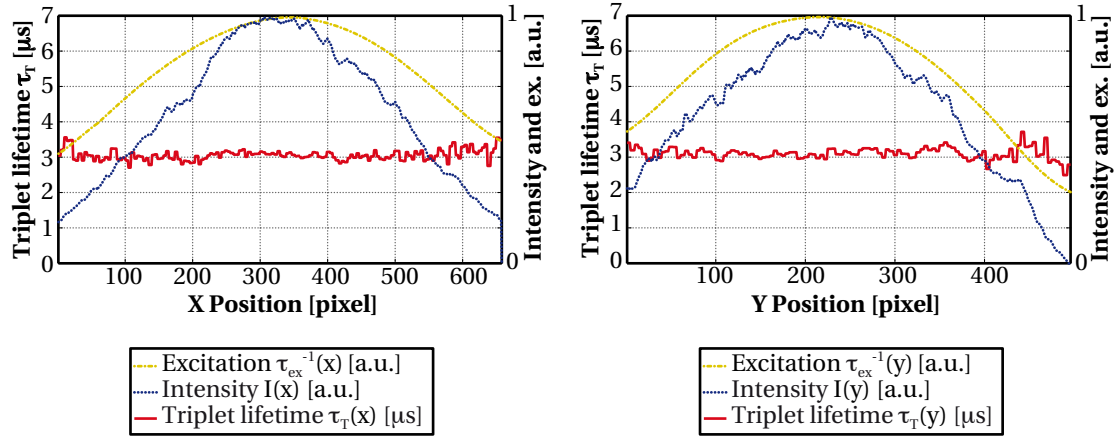


Figure 3.8: Excitation profile estimation in triplet lifetime imaging – Cross sections of the triplet lifetime fit in x and y directions (with the respective slice width and height of 30px) in comparison with the mean fluorescence intensity over all pulse patterns as well as the fitted gaussian excitation intensity.

this time consuming step and used an alternating least-squares approach for fast fitting. This resulted in typical fitting times of approximately 90 s for 152x115x9 pixels on a standard desktop computer (Intel Xeon 3.2 GHz, 2 GB RAM).

For the cell images we performed an averaging of the triplet lifetimes of three sequentially recorded measurements (2 s per measurement) in order to improve the measurement quality. For the measurements with of the oxygen consumption, we averaged the fitted triplet lifetime as discussed in section 4.1.3 on page 43. However for the uptake assessment, where movements are not to be expected between the sequentially recorded measurements, we found it more reliable to average the data before the fitting.

3.2.1 Image display

Appropriate display of the fitted results is of major importance to emphasize the meaningful data. Figure 3.9 shows an overview of the "problem": there are three different channels of information available. As for the case of fluorescence lifetime images, the triplet lifetime data is only meaningful over areas with fluorescence intensity above the background, because the lifetime is not defined otherwise. In figure 3.9 (B), the background areas show lifetimes similar to undefined white noise. To emphasize the meaningful data, the display has to be masked with the fluorescence intensity channel. This already requires hence two channels of information and prevents usage of pure gray-scale display. It is resolved by encoding the lifetime with different colors of the same intensity. The combination with the phase-contrast image in gray-scale reveals the full information in one single image.

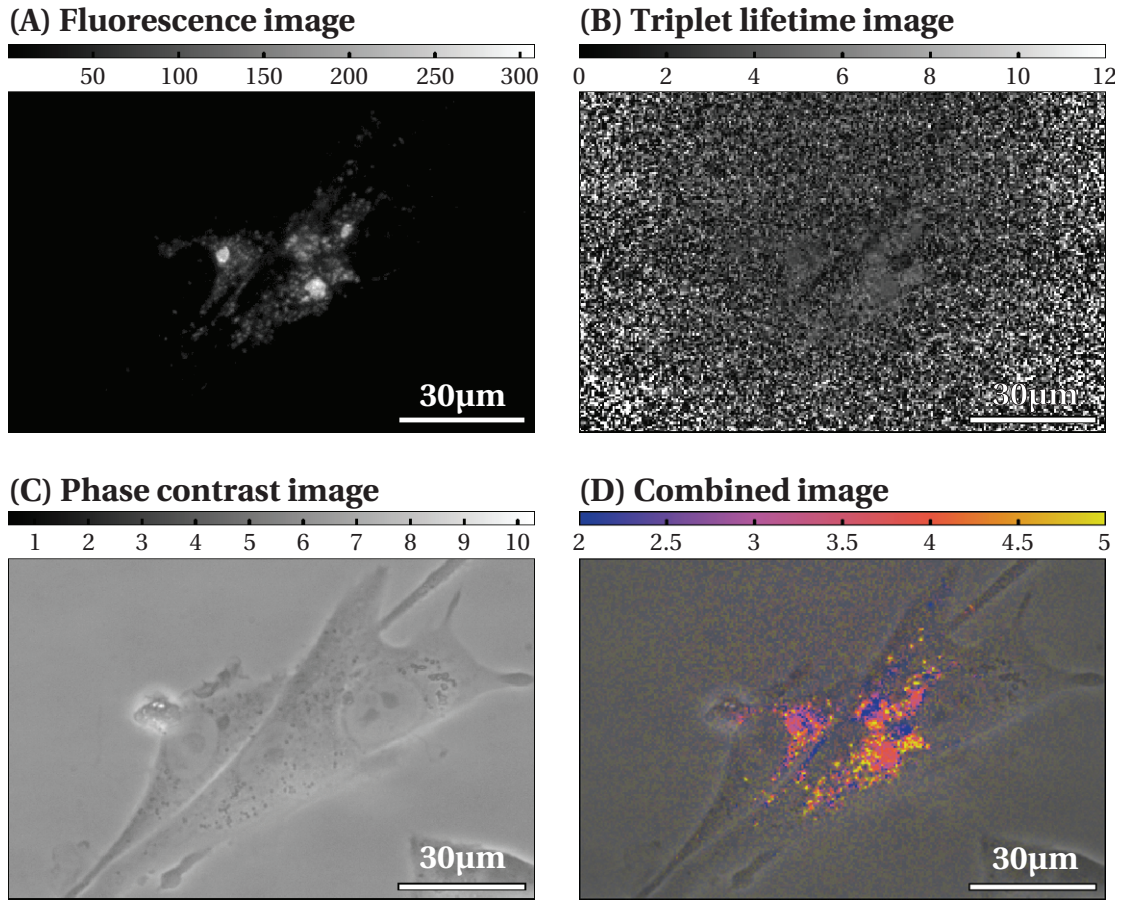


Figure 3.9: Displaying triplet lifetime images: a combination of three channels of information: (A) the fluorescence raw data, (B) the calculated triplet lifetimes for every point and (C) the phase contrast image. (D) The final combination of them involves a threshold and a gamma-correction of the fluorescence image, in order to yield a transparency mask for the triplet lifetimes that can be overlaid over the phase contrast image. The image shows a chinese hamster ovarian (CHO) cell that has been incubated with TMR-labeled transferrin for 10min.

3.3 Model system: TMR on cover slide

Fig. 3.10 shows a typical modulated excitation response and a bleaching estimation curve for a measurement of a TMR layer adhering to a glass cover slide. With the bleaching estimation, photo-bleaching could be taken into account accurately as shown by the corrected fluorescence responses. By global fitting we found $\tau_{isc} = 1.17 \mu s$. The average triplet lifetime is around $\tau_T = 3.1 \mu s$. These values are comparable to values measured for TMR in solution: $\tau_{isc} = 1.85 \mu s$ and $\tau_T = 2.5 \mu s$ [92]. The cited values were measured with fluorescence correlation spectroscopy (FCS) and varying excitation intensity [68]. The differences from our results are probably due to higher order artifacts as described in the discussion.

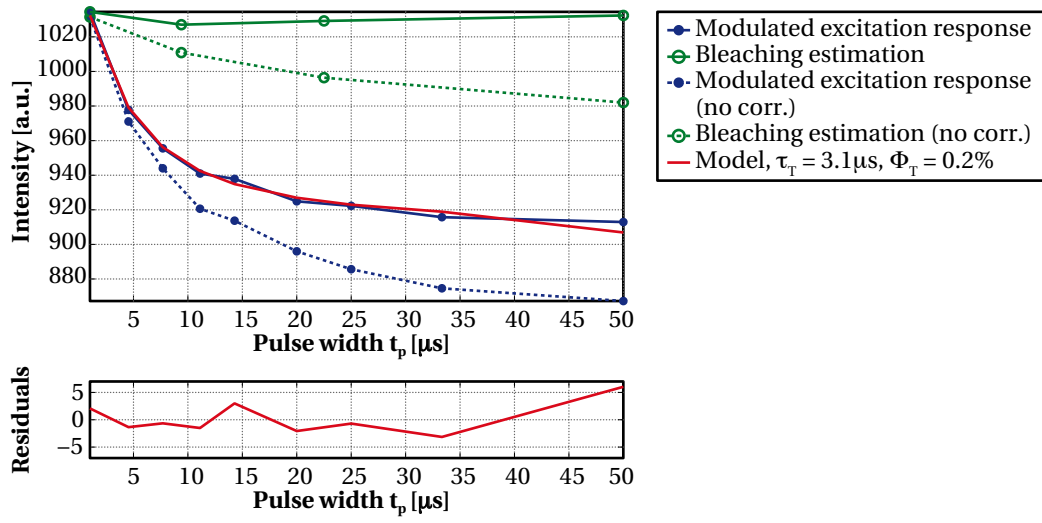


Figure 3.10: Observation of TMR adhering to a glass cover slide with a water droplet on top of the fluorophores. Measurement parameters: $t_p = 1\text{-}50\mu\text{s}$, $T_p = 50\mu\text{s}$, $P = 7\text{ W}$, $t_{\text{ill.}} = 0.1\text{ ms/pulse pattern}$, 9 images measuring the response to a modulated excitation and 4 bleaching estimation images acquired at the shortest pulse width. The curves are based on a spatial average over 30×30 px in the center of the acquired images. The bleaching estimation measurement points have been plotted in order to reflect the moment they have been taken and not at their specific pulse width of $1\mu\text{s}$. Global fitting over the whole image lead to $\Phi_T = 0.2\%$ and localized fitting to an average of $\tau_T = 3.1\mu\text{s}$.

4 Triplet lifetime imaging applications

4.1 Oxygen consumption imaging

The relationship between the concentration of a quencher (oxygen) and the triplet lifetime is described by the Stern-Volmer equation [119, 120]:

$$\frac{\tau_{T0}}{\tau_T} = 1 + k_q \tau_{T0} [O_2] \quad (4.1)$$

where τ_{T0} is the triplet lifetime in the absence of the quencher and k_q is a quenching constant obtained by the Smoluchowski equation:

$$k_q = 4r\pi R(D_F + D_Q)N_A \times 10^3 \quad (4.2)$$

where D are the diffusion coefficients of the quencher and the fluorophore, R is the radius of interaction between quencher and fluorophore, r is the quenching efficiency and N_A is Avogadro's number.

Both constants τ_{T0} and k_q need to be known precisely in order to obtain an accurate relation between triplet lifetime τ_T and oxygen concentration $[O_2]$.

In the presence of reducing and oxidizing systems there exist alternative relaxation pathways for the triplet state as has been demonstrated by Rehm and Weller [121]. In more recent work, this knowledge has been exploited for improved photostability [116, 122]. Biological cells are complex systems with many different organelles and local environments, including different reducing and oxidizing systems. Further, a cell cannot be considered as a homogenous medium and hence we also expect varying diffusion constants. At present, it is not possible to determine $\tau_{T0} = \tau_{T0}(\vec{r})$ and $k_q = k_q(\vec{r})$ in a precise manner for all different and non-stationary

Chapter 4. Triplet lifetime imaging applications

organelles of a cell. Therefore, we propose to limit the observation to the triplet state relaxation rate k_T , which is the inverse of the triplet lifetime:

$$k_T(\vec{r}) = \frac{1}{\tau_T(\vec{r})} = \frac{1}{\tau_{T0}(\vec{r})} + k_q(\vec{r})[O_2(\vec{r})] \quad (4.3)$$

Assuming that a variation in the concentration of the quencher does not influence $\tau_{T0}(\vec{r})$ nor $k_q(\vec{r})$, we may express the variation of the concentration as:

$$\frac{d}{dt} \{k_T(\vec{r})\} = k_q(\vec{r}) \frac{d}{dt} \{[O_2(\vec{r})]\} \quad (4.4)$$

In other words, the variation of the quencher concentration $\frac{d}{dt} \{[O_2]\}$ is proportional to the variation in the triplet relaxation rate $\frac{d}{dt} \{k_T(\vec{r})\}$.

4.1.1 Calibration experiment: triplet lifetime versus oxygen concentration

Materials and Method

Adhesion of TMR (5-(and-6)-carboxytetramethylrhodamine, succinimidyl ester (5(6)-TAMRA, SE), Invitrogen) on a glass cover-slide has been done by using bovine serum albumin (BSA) as intermediate linker between the glass cover-slide and the TMR-molecules: after deposition of a droplet of BSA on a glass cover slide, the slide was washed with 3 ml deionized water. In a second step a droplet of TMR was applied. After 1 minute the solution was washed with 5 ml deionized water. These test samples were covered with water during the measurements, either with a droplet of water on top or by putting the slide inside a flow cell containing water.

We used the enzyme ascorbase (Sigma-Aldrich) for catalysis of the oxidation of L-ascorbic acid (Sigma Aldrich) according to the following reaction:



Titration of L-ascorbic acid removes oxygen from a solution in a controlled way [120]. The final reaction mix consisted of 3 ml H_2O , 10 units ascorbase (1 unit oxidizes 1 μ mole of L-ascorbic acid per minute), 20 mM sodium phosphate buffer and 0.05% (w/v) bovine serum albumin (BSA). Adding 300 μ l of a solution of 25.5 mM L-ascorbic acid removes all dissolved oxygen inside 3 ml of H_2O at room temperature provided that there is no re-oxygenation from the environment.

In order to minimize the oxygen uptake during the experiment, the observation was done in a custom-made PDMS-flowcell with an observation volume of $\approx 20 \text{ mm}^3$ connected by tubing with low gas permeability (Ismatec, Fluran HCA with inner diameter of 0.89 mm) to a peristaltic pump (Ismatec Reglo Digital) at 1.5 μ l/s. The solution reservoir was placed in a

larger container connected to a low continuous flow of nitrogen. The L-ascorbic acid doses were added with a syringe through a tiny access hole in the container. This model system allowed a verification of the acquisition method and the fitting algorithm for different oxygen concentrations.

Experiment

We performed calibration experiments by lowering the dissolved oxygen concentration in discrete steps by titration of L-ascorbic acid. In parallel to the triplet lifetime acquisitions, the dissolved oxygen concentration was monitored with an oxygen probe as reference (SG6 Seven Go Pro dissolved oxygen meter with InLab 605 sensor, Mettler Toledo). As shown in Fig. 4.1 A, the probe revealed the linear decrease in dissolved oxygen as expected in theory, which demonstrates that the titration of L-ascorbic acid is indeed proportional to the removed amount of dissolved oxygen. The graph of the triplet state relaxation rate k_T ($= 1/\tau_T$), Fig. 4.1 C, also demonstrates a linear relationship, which suggests that the molecules' response to oxygen can be described by the Stern-Volmer model. This proves that TMR as reporter molecule measured with our method works well for determining different oxygen concentrations. However, despite a minimized surface in contact with air, re-oxygenation of the sample could not be prevented totally. Due to this, the titration of 300 μl L-ascorbic-acid did not remove all oxygen in the solution. Nevertheless, the experiment allowed us to measure the response of our system in physiological conditions and it demonstrates nicely the linearity of the quenching mechanism.

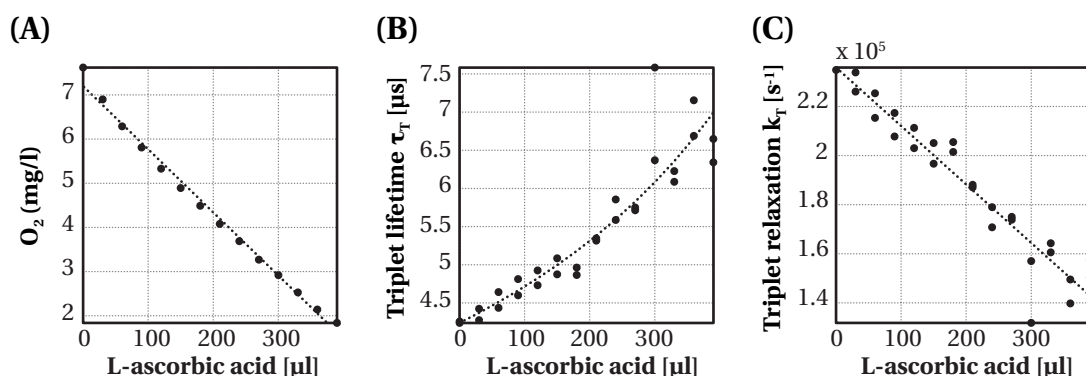


Figure 4.1: Observation of TMR adhering to a glass cover slide in a flow cell setup with ascorbase in solution. Titration of 25.5 mM L-Ascorbic-Acid removes the oxygen in controlled discrete steps. (A) Dissolved oxygen as measured by a commercial probe (Mettler Toledo). (B) Triplet lifetime measurement using an average intersystem crossing of $\tau_{isc} = 0.69 \mu\text{s}$ obtained by a global fitting over 7 measurements. (C) Triplet state relaxation rate $k_T = \tau_T^{-1}$.

4.1.2 Smooth muscle cells from rat thoracic aorta (A7r5)

To test our triplet imaging method in a biologically relevant context, we performed AVP stimulated contraction experiments with rat thoracic aorta smooth muscle cell line A7r5 [123] (Promochem; CRL-1444). Figure 4.2 shows a phase contrast image of the employed cell type. The cells have been labeled with TMR linked to SNAP-tag- β -galactosidase which is a cytosolic protein linked to a tag for labeling [124]. Figure 4.3 shows an overview of the SNAP-tag labeling technique.

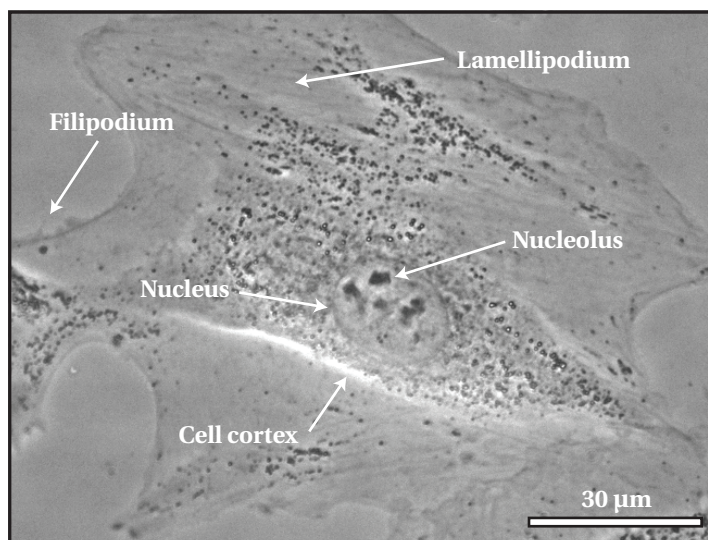


Figure 4.2: Phase contrast image of a smooth muscle cell from rat thoracic aorta (A7r5). This cell type has been used for the oxygen consumption application.

The cells have been cultured in Dulbecco's modified eagle medium (DMEM, GIBCO; 41965) supplemented with 10% fetal calf serum (FCS). We used two different labeling protocols: one to realize transient transfections and one for stable transfections. For the stable transfection we used A7r5 cells stably transfected with pNuc SNAP β -gal plasmids expressing a fusion protein of SNAP-tag and β -galactosidase (SNAP- β -gal); SNAP-tag fusion proteins can be specifically labeled with different fluorophores in living cells [125]. Stably transfected clones expressing SNAP β -gal fusion proteins were selected by adding 2 mg/mL G418 (Geneticin disulfate salt, Sigma; G5013) to the culture medium.

For the transient transfection we used the same A7r5 cell line that we transfected according to a standard transfection protocol using the Jet Pei technique (Polyplus transfection; 101-05) with 2 μ g plasmid DNA per 35 mm dish. The transient transfections were started 24-48 h before the experiment.

Two days prior to the experiments, respectively one day before the transfection, the cells were transferred into 3.5 cm microscope observation dishes (Ibidi) coated with collagen.

The day of the experiment, cells were labeled by loading the dishes for 5 minutes at room temperature with 200 μL of a solution of 1 μM TMR-Star (Covalys; LK040) in DMEM with 10% FCS. Cells were then washed three times in DMEM with 10% FCS then incubated for 5 minutes at each step at 37 °C. Finally the cells were incubated for at least three hours until the experiment. Before measurements the medium was replaced by a Hank's Buffered Salt Solution (HBSS, GIBCO).

Cell contraction was induced using [Arg⁸]-vasopressin acetate salt (Sigma; V9879) at a final concentration of 500 nM AVP. This hormone is well known to initiate a vasoconstriction of the smooth muscle cells at this concentration [126, 127].

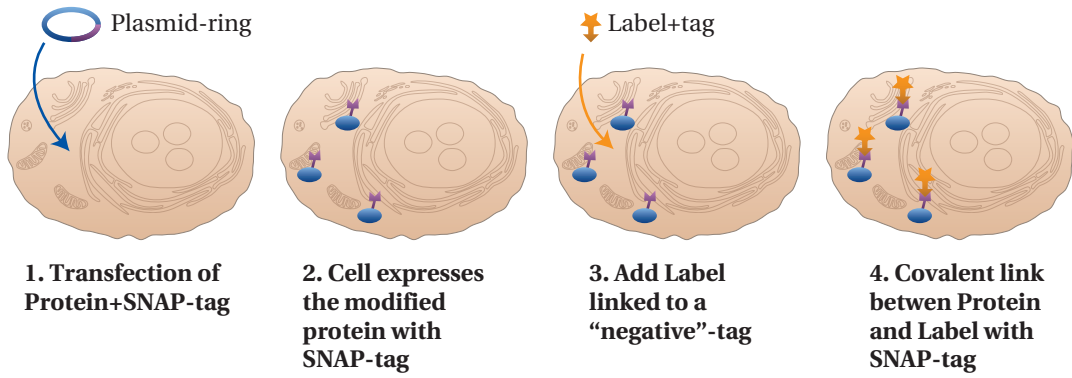


Figure 4.3: Principle of the SNAP-tag labeling technique. See Keppler et al. [125] for further details of this method.

4.1.3 Averaging of the data

The triplet relaxation values $\bar{k}_{T,i}$ shown in the temporal evolution of the contraction experiments, correspond to the mean values of three consecutive measurements ($k_{T,j}$ to $k_{T,j+2}$):

$$\bar{k}_{T,i} = \bar{k}_{T,i+1} = \bar{k}_{T,i+2} = 1/3 \times \sum_{j=i}^{i+2} k_{T,j} \quad \Bigg|_{i=1:3:(N-2)} \quad (4.6)$$

The standard deviations indicated for these measurements correspond to the mean standard deviations calculated over all measurements subtracted by these respective mean values:

$$s = \left(\frac{1}{N-1} \sum_{i=1}^N (k_{T,j} - \bar{k}_{T,j})^2 \right)^{1/2} \quad (4.7)$$

4.1.4 Triplet lifetime results

Fig. 4.4 shows two typical experiments. In Fig. 4.4 (A) and (C), the color encodes the different triplet lifetimes, whereas the intensity is proportional to the fluorescence intensity (as explained in Fig. 3.9). Two images are shown one before and one after the induced contraction. Fig. 4.4 (B) and (D) show the temporal evolution of the triplet relaxation rate over a selected area (white square on the corresponding images on the left side). As mentioned above the variation in $k_T = 1/\tau_T$ is proportional to the variation in the oxygen concentration. After global stimulation with 500 nM [Arg⁸]-vasopressin (AVP) the cells undergo a contraction. This leads to an oxygen consumption inside the cell, which can be observed on the temporal evolution of the triplet relaxation rate. In order to achieve longer measurement times and minimal phototoxicity for the cells, we have compromised the image quality slightly by reducing the excitation power. But one can easily obtain better resolutions and higher signal quality when using higher excitation levels.

All images have been recalculated for display in this thesis with a novel algorithm that takes the average of three acquisitions before the fitting. We have used a $\tau_{isc} = 1.85 \mu s$ corresponding to TMR in solution for all the images in this chapter.

The results of three measurements with global AVP stimulation are shown in Fig. 4.5 (A) in comparison with two negative controls without addition of AVP. In Fig. 4.5 (B) the temporal evolutions are normalized with respect to their initial and final steady states. For the negative controls we used a factor of 0.4×10^{-5} for the normalization corresponding to a typical difference between the steady state values before and after adding AVP. The temporal evolution presented in the three curves has been observed in 84% of the observed cells (n=25). The remaining 16% of cells did not show a visible decrease in triplet relaxation rate after the addition of AVP similar to the negative control experiments (n=5).

Discussion

The L-ascorbic acid titration experiment (Fig. 4.1) demonstrates that the proposed method is able to determine variations in oxygen concentration. The sensitivity of this method is not as good as in other methods [39, 47, 120]. However the high intensity of the fluorescence signal enables a combined performance of temporal and spatial resolution well beyond what can be achieved with methods based on phosphorescence quenching or on other mechanisms leading to low intensity signals.

Since high laser excitation power is required to increase the contrast based on the triplet state buildup, we reduced the acquisition times such that there is illumination during only 1.2 ms per acquisition of 12 images. Despite using a fairly photostable fluorophore, bleaching has been an important issue. Typically at the end of an experiment (after around 30 acquisitions

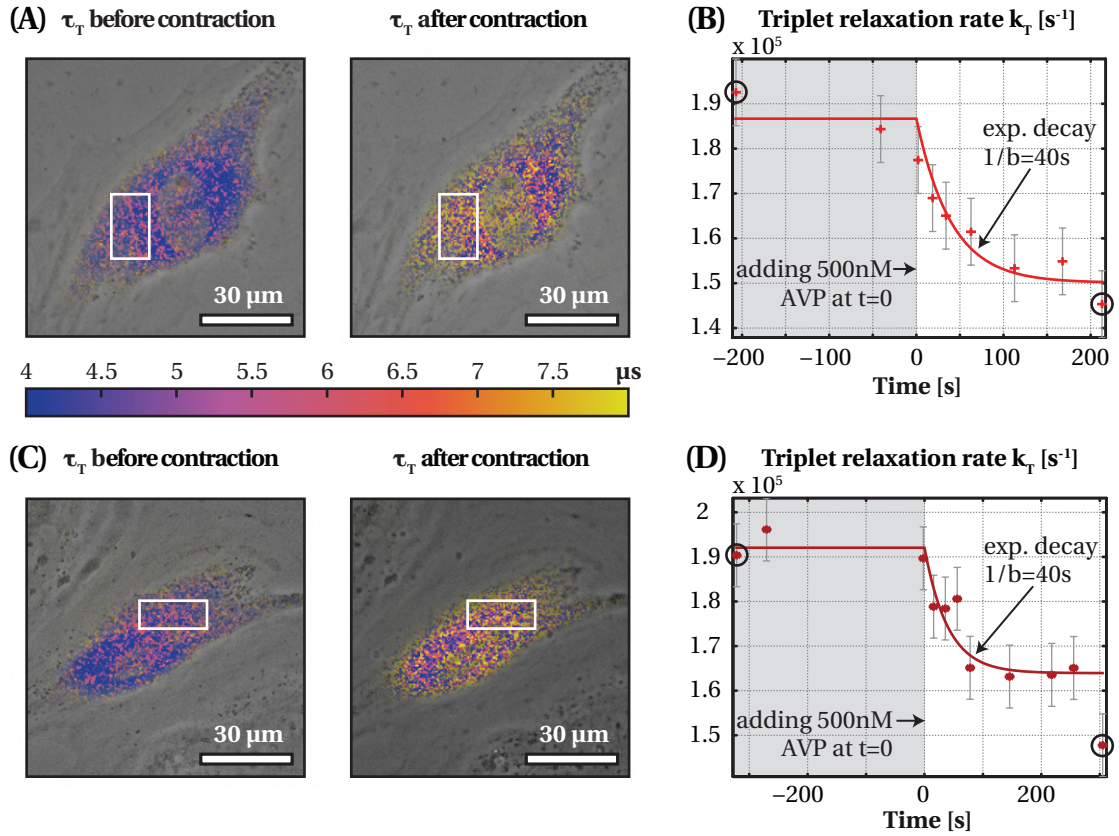


Figure 4.4: Two experiments on contraction of smooth muscle cells A7r5 with transient transfections of the cytosolic fusion protein β -galactosidase (SNAP- β -gal) employed for the labeling with TMR. Contraction was initiated with [Arg⁸]-vasopressin (AVP). (A) and (C) Triplet lifetime image with color encoded lifetime. (B) and (D) show the temporal evolution of the average triplet relaxation rate for the region inside the white rectangle. The result indicates a variation in the oxygen concentration following a monoexponential decay (the approximate decay parameter was estimated from multiple experiments). We used for (B): $\tau_{isc} = 2.12 \mu s$ and for (D): $\tau_{isc} = 2.01 \mu s$, both values were obtained by global fitting on several measurements. The image quality was optimized for multiple measurements.

of 12 images each), the fluorescence signal corresponds to about 20% of the initial intensity, limiting the total number of acquisitions that can be made on the same cell. Nevertheless, the proposed functional imaging method was successfully applied in a study of oxygen consumption during drug-induced contraction of single smooth muscle cells (Fig. 4.5). In most cells we measured mono-exponentially falling intracellular oxygen concentration without initial delay upon the addition of 500 nM AVP. On average we found a typical decay constant of ≈ 40 s for these cells. These positive results can be compared to experiments where no AVP was added (Fig. 4.5 cells 4 and 5).

Triplet lifetime images of cells (Fig. 4.4) reveal areas of long (yellow-red color code) and short triplet lifetimes with heterogeneous cellular distribution. In general, these areas indicate different oxygen concentrations as well as different local environments of the dyes. Biological cells

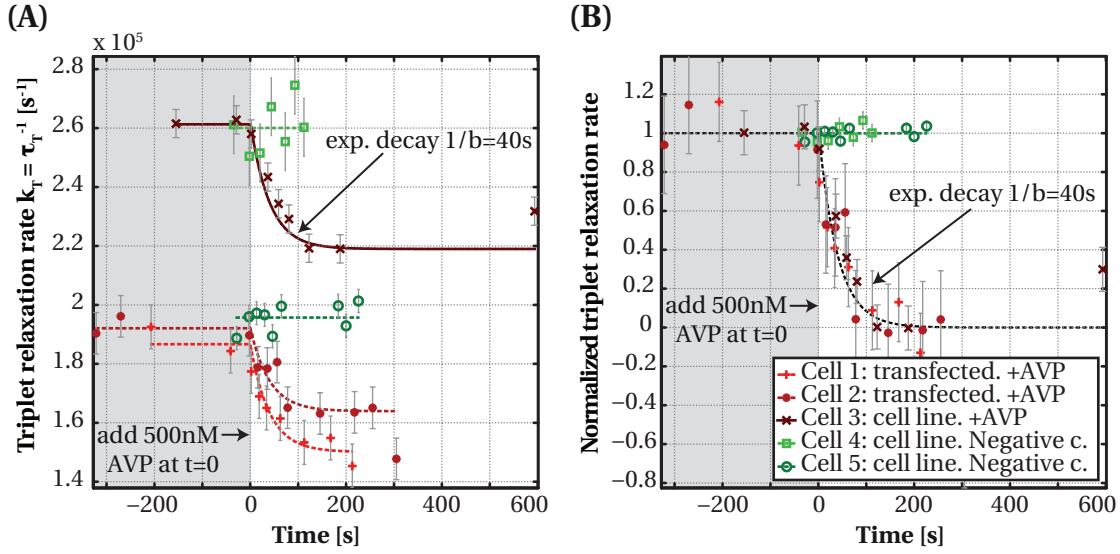


Figure 4.5: Three experiments on contraction of smooth muscle cells A7r5 upon addition of AVP and two negative controls where no AVP was added. (A) Average triplet relaxation rate measured on a small area inside the respective cells. (B) Relaxation rates normalized with respect to the initial and final steady state. For the negative controls we used a factor of 0.4×10^{-5} for the normalization corresponding to a typical difference between the steady state values before and after adding AVP. Global fitting was used to determine the respective intersystem crossing rates τ_{isc} leading to the following values: (Cell 1) $2.12 \mu\text{s}$ (Cell 2) $2.01 \mu\text{s}$ (Cell 3) $1.19 \mu\text{s}$ (Cell 4) $1.08 \mu\text{s}$ (Cell 5) $2.01 \mu\text{s}$.

contain various organelles and exhibit different sub-cellular compartments with corresponding dimensions that can locally influence the triplet state lifetime. In particular, organelles of the endosomal and lysosomal compartments are characterized by distinct pH. Large shifts in the pH could lead to noticeable changes in the triplet state of the dyes. Another explanation for these areas may be sites of mitochondria, the main oxygen-consuming organelles in a cell. This is corroborated by matching triplet lifetime images with phase contrast images, in which mitochondria appear as phase-dense circular structures with $\approx 1 \mu\text{m}$ diameter. Our data indicate that in sub-cellular areas with lower density of these structures, the corresponding triplet relaxation rate is significantly higher (see phase contrast image in 4.6, right of the nucleus). This example may indicate an intracellular oxygen gradient, created by the absence of mitochondria in this area. To this end, we can only reasonably speculate about the nature of the sub-cellular compartments coinciding with distinct triplet lifetimes. Further experiments using specific compartmental marker proteins will be needed to clarify their nature. We observed rather large differences between different cells in their triplet relaxation rate k_T as well as their intersystem crossing rate k_{isc} . When analyzing the deviating measurements we found differences in the bleaching correction in contrast to experiments that lead to $k_{isc} \approx 2 \mu\text{s}$. The deviating correction leads to a systematic small hump on the corrected modulated excitation response for pulse widths around $15 \mu\text{s}$ (as also visible in Fig. 3.10. This probably accounts for the higher intersystem crossing rates (and lower triplet lifetimes). We think the effect stems from higher order energy states that start to be populated for longer excitation pulses

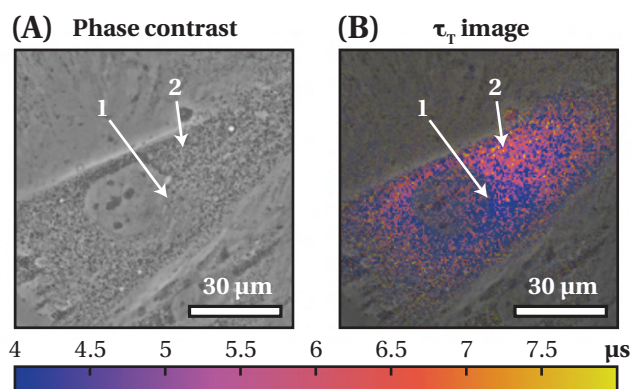


Figure 4.6: (A) Phase contrast of aTriplet lifetime image of A7r5 with varying cellular organelle density. Mitochondria appear as darker dense circular structures in phase contrast imaging. Region 1 seems to be less dense than region 2. (B) Triplet lifetime image with color encoded lifetime. Region 1 shows a lower triplet lifetime which could correspond *potentially* to an area with higher oxygen concentration. Is this an indication for the oxygen consumption activity of the mitochondria? Only further studies with specific compartmental markers could tell this for sure.

($t_p > 10 \mu s$). This would lead to an additional kinetic response upon modulated excitation which we have not taken into account in the current three state model. Correcting for this higher order effect would require a more advanced bleaching estimate measurement which is beyond the scope of this thesis.

As described above, there was an important decrease in fluorescence intensity over a full experiment. This led to difficulties in fitting low intensity measurements at the end of the experiment and explains the deviations of the two outliers at the very end of the measurement of cell 2 and 3. Hence the standard deviation as described in "materials and methods" is actually expected to grow with measurement time although the measurements themselves do not indicate it.

Our measurements demonstrate that the proposed method is well suited to address biological questions related to fast oxygen kinetics at the cellular and sub-cellular level. Our results are in accordance with previously reported measurements of oxygen consumption during contraction of skeletal muscle fibers of *Xenopus laevis* [128] as well as with indirect measurements of the oxygen uptake of single cells in a sealed chamber [57].

The method could be further refined by taking care of variations of the intersystem crossing rate k_{isc} during the experiment. Such effects could be caused by variations of the singlet oxygen concentrations. In some cases with strong labeling (eg. when labeling the cells with nuclear localized proteins) we did indeed see continuous variations of the intersystem crossing rate during the experiment that might have been due to increased photosensitized singlet oxygen. Taking into account higher triplet states might improve the parameter extraction but

Chapter 4. Triplet lifetime imaging applications

at the expense of a far more complicated fitting procedure and the potential risk of leading to a less robust fitting.

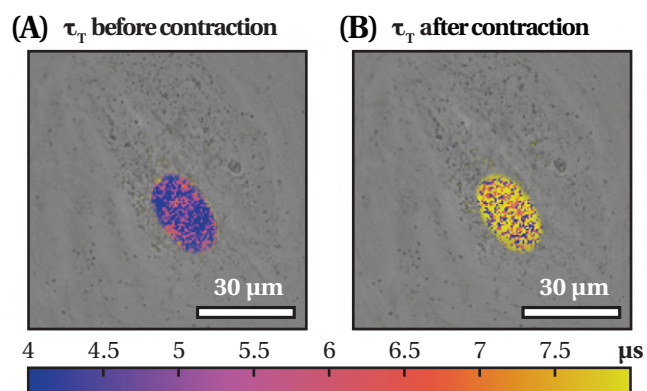


Figure 4.7: Triplet lifetime image with color encoded lifetime of A7r5 with a transient nuclear localization signal (NLS) SNAP-tag transfection before and after an AVP induced contraction.

4.2 Assessing the cellular uptake mechanism

One of the fundamental elements of biological cells, is the plasma membrane [129]. It encloses the cell, protects it from the outside and allows its functioning at the ion-concentration levels required by the cell. However the cell is not independent from the outside and requires certain ions, proteins and other molecules to pass its border and also to be able to dispose of waste that is produced inside the cell. As a result, the membrane cannot function as an impermeable boundary but as a *controlled selective barrier*.

There exists a multitude of transport mechanisms across the membrane. Ions are typically transported with the help of selective ion-channels; proteins undergo a receptor based uptake and larger molecules and particles are uptaken by endocytosis [129]. During the receptor based uptake, a ligand links to a binding-site of a membrane protein which undergoes a conformational change that delivers either the ligand or the receptor-ligand complex as a whole inside the cell. Alternatively the receptor can also be uptaken with the help of clathrin-coated pits to form a vessicle inside the cell (endosome). The receptor is often recycled back to the plasma-membrane in order to continue functioning.

The iron transport with the help of Transferrin is an example for such a receptor-based uptake with the help of clathrin-coated pits [130]. Transferrin is a serum-protein with two binding sites for Fe^{3+} -ions. It can bind to a transferrin-receptor (TfnR) within the plasma-membrane. With the help of clathrin-coated pits it is then internalized as a vessicle to form a so called early-endosome. The later contain a strong acidic environment which causes the relase of the iron from the transferrin [129, 130]. The iron-free transferrin (apotransferrin) is then recycled back to the plasma-membrane together with the receptor where they dissociate to release the transferrin to the outside of the cell (serum) from where the cycle can be re-initiated [130].

Two different recycling pathways have been identified: a fast recycling directly from early endosomes and a slow recycling via the perinuclear recycling compartment (PNRC) [131–133]. We have assessed this well known uptake&recycling pathway with the help of triplet lifetime imaging to demonstrate the usefulness of the technique in this context. Our results are based on differences in triplet lifetimes between the autofluorescence (background) and the TMR-labeled transferrin.

4.2.1 Materials and Methods

Cell cultivation

The experiments have been done with adherent chinese hamster ovarian cells (CHO) that have been seeded 24h prior to the experiment on micro-dishes with a coating for adherent cells (μ -Dish, #80136, Ibbidi). The cell cultivation was done in ProCHO5 supplemented with 10%

Chapter 4. Triplet lifetime imaging applications

fetal calf serum (FCS). Two protocols have been used for the experiments: an RPMI-protocol and an HBSS-protocol, which lead to identical measurement results. All employed media were warmed to 37°C before employing them in order to prevent thermal shocks for the cells.

Prior to the experiment, the cells were washed twice with either RPMI or HBSS and incubated for 5min at 37°C in the respective media to release membrane-receptor bound transferrin [130]. This step was followed by a 20min incubation in serum-free DMEM-medium at 37°C to "starve" them of transferrin (chase) before washing them again twice with RPMI or HBSS and incubating them again for 5min at 37°C in the respective media to remove any remaining membrane-receptor bound transferrin. The cells were then incubated for 7min (pulse) with DMEM containing tetramethylrhodamine (TMR)-labeled transferrin from human serum (T-2872, Invitrogen Inc.) at a concentration of 500 µg/ml. This was followed by washing them three times with ProCHO5+10% FCS. The measurements have been done in ProCHO5 with serum. We added a special cell-incubator to the triplet lifetime imaging setup for these experiments that controlled the environment at 37°C with 5% CO₂ and maintained a humid environment (see figure 3.1 for a drawing of the setup).

Triplet lifetime unmixing

Our results are based on differences in triplet lifetimes of two fluorescent species (autofluorescence vs label). In order to assess the quantity of each, an expression has to be found that allows *unmixing* of the measured triplet lifetimes based on the known triplet lifetimes of each species.

Ideally, the derivation would start from equation 2.7 by writing the sum of intensities of two individual fluorophore contributions and comparing them for every different pulse length t_p . However, the complexity of the equation prevents to derive a simple analytical expression for the unmixing. As a simple but powerful alternative, we propose to start from the expression for the relative triplet population (eq. 2.6) and describe the mixing simply with the help of this expression. Figure 4.8 shows an overview of the idea. Hence

$$\begin{aligned} P_T^{\text{eq, sum}} &= \alpha P_T^{\text{eq, dye}} + (1 - \alpha) P_T^{\text{eq, autofluorescence}} \\ \frac{\Phi_T \tau_{T, \text{sum}}}{(\tau_{\text{ex}} + \tau_S + \Phi_T \tau_{T, \text{sum}})} &= \frac{\alpha \Phi_T \tau_{T1}}{(\tau_{\text{ex}} + \tau_S + \Phi_T \tau_{T1})} + \frac{(1 - \alpha) \Phi_T \tau_{T2}}{(\tau_{\text{ex}} + \tau_S + \Phi_T \tau_{T2})} \end{aligned} \quad (4.8)$$

This equation can easily be solved for α to reveal a simple analytical expression that describes the proportional amount of the dye (species 1) with respect to the autofluorescence (species 2) based on a mixture of the two species

$$\alpha = - \frac{(\tau_{T2} - \tau_{T, \text{sum}})(\tau_{\text{ex}} + \tau_S + \tau_{T1} \Phi_T)}{(\tau_{T1} - \tau_{T2})(\tau_{\text{ex}} + \tau_S + \tau_{T, \text{sum}} \Phi_T)} \quad (4.9)$$

The above equation allows to determine the *proportional* amount of dye versus autofluo-

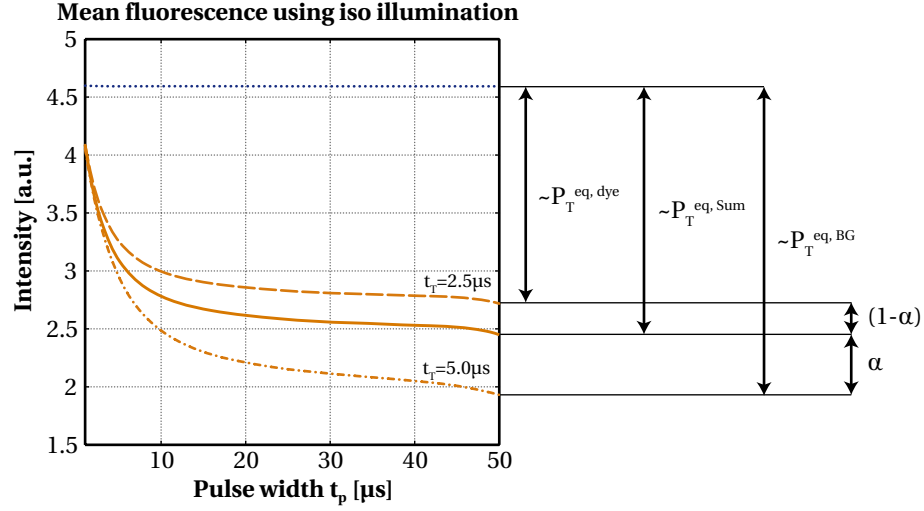


Figure 4.8: Unmixing of two known triplet lifetimes with the help of the triplet population for a constant excitation at equilibrium P_T^{eq} .

rescence. However, for an uptake assessment, we are also interested in the actual *quantity* and not just the relative proportion. The former is usually assessed with the help of the total fluorescence intensity within the cell. This is accepted generally as a quantitative measurement for the absolute amount of a fluorescence-labeled species [131–133], although it is rather error prone, by the fact that the intensity is sensitive to bleaching and photo physics. To overcome these limitations, we propose to limit the observation to a single shot per cell (to limit the photobleaching) and to extend the intensity based measure with the term we have just derived for the relative amount of the dye vs autofluorescence. As a result, we estimate that the uptaken quantity is proportional to

$$\begin{aligned} Q &\propto \left(1 + \frac{I - I_{\text{BG}}}{I_{\text{BG}}}\right) \times \alpha \\ &\propto \frac{I}{I_{\text{BG}}} \times \alpha \end{aligned} \quad (4.10)$$

This result extends the sensitivity range for low quantities where the fluorescence intensity is close to the intensity of the background (autofluorescence) and leads to more reliable and stable results.

4.2.2 Results and discussion

We have performed a series of experiments. Figure 4.9 shows a comparison of typical images for the three cases: (A) the beginning of the experiment, where the cells are fully loaded with labeled transferrin, (B) an image of cells after 20min, where a large amount of the uptaken labeled transferrin is recycled back into the medium and (C) a typical image of the

Chapter 4. Triplet lifetime imaging applications

autofluorescence of CHO-cells excited at 532nm. All the images have then been segmented manually in order to calculate the mean triplet lifetime over a single cell. Figure 4.10 shows a graph of the evolutions for the respective parameters. Every single spot corresponds to the intensity-weighted mean over roughly 10-20 cells. After every single observation, the field of observation has been moved to a new area on the dish in order to keep the photobleaching as low as possible to prevent falsification of the intensity based measurement. Since there is a rather large variability of uptaken transferrin from one cell to the next, the results show an important dispersion of values.

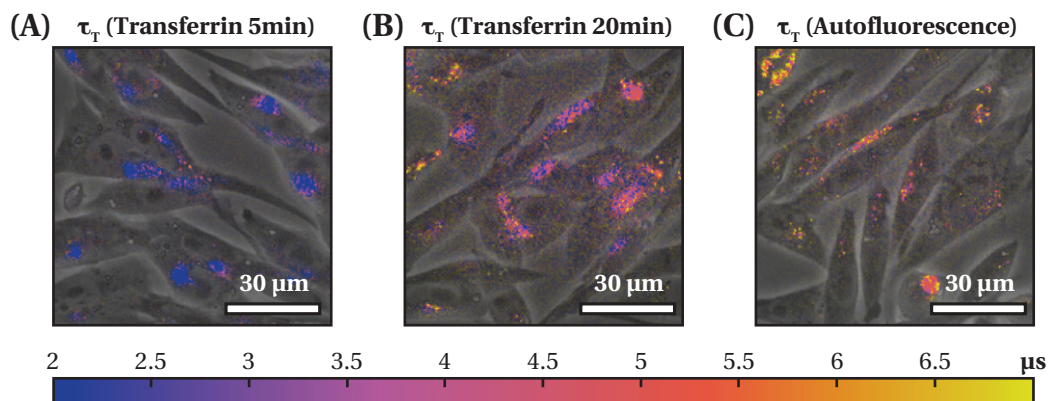


Figure 4.9: Triplet lifetime images of transferrin recycling (color encoded). (A) Beginning of the experiment, where the cells are fully loaded with labeled transferrin. (B) An image of cells after 20min, where a large amount of the uptaken labeled transferrin is recycled back into the medium and (C) a typical image of the autofluorescence of CHO-cells excited at 532nm. The calculation employs a singlet lifetime of $\tau_S = 2.4\text{ns}$ for the TMR-labeled Transferrin (from fluorescence lifetime measurements) and $\Phi_T = 0.3\%$ (from triplet-lifetime and -yield fitting over ROI inside CHO-cells).

Our results proof that the triplet lifetime based uptake assessment can provide an interesting extension to existing intensity based measures, since the lifetime is (almost) unaffected by photobleaching. Under normal uptake conditions, the fluorescence intensity of the uptaken TMR-labeled transferrin is only about twice the intensity coming from the autofluorescence inside the cell. As a result, intensity-based assessment of the evolution of the recycling of transferrin can only be done up to the half-time of the recycling. The lifetime dependent measure, extends this range and allows for studies on the transferrin recycling on a longer time-scale.

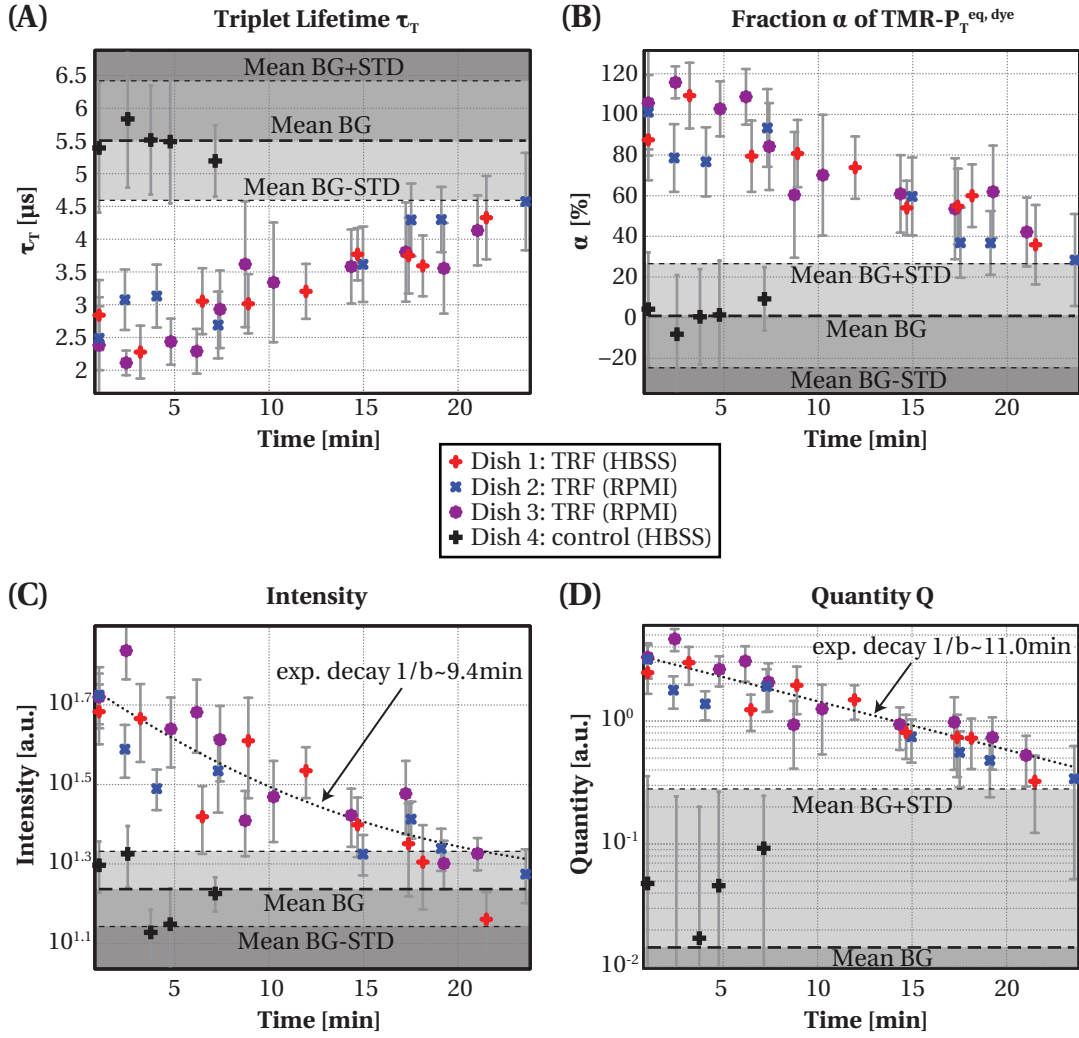


Figure 4.10: Assessment of transferrin recycling in CHO-cells for three different experiments compared to the autofluorescence within these cells. **(A)** Triplet lifetime, **(B)** proportional amount of the dye ($\alpha=100\%$) vs autofluorescence ($\alpha=0\%$) as defined by equation 4.9, **(C)** fluorescence intensity and **(D)** quantity of transferrin inside the cell Q as defined by equation 4.10. For the control measurement, we have repeated every washing and incubation step as for the experiments, except that we did not incubate the cells with transferrin-DMEM but only pure DMEM. For the quantity calculations, we used $\tau_{T, \text{dye}} = 2.5\mu\text{s}$ and $\tau_{T, \text{autofluorescence}} = 5.51\mu\text{s}$. Further on, the calculation employs a singlet lifetime of $\tau_S = 2.4\text{ns}$ for the TMR-labeled Transferrin (from fluorescence lifetime measurements) and $\Phi_T = 0.3\%$ (from triplet-lifetime and -yield fitting over ROI inside CHO-cells).

4.3 Fluorophore-DNA-complexes

The quenching of fluorescence of tetramethylrhodamine by guanosine (a DNA-base) has been shown already 15 years ago, by Edman et al. [61]. Subsequent work by the same group and others further identified and discussed different states during the quenching process [60, 134–136]. The quenching has been attributed to photoinduced electron transfer [134, 137] when the fluorophore and the base are close enough for this kind of interaction ($<1\text{nm}$). More recently the group of Zhao et al. proposed a three-state charge separation model for the TMR-guanosine interaction. With the help of fluorescence-correlation spectroscopy (FCS) they measured a distinct third state appearing upon the addition of guanosine to a solution of TMR [138, 139]. On the FCS-curves, the state "looks" very similar to a triplet state, which comes from the fact that the third state is indeed also a long-living dark-state, as is the triplet state.

However all the employed techniques that are able to measure the quenching of fluorescence by DNA are only partially extendable for imaging. We wanted to check, if this additional dark state, originating from charge-separation, can also be observed by triplet lifetime imaging.

For the case of FCS at low intensities, the three-state model from Li et al. [138] is adequate and accurate to describe the results. However in our case with a strong illumination intensity, we also have an important triplet state population. As a result, the addition of DNA, *should* in principle be described by a four-state system. However in the observed results, both states contribute to the observed dark-state population and an unmixing of the two is difficult at least. This is why we have adopted the terminology of dark-state instead of triplet state or charge-separation population. As a proof of concept, we have observed the dark state lifetime and -yield of TMR within a DNA-poly-L-lysine complex.

4.3.1 Materials and Methods

Sample

We have labeled two different Poly-Lysine analogues of different sizes with tetramethylrhodamine (TMR): a dendrimer ($\approx 2\text{ kDa}$) and a larger hyperbranched Poly-Lysine ($\approx 80\text{ kDa}$). These poly-Lysines analogues [140] are used as new synthetic delivery vectors for DNA into the cell. Both of them are positively charged. Upon addition of negatively charged DNA, they form a complex due to electrostatic interaction. We added a plasmid of pEGFP1 N1 (4000bp) to a solution with the respective polymers and observed a droplet of each on the triplet lifetime imaging setup. The result has been compared to a droplet of the pure TMR-labeled poly-Lysine analogues. We employed a concentration of $40\text{ }\mu\text{g/ml}$ of labeled poly-Lysines that have been labeled at a 1:1 ratio and a DNA concentration of 1 mg/ml .

Image processing

The resulting images have been averaged over a small area. The intensity has subsequently been fitted both for the dark-state lifetime and -yield based on the equation for the triplet state 2.7. However, when identifying the occurrences of the triplet yield in the equation, it appears that the yield never appears alone, it is always bundled with the triplet lifetime as $\Phi_T \tau_T$. As a result, fitting of the triplet yield is not very robust and there always remains a certain interdependence between the two variables (see the dotted lines in figure 4.11 (A) as visualization). To overcome this limitation but still be able to fit the results accurately by keeping both degrees of freedom, we propose to calculate the relative dark-state population at equilibrium with regards to the expected relative triplet population for the employed fluorophore (dye). This value tells us, how much the observed dark-state population at equilibrium differs from the expected triplet population for this fluorophore. Hence with the help of equation 2.6 we define

$$P_D^{\text{rel}} = \frac{P_D^{\text{eq}}}{P_T^{\text{eq, dye}}} = \frac{\Phi_D \tau_D}{\tau_{ex} + \tau_S + \Phi_D \tau_D} \frac{\tau_{ex} + \tau_S + \Phi_{T, \text{dye}} \tau_{T, \text{dye}}}{\Phi_{T, \text{dye}} \tau_{T, \text{dye}}} \quad (4.11)$$

Where τ_D and Φ_D are the respective dark-state lifetime and -yield. Figure 4.11 (B) shows results for this relative dark-state population. Where we have used typical values for TMR (see table 2.3) as a reference. These results are much more robust and emphasize the meaningful data and values.

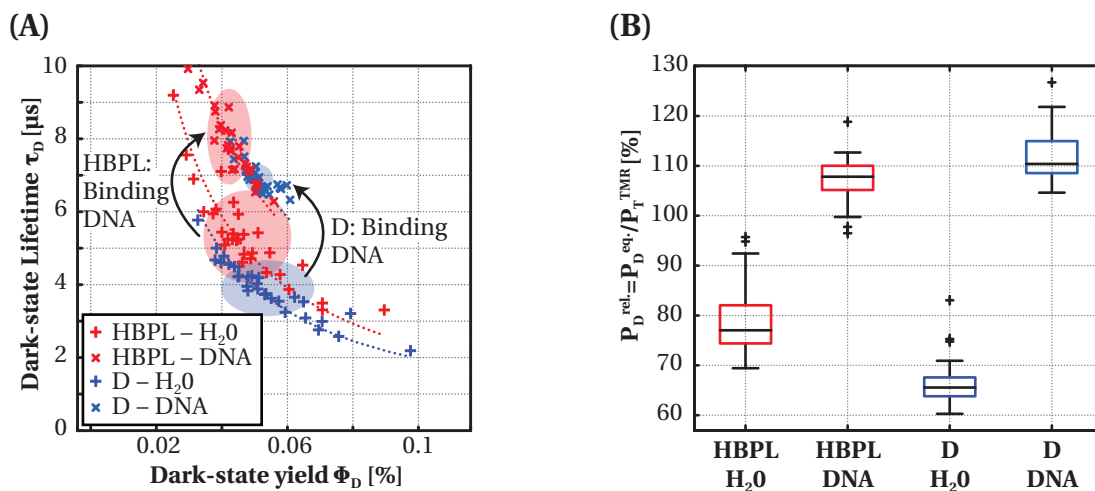


Figure 4.11: Interaction of two different TMR-labeled L-lysine analogues with DNA in solution. **HBPL** Hyperbranched Poly-Lysine ($\approx 80\text{kDa}$) and **D** Dendrimer ($\approx 2\text{kDa}$). Both of these L-lysine analogues are positively charged. Upon addition of DNA they form a complex due to electrostatic interaction. The images have been averaged over smaller region of interests (ROI). Dark-state lifetime τ_D and -yield Φ_D have then been fitted for every ROI. (A) Scatterplot of the dark-state lifetime vs -yield with ellipses indicating the mean and standard deviation values. The dotted lines are a visual guideline for the interdependence of the fitting of τ_T and Φ_T . (B) Boxplot of the relative dark-state populations as defined in equation 4.11 with the reference $P_T^{\text{eq, dye}}$ corresponding to standard values for TMR.

4.3.2 Results and discussion

Similarly to FCS measurements of the DNA-TMR interaction [138], we have observed a large increase in dark-state population upon the addition of DNA to a solution of TMR-labeled poly-lysine analogues. The interaction with the polymer, modifies the dark-state lifetime and -yield of the label compared to the triplet state of the pure dye. Because of this, the relative dark-state population without the DNA is not at 100%. Additionally our current setup is based on a wide-field approach which is suitable for imaging of cells. However for observations of droplets of solution, the lack of optical sectioning falsifies the assumed excitation profile. Nevertheless this configuration allows for a proof of concept of the contrast mechanism.

The addition of the DNA leads to a much more important dark-state population for both of the complexes that have been studied. The difference appears to be larger for the smaller poly-lysine analogue, which could potentially be due to the bigger size of the hyperbranched poly-lysine, yielding a close-interaction between guanosine and the TMR-label more difficult because the resulting complex is more bulky.

These results are a first proof of concept that triplet lifetime imaging might become an interesting imaging technique to study the presence of DNA. This opens up for studies on the interaction of DNA with the carrier during the delivery of the gene vector inside the cell.

5 Triplet SOFI - superresolution based on modulated excitation

The idea of super-resolution optical fluctuation imaging (SOFI) is to perform a higher order statistical analysis on the statistical intensity fluctuations as proposed by T. Dertinger et al. [12]. The concept can be compared to other traditional localization based super-resolution techniques such as PALM [11] and STORM [10]: the main difference to these concepts is that the later have more difficulties to cope with high-label densities than SOFI, since they "expect" single emitters for the localization. SOFI is less prone to this limitations, since even when two closely spaced fluorophores emit at the same time, there will still be uncorrelated fluctuations visible for both of them in order to distinguish them. A complete comparison between the two methods has been done by my brother, S. Geissbuehler et al. [141].

Usually any of the above mentioned methods work with fluctuations (blinking) which arise either when the fluorophores pass onto radical dark states that have lifetimes in the ms range or by specially engineered photo-activated fluorophores which allow to control the amount of emitting fluorophores by an additional activation laser. Both of these methods are necessary, to make the fluctuations accessible for the typical frame rates of CCD cameras. To enhance and control the anionic states and the related transitions employed for STORM, a wide set of chemicals and imaging buffers (containing toxic thiol compounds or other reducing and oxidizing reactants) has been developed by various groups [115, 116, 142, 143]. And for PALM, many photo-activated fluorophores have been developed and studied [144–147]. However, every fluorophore has an inherent "blinking" arising from the passage on the triplet state as can be demonstrated nicely in Fluorescence Correlation Spectroscopy (FCS) [148] as well as triplet lifetime imaging (see previous chapters). However "usually" the fluctuations are in the μs regime, which is not available with common CCD-cameras. In order to make these fluctuations available for a camera, one needs to illuminate the sample with a modulated excitation similar to the triplet lifetime imaging. Even more, the fluctuations can be enhanced by employing a pre-pulse of light illumination, which populates the triplet state prior to the acquisition. The whole concept is shown graphically in figure 5.1.

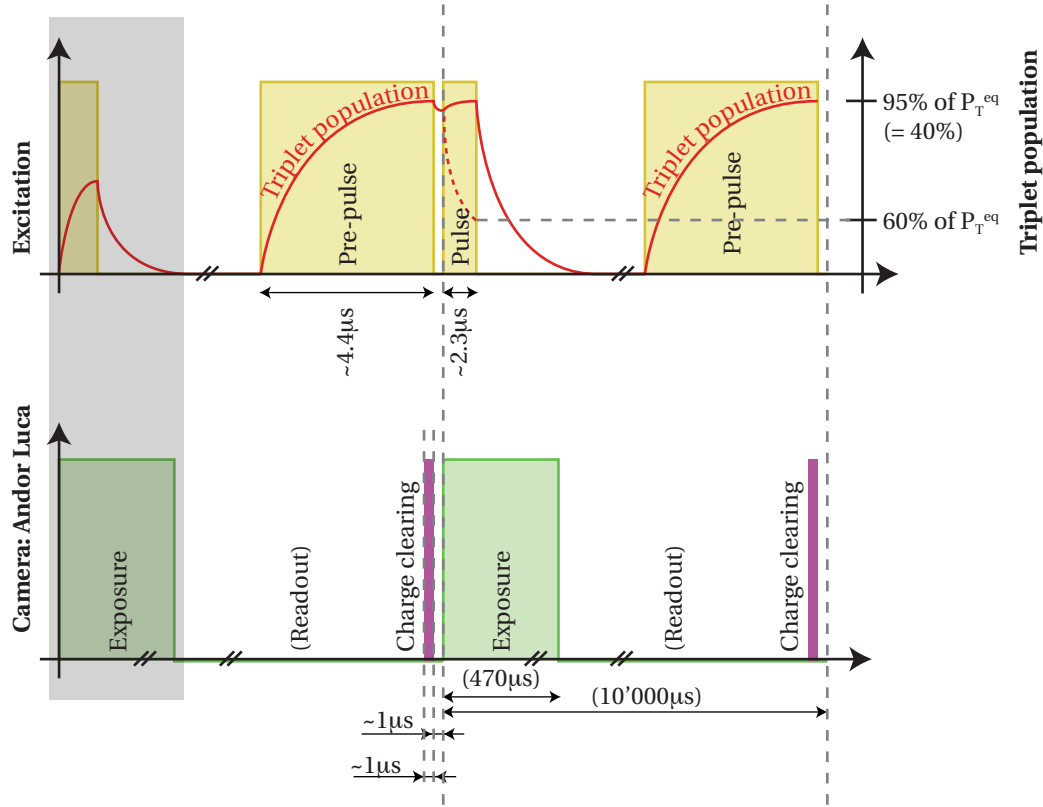


Figure 5.1: Triplet SOFI: Schematic drawing of the idea. A pre-pulse is used to populate the triplet state prior to the acquisition. A short pulse of light is used to probe the remaining molecules from the singlet state. The pre-pulse length is calculated to populate the triplet state up to 95% of the triplet state population at equilibrium P_T^{eq} for the given fluorophore and excitation power. At the beginning of the pulse, the molecules residing on the triplet state will relax back to the ground state: we want to stop the illumination when 60% relaxed from the triplet state. The concept has been optimized for the camera properties of the Andor Luca S, which has the advantage of a very fast charge clearing cycle.

5.1 Theory

The ideal length of the pre-pulse is defined by the amount of fluorophores that we want to push on the triplet state. As shown in section 2.2.1, the rise for the triplet state population can be described by an exponential increase with a rate-constant of k_2 . Hence 95% of P_T^{eq} will be reached after $t_{\text{pre-pulse}} = \log(1 - 0.95)/k_2$.

For the ideal pulse length, we focus only on the fraction of molecules that reside in the triplet state at the beginning of the pulse: they will relax back to the ground-state with the typical triplet state lifetime. Since the fluctuations will be averaged out if those presumably dark fluorophores start to emit during the measurement pulse, we want to keep the fraction that relaxed back to the ground state low and hence 60% of these initially dark molecules will relax to the ground state in $t_{\text{pulse}} = \log(1 - 0.6) \times \tau_T$.

In order to calculate the amount of photons emitted for every fluorophore that is *on* during the pulse length, we need to take into consideration their non-stationary behaviour. At the beginning of the measurement pulse, those molecules will experience a similar average singlet state population as depicted on figure 2.5 at the onset of the pulse. Correspondingly the decrease of the singlet state population follows an exponential decay with rate constant k_2 . So the amount of emitted photons per measurement pulse (eg frame) per molecule in the *on*-state can be described by

$$N^{\text{frame}} = \Phi_F \frac{1}{\tau_S} \times \int_0^{t_{\text{pulse}}} P_1^{\text{on}}(t) dt \quad (5.1)$$

Where $P_1^{\text{on}}(t)$ is the temporal evolution of the singlet state population for an excitation starting at 0. The derivation is similar as for the average fluorescence intensity given in appendix A. The calculation is done for molecules that are in the ground state at the beginning, or in other words, molecules that are not in the triplet state. With the help of equation A.10 on page 108 and $P_T(0^+) = 0$, we find as boundary condition $a_2 = -P_T^{\text{eq}}$. Hence it follows that the singlet population of the bright molecules at the onset of the pulse is described by

$$\begin{aligned} P_1^{\text{on}}(t) &= \frac{\tau_S}{\Phi_T} \left(\frac{dP_T}{dt} + \frac{1}{\tau_T} P_T \right) \\ &= \frac{\tau_S}{\Phi_T} \left(a_2 \left(k_2 + \frac{1}{\tau_T} \right) \exp(k_2 t) + \frac{1}{\tau_T} P_T^{\text{eq}} \right) \\ &= \frac{\tau_S}{\Phi_T} P_T^{\text{eq}} \left(\frac{1}{\tau_T} - \left(k_2 + \frac{1}{\tau_T} \right) \exp(k_2 t) \right) \end{aligned} \quad (5.2)$$

Insertion into equation 5.1 yields

$$\begin{aligned} N^{\text{frame}} &= \Phi_F \frac{1}{\tau_S} \times \frac{\tau_S}{\Phi_T} P_T^{\text{eq}} \int_0^{t_{\text{pulse}}} \left(\frac{1}{\tau_T} - \left(k_2 + \frac{1}{\tau_T} \right) \exp(k_2 t) \right) dt \\ &= \frac{\Phi_F}{\Phi_T} P_T^{\text{eq}} \left(\frac{t_{\text{pulse}}}{\tau_T} - \frac{1}{k_2} \left(k_2 + \frac{1}{\tau_T} \right) (\exp(k_2 t_{\text{pulse}}) - 1) \right) \\ &= \frac{\Phi_F}{\Phi_T} P_T^{\text{eq}} \left(\frac{t_{\text{pulse}}}{\tau_T} - P_T^{\text{eq}} (\exp(k_2 t_{\text{pulse}}) - 1) \right) \end{aligned} \quad (5.3)$$

where we have used the simplification from equation A.17 on page 109.

5.2 The ideal fluorophore

Similarly to section 2.4, we can now compare various fluorescent molecules according to their photophysical behaviour. The *ideal* candidate for triplet SOFI will satisfy the following requirements:

N^{frame} A crucial limitation to triplet SOFI is the very short illumination pulse, which leads to only very few photons per molecule per frame. The most important factor is hence N^{frame} , which should be as large as possible.

P_T^{eq} The technique is based on the switching of fluorescent molecules using the triplet state. The more molecules that can be pushed on the triplet state, the more the fluctuations will be important. Hence we are looking for a fluorophore with a large average triplet population P_T^{eq} . Furthermore, the P_T^{max} can be compared, to know how much larger the maximum triplet fraction would be for higher illumination intensities.

An overview of the important parameters is given in table 5.1.

5.3 Conclusion

In the case of triplet SOFI, the requirements on the fluorophore are more important than for triplet lifetime imaging. Even when using an objective with a high numerical aperture ($\text{NA}=1.45$), we can expect typically to detect only $\approx 5\%$ of the emitted photons due to the limited collection efficiency ($\approx 14\%$ according to [149]), the limited transmittance through the fluorescence filters $\approx 45\%$ [149]) and the quantum efficiency of the detector ($\approx 60\%$). According to theoretical calculations, SOFI requires 45 times less photons than for STORM [141]. Since the later requires typically around ≈ 300 photons, this means that we require typically at least ≈ 10 detected photons for SOFI. With the 5% detection efficiency, we require hence that the fluorophore emits ≈ 200 photons per frame in order to be a valid candidate for Triplet SOFI.

As visible in table 5.1, this limits the choice of appropriate candidates drastically. For usage with the 532nm laser, it leaves as candidates only the Rhodamines 6G and B. For both of them we can expect some 30% of the molecules in the off-state as predicted by P_T^{eq} .

Since the photophysical values for the triplet lifetime and -yield are sensitive to the employed measurement method (as discussed in section 2.4.1), the table serves merely as a guideline. Whether the fluorophores of choice really perform as expected, has to be tested in practice in future work. Additionally the Atto-dyes are also potentially interesting candidates that have not been included in this comparison due to lack of data for the triplet state properties.

This preliminary conceptual work, opens a door for future work on this subject, to test if the method has the potential to become an interesting super-resolution technique or not.

5.3 Conclusion

Table 5.1: The *ideal* triplet SOFI fluorophore: a comparison of relevant parameters when excited by three different lasers: Argon (488nm and 514nm), frequency doubled Nd:YAG (532nm) as well as Helium-Neon laser (543nm, 594nm and 633nm) each with a resulting sample illumination intensity of 10mW/ μm^2 which is 10 times higher than for the table 2.4 for the ideal triplet lifetime imaging fluorophore.

	τ_T [μs]	Φ_F [%]	$t_{pre-p.}$ [μs] ^a	t_{pulse} [μs] ^b	P_T^{eq} [%]	P_T^{max} [%]	% Sat.	N^{frame}
488nm								
TMR	2.5	28	6.03	2.29	19.5	56.6	34.4	47.7
Fluorescein	1.89	71	0.38	1.73	93.3	95.4	97.8	26.6
Rhodamine 6G	2.56	95	4.01	2.35	47.8	64.8	73.8	212.5
Rhodamine 123	1.89	90	2.69	1.73	52.5	65.4	80.3	161.3
Rhodamine 110	5	94	5.19	4.58	65.3	72.4	90.2	445.4
Rhodamine B	6	53	11.52	5.5	35.9	76.3	47.1	251.3
Atto 488	4	80	2.32	3.67	80.6	85.7	94	184.4
Eosine Y	0.001	22	0	0	3	34	8.7	0
Rose Bengal	0.4	5	0.15	0.37	87.9	98.3	89.4	0.2
514nm								
TMR	2.5	28	4.77	2.29	36.2	56.6	64	100.9
Fluorescein	1.89	71	0.47	1.73	91.8	95.4	96.2	26
Rhodamine 6G	2.56	95	3.33	2.35	56.6	64.8	87.4	271.3
Rhodamine 123	1.89	90	2.37	1.73	58.1	65.4	88.9	187.4
Rhodamine 110	5	94	6.28	4.58	58.1	72.4	80.2	372.3
Rhodamine B	6	53	7.93	5.5	55.9	76.3	73.2	462.1
Atto 488	4	80	2.47	3.67	79.4	85.7	92.7	180.2
Eosine Y	0.001	22	0	0	5.9	34	17.4	0
Rose Bengal	0.4	5	0.05	0.37	95.8	98.3	97.4	0.2
532nm								
TMR	2.5	28	4.43	2.29	40.8	56.6	72.1	117.9
Rhodamine 6G	2.56	95	3.06	2.35	60.1	64.8	92.8	297.3
Rhodamine 123	1.89	90	3.91	1.73	31	65.4	47.4	79.7
Rhodamine B	6	53	6.24	5.5	65.3	76.3	85.6	585.4
Atto 488	4	80	6.05	3.67	49.5	85.7	57.8	87.9
Eosine Y	0.001	22	0	0	6.9	34	20.2	0
Rose Bengal	0.4	5	0.05	0.37	95.9	98.3	97.6	0.2
633nm								
CY5	2	18	2.6	1.83	56.6	68.8	82.3	130.9

^a The pre-pulse has been calculated to reach 95% of P_T^{eq} .

^b The pulse has been calculated to stop measurements, once the available triplet state population dropped to 60% of P_T^{eq} .

Nonlinear correlation spectroscopy **Part II**

6 Nonlinear correlation spectroscopy: Theory

6.1 Non-linear optics

In classical optics, there is a linear relationship between the applied electric field $\mathbf{E}(t)$ [V/m] and the induced polarization density $\mathbf{P}(t)$ [C/m²]

$$\mathbf{P}(t) = \mathbf{P}_{\text{lin.}} = \epsilon_0 \chi^{(1)} \mathbf{E}(t) \quad (6.1)$$

where $\chi^{(1)}$ is the linear susceptibility and $\epsilon_0 = 8.85 \times 10^{-12}$ [F/m] is the permittivity of free space. This holds for low field strengths, however for higher intensities, the \mathbf{P} vs \mathbf{E} coupling becomes non-linear. The non-linearity gives rise to the fascinating higher-order nonlinear processes employed in multiple detection and imaging techniques such as coherent anti-stokes raman scattering (CARS) [33, 150, 151], second-harmonic generation (SHG) microscopy [152–154], optical coherence tomography based on SHG [155, 156] as well as third harmonic generation (THG) microscopy [157–160].

The modified non-linear relationship between the electric field $\mathbf{E}(t)$ and the polarization density $\mathbf{P}(t)$ can be written as a power-series expansion [161, 162]

$$\mathbf{P}(t) = \mathbf{P}_{\text{lin.}} + \mathbf{P}_{\text{non-lin.}} = \epsilon_0 [\chi^{(1)} \mathbf{E}(t) + \chi^{(2)} \mathbf{E}^2(t) + \chi^{(3)} \mathbf{E}^3(t) + \dots] \quad (6.2)$$

Where $\chi^{(2)}$ [m/V] and $\chi^{(3)}$ [m²/V²] are the respective second- and third-order susceptibilities. In general every material has a non-zero third-order susceptibility, however second-harmonic generation requires a non-centrosymmetric medium [161]. Furthermore the nonlinear susceptibilities $\chi^{(2,3,\dots)}$ are tensors which describe the different interaction possibilities between any of the components of the electric field and their effect on the respective polarizability components. Fortunately many of the tensor-elements are identical for symmetry reasons. For the case of a third-harmonic generation where interacting electric fields have all the

same wavelength to generate an electric field at a third of the fundamental wavelength, the non-linear susceptibility simplifies to only one independent element [161].

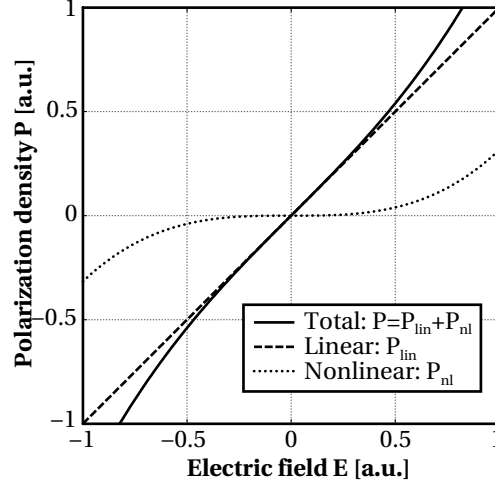


Figure 6.1: A schematic drawing of the non-linear $\mathbf{E} \rightarrow \mathbf{P}$ relation. In typical matter, there is difference between the linear susceptibility $\chi^{(1)}$ to the third order susceptibility $\chi^{(3)}$ of ≈ 24 orders of magnitude! This underlines that non-linearity requires strong electric fields.

6.1.1 Higher harmonic generation by a focussed beam

This modified relationship between \mathbf{P} and \mathbf{E} has an effect on the propagation of the optical wave through the medium of consideration: the non-linear component of the polarizability can *induce* new components of the electric field \mathbf{E} . In the following, we describe the essentials of nonlinear optics as given in detail by Boyd in his book on "Nonlinear optics" [161]. For the case of a homogenous, isotropic dielectric medium, the wave-equation can be rewritten by incorporation of a source-term as [161]:

$$\nabla^2 \mathbf{E}(\mathbf{r}, t) - \frac{n^2}{c_0^2} \frac{\partial^2 \mathbf{E}(\mathbf{r}, t)}{\partial t^2} = \frac{1}{\epsilon_0 c_0^2} \frac{\partial^2 \mathbf{P}(\mathbf{r}, t)_{\text{non-lin.}}}{\partial t^2} \quad (6.3)$$

where c_0^2 [m/s] is the speed of light in vacuum and n the refractive index of the medium. And the electric field $\mathbf{E}(t)$ and the polarization $\mathbf{P}(t)$ are represented as

$$\mathbf{E}(\mathbf{r}, t) = \mathbf{A}(\mathbf{r}) e^{i(kz - \omega t)} + \text{c.c.} \quad (6.4)$$

$$\mathbf{P}(\mathbf{r}, t) = \mathbf{p}(\mathbf{r}) e^{i(kz - \omega t)} + \text{c.c.} \quad (6.5)$$

A very common approximation of equation 6.3 is the slowly varying amplitude approximation, which assumes that the amplitude of the electric field \mathbf{E} changes in longitudinal direction only for distances larger than the optical wavelength. Additionally the laplacian operator can be decomposed in transverse and longitudinal components $\nabla^2 = \partial^2 / \partial z^2 + \nabla_T^2$. Under this

approximation, equation 6.3 can be rewritten for the harmonic generation by a gaussian beam to [161]

$$2ik_q \frac{\partial A_q}{\partial z} + \nabla_T^2 A_q = -\frac{\omega_q^2}{c^2} \chi^{(q)} A_1^q \exp(i\Delta k z) \quad (6.6)$$

Where $\Delta k = qk_1 - k_q$ which describes the wavevector mismatch between the fundamental and the higher harmonics wave and $\chi^{(q)}$ describes the q th-harmonic generation susceptibility. Under the gaussian beam approximation, A_1 and A_q , the complex amplitudes of the fundamental wave and the q th harmonic wave can be described by [161]

$$A_1(r, z) = \frac{\mathcal{A}_1}{1 + i\zeta} e^{-r^2/\omega_0^2(1+i\zeta)} \quad (6.7)$$

$$A_q(r, z) = \frac{\mathcal{A}_q(z)}{1 + i\zeta} e^{-qr^2/\omega_0^2(1+i\zeta)} \quad (6.8)$$

where $\zeta = 2z/b = 2z/(k\omega_0^2)$ with $b = 2\pi\omega_0^2/\lambda = k\omega_0^2$ the confocal parameter. It should be noted that the beam waist of the q th harmonic generation scales with the factor of \sqrt{q} with regards to the fundamental beam. However the confocal parameter b stays the same for the higher harmonic generation since $b_q = k_q\omega_q^2 = qk_1\omega_1^2/q = k\omega_0^2 = b$.

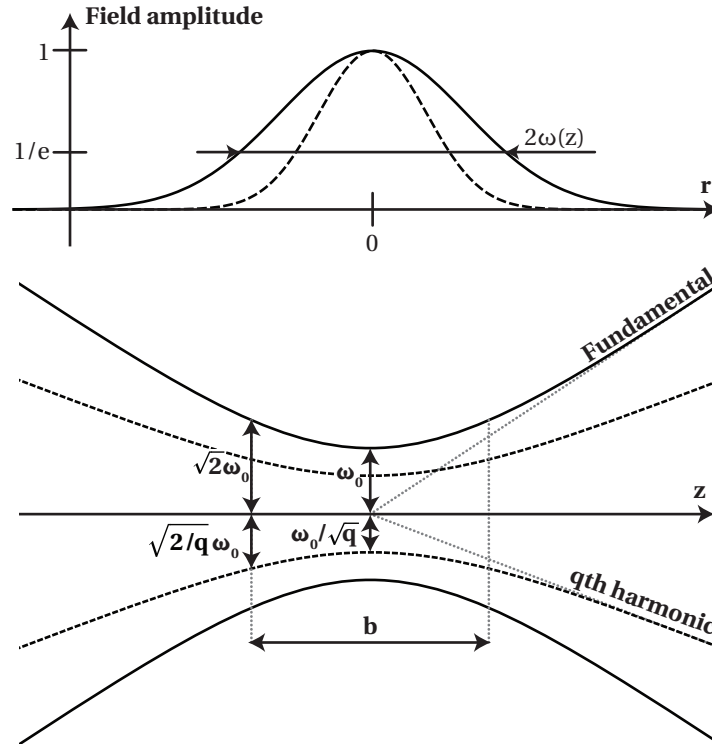


Figure 6.2: Schematic drawing of a gaussian beam. The drawing also shows the relationship between the confocal parameter b and the beam waist ω_0 . A comparison with the q th harmonic is also shown.

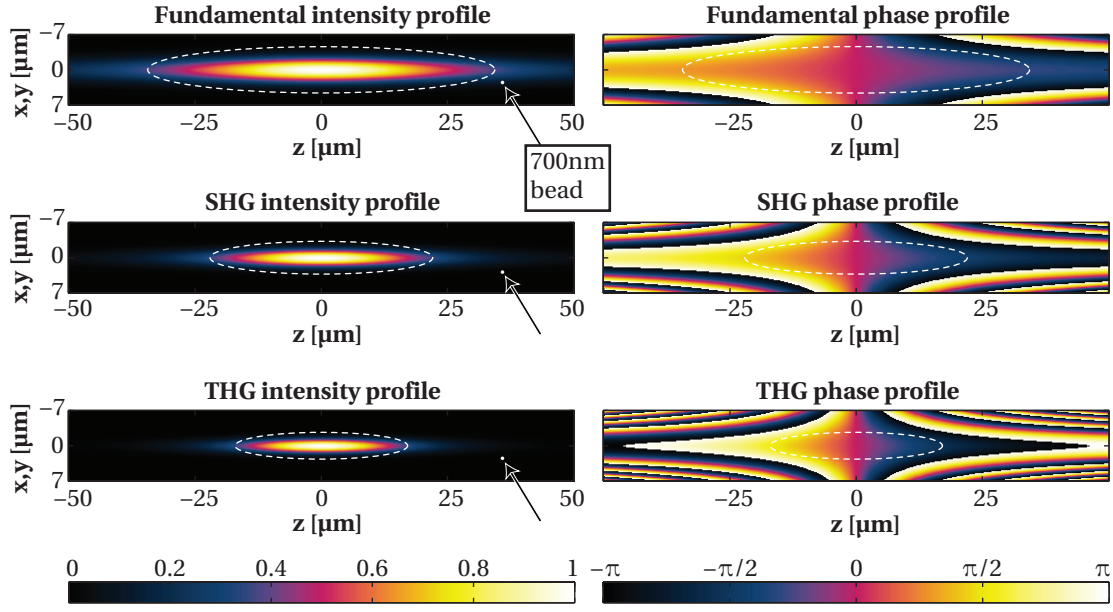


Figure 6.3: A comparison of focussed gaussian beam volumes predicted by equations 6.7 and 6.8 in intensity and phase for the fundamental beam, the second harmonic generation (SHG) as well as the third harmonic generation (THG). The calculation assumes $\lambda_{\text{fundamental}} = 1250\text{nm}$, ideal phase matching ($\Delta k = 0$) and $\omega_0 = 3.3\mu\text{m}$ which corresponds roughly to a case of $\text{NA}=0.22$ (according to our current flow cell setup depicted in Fig. 7.5). The circle indicates twice the beam waist in each direction (x,y and z) for easier comparison of the phase images.

Following Boyd [161], the complex amplitude $\mathcal{A}_q(z)$ can be found by inserting equation 6.8 into 6.6, which yields finally

$$\mathcal{A}_q(z) = \frac{iq\omega}{2n_q c} \chi^{(q)} \mathcal{A}_1^q J_q(\Delta k, z_0, z) \quad (6.9)$$

where

$$J_q(\Delta k, z_0, z) = \int_{z_0}^z \frac{e^{i\Delta k z'}}{(1 + 2iz'/b)^{q-1}} dz' \quad (6.10)$$

The integration of equation 6.10 can be done analytically for a perfect phase matching condition ($\Delta k = 0$)

$$J_q(\Delta k = 0, z_0, z, q > 2) = \frac{ib}{2(q-2)} \frac{1}{(1 + i2z'/b)^{(q-2)}} \Bigg|_{z_0}^z$$

$$J_q(\Delta k = 0, z_0, z, q = 2) = -\frac{ib}{2} \log(b) \log(1 + i2z'/b) \Bigg|_{z_0}^z$$

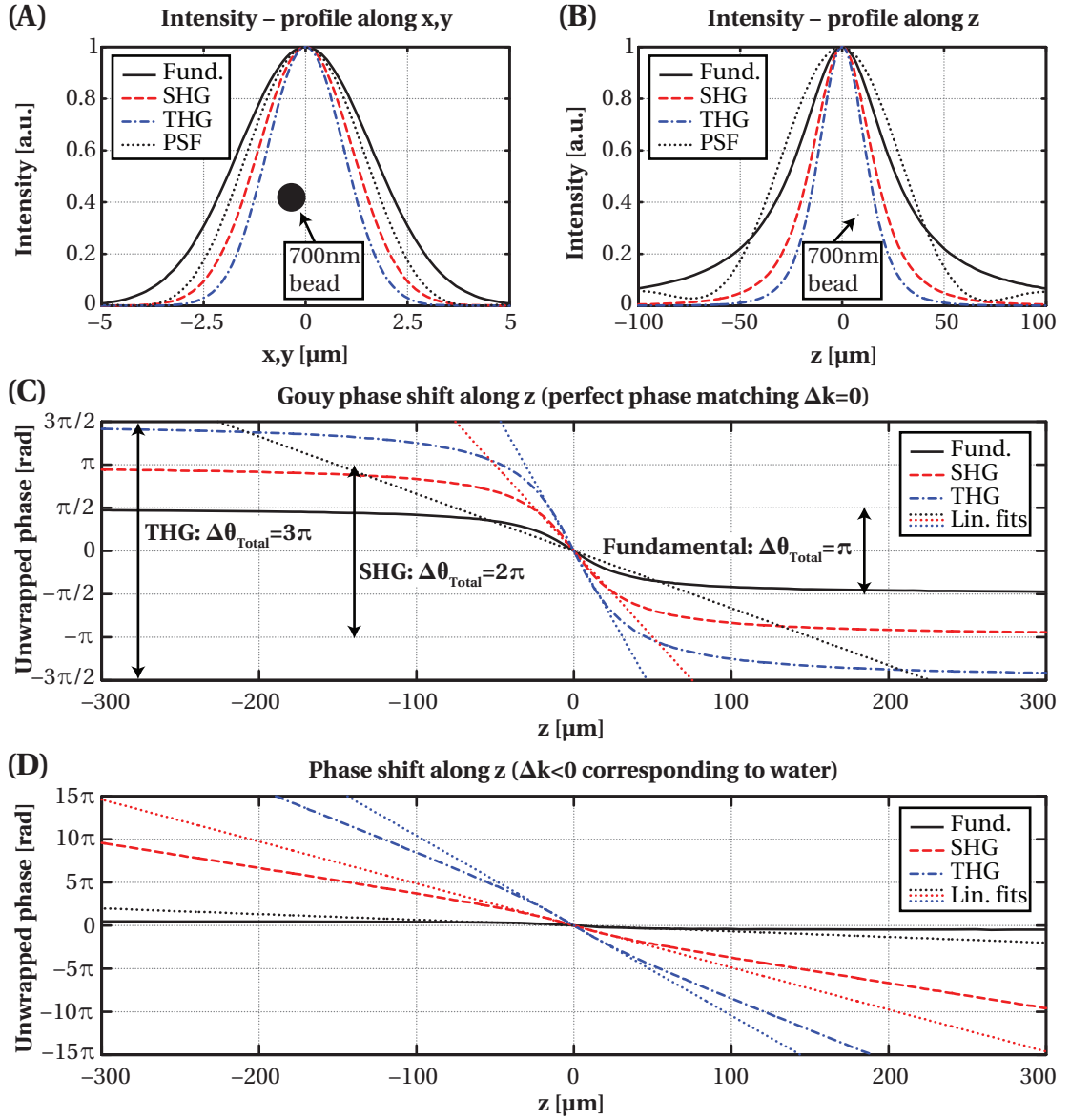


Figure 6.4: (A,B) A comparison of focussed gaussian beam volumes in lateral and axial intensity profile predicted by equations 6.7 and 6.8. PSF denotes the intensity profiles calculated by Zemax for the current flow cell setup (see figure 7.6 for further details). (C) Comparison of Gouy phase shifts for the fundamental beam as well as the second and third harmonic generation. The calculation assumes $\lambda_{\text{fundamental}} = 1250\text{nm}$, ideal phase matching ($\Delta k = 0$) and $\omega_0 = 3.3\mu\text{m}$ which corresponds roughly to a case of NA=0.22 (according to our current flow cell setup). (D) Axial phaseshift across the focal spot for phase-mismatch corresponding to water. The dotted lines depict the linear phase ramp approximation as described in section 6.2.

For third-harmonic generation in bulk material, one obtains that the generation vanishes for perfect phase matching $\Delta k = 0$ due to the Gouy phase shift: any third harmonic generation in front of the centrum of the focal spot carries a phase difference of 3π compared to the generation behind the focal spot. As a result they interfere destructively to make the signal vanish completely [161]. See figure 6.4 (C) for a comparison of the Gouy phase shifts.

6.1.2 Second and third harmonic generation by small particles

The result of the previous derivation can be translated to the case of higher harmonic generation from a single particle in focus. Shcheslavskiy et al. [163] described this for the case of third-harmonic generation. Their analysis is based on a medium and sphere contribution. Only one fundamental approximation is made: since the third-harmonic generation vanishes for the case of tight-focussing into a homogenous medium, one can write the total third-harmonic amplitude as the total third-harmonic generated by the sphere minus the total third-harmonic that would be created by the background (ex. water) in the absence of the sphere. This concept developed for third-harmonic generation can be generalized including

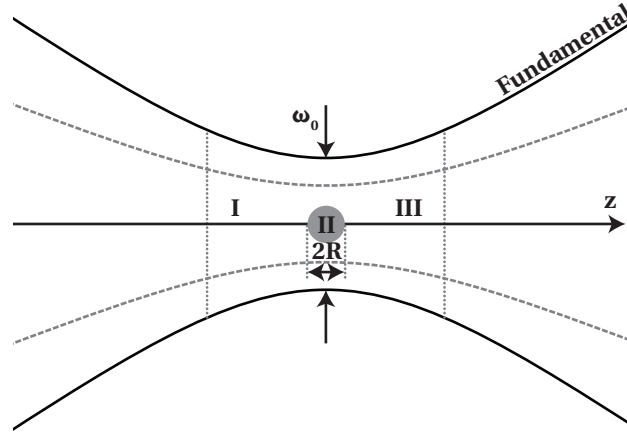


Figure 6.5: Higher harmonic generation from a single particle - Schematic principle of the decomposition proposed by Shcheslavskiy et al. [163].

second-harmonic generation, since second harmonic can only be generated from particles with a non-centrosymmetric structure¹, which is generally not the case for the surrounding medium. Therefore we generalize the concept from Shcheslavskiy et al. [163] for second and third harmonic generation. Starting from equation 6.9 we write:

$$\mathcal{A}_q(z) = \frac{iq\omega}{2n_q c} \mathcal{A}_1^q \left[\chi_I^{(q)} J_{q,I} + \chi_{II}^{(q)} J_{q,II} + \chi_{III}^{(q)} J_{q,III} \right] \quad (6.11)$$

¹The interface between two different materials is also non-centrosymmetric and can induce SHG. However in our own experiments with the interface of a centro-symmetric nanoparticle (such as polystyrene spheres) the generated second harmonic intensity was too low, to be detected in our setup.

where $J_{q,I}$, $J_{q,II}$ and $J_{q,III}$ are the integrals according to equation 6.10 over the respective areas I, II and III (see figure 6.5 for a drawing). As mentioned before, both for third and second harmonic generation, we can consider the total amplitude to be zero for tight focussing into a medium and consequently we can rewrite the last equation to

$$\mathcal{A}_q(z) = \frac{iq\omega}{2n_q c} \mathcal{A}_1^q \int_{-L(\rho)/2}^{+L(\rho)/2} \chi_S^{(q)} \frac{e^{i\Delta k_S z'}}{\left(1 + \frac{2iz'}{b}\right)^{q-1}} - \chi_M^{(q)} \frac{e^{i\Delta k_M z'}}{\left(1 + \frac{2iz'}{b}\right)^{q-1}} dz' \quad \{q = 2 \text{ or } 3\} \quad (6.12)$$

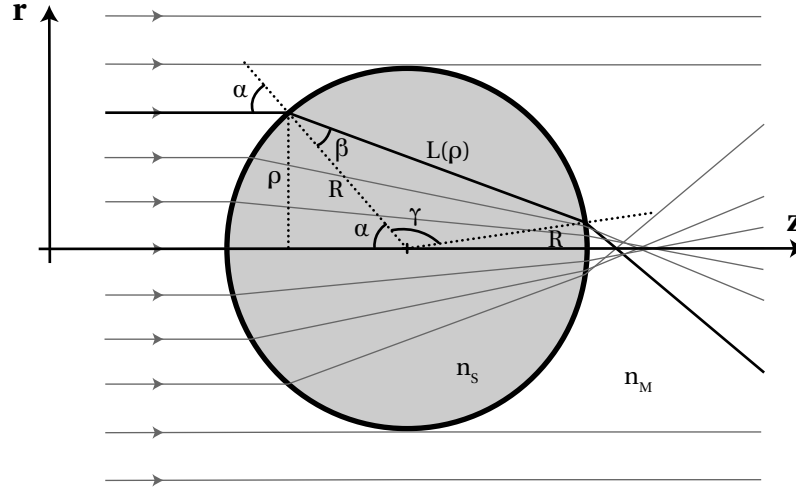


Figure 6.6: Optical interaction with a small sphere.

The limits of the integral can be approximated by geometrical optics to include the focussing effect of the sphere (see Fig. 6.6), which results in a longer optical pathlength through the nonlinear medium. The derivation employs the law of sines, Snell's law and some geometry principles:

$$\frac{L(\rho)}{\sin(\gamma)} = \frac{L(\rho)}{\sin(180 - 2\beta)} = \frac{L(\rho)}{\sin(2\beta)} = \frac{L(\rho)}{2 \sin(\beta) \cos(\beta)} = \frac{R}{\sin(\beta)}$$

and hence

$$\begin{aligned} L(\rho) &= 2R \cos(\beta) = 2R \sqrt{1 - \sin^2(\beta)} = 2R \sqrt{1 - n_M^2 \sin^2(\alpha) / n_S^2} \\ &= 2R \sqrt{1 - \frac{n_M^2}{n_S^2} \left(\frac{\rho}{R}\right)^2} \end{aligned}$$

In order to yield the total higher harmonics power emitted in the far field, we insert equation 6.12 into equation 6.8 to retrieve the full complex amplitude $A_q(r, z)$ (including the Gouy phase shift) and perform an integral over the whole volume $\mathcal{P}_q = \int I_q 2\pi r dr$ where $I_q = 2n\epsilon_0 c |A_q|^2$. Figure 6.7 shows the result of this numerical integration for different sphere sizes.

The focussed gaussian beam approximation is a rather simple model for the focal field. However the outcome of the sphere size calculation is dominated mainly by the Gouy-phase shift along the axial direction of the focussed beam, which is well described by the approximation. In order to yield most accurate results, we have chosen our gaussian beam parameter ω_0 in equation 6.7 by fitting the *entire* two-dimensional beam-profile to a point-spread-function (PSF) calculation for the respective optical systems. This is in contrast to the usual practice, where the gaussian beam parameter is simply calculated by Abbe's resolution formula $\omega_0 = 0.61\lambda_1/(\text{NA}\sin(\alpha))$ yielding the beam waist radius at the focus. Our two-dimensional parameter estimation overestimates the radial waist slightly, but yields a much better axial approximation as can be seen in figure 7.6 on page 86. The results of the higher harmonic generation intensity in function of the particle diameter can be compared to the more general approach based on Green's function formulation which can also be applied to high NA objectives (proposed by Cheng et al. [164]). In figure 6.7, both of these calculations are shown for comparison.

As a concluding remark on the higher harmonic generation theory, it should be noted that all presented approaches neglect the physical origin of the higher harmonics generation. It is simply assumed that the material can be characterized by a nonlinear susceptibility that describes entirely the generation of the higher harmonics as a function of the incident electric wave. For the case of metallic clusters, Fomichev et al. have developed a more physical model based on plasma oscillations [165, 166].

6.2 Coherent correlation spectroscopy

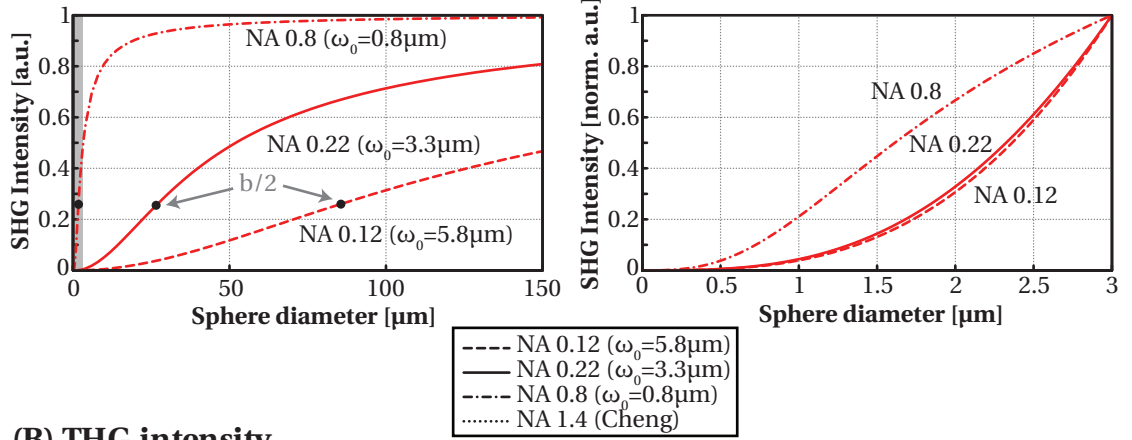
Although the approach given above is already simplified to large amounts it is not possible to obtain an analytical expression for a particle at a random position inside the focal volume. In order to develop a theory and an analytical model for the autocorrelation of diffusing particles, further simplifications have to be applied. In the past, Cheng et al. have developed a coherent correlation spectroscopy model for the case of coherent anti-Stokes Raman scattering correlation spectroscopy [70]. Their approach can be generalized to the case of higher harmonics generation from single (small) particles.

The excitation amplitude can be approximated by a gaussian focal volume taking into consideration the higher harmonic generation (eg $A_q(r)$ is the fundamental gaussian beam $A_1(r)$ multiplied q times to reflect the q th harmonic generation)

$$A_q(\mathbf{r}) \approx A_{q0} \exp\left(-\frac{x^2 + y^2}{\omega_0^2/q}\right) \exp\left(-\frac{z^2}{z_0^2/q}\right) \exp(-i\kappa_q z) \quad (6.13)$$

We have included a linear phase term κ that can incorporate for a phase mismatch ($\Delta k = qk_1 - k_q$) as well as for an eventual approximation of the Gouy phase shift across the focal

(A) SHG intensity as a function of the particle diameter



(B) THG intensity

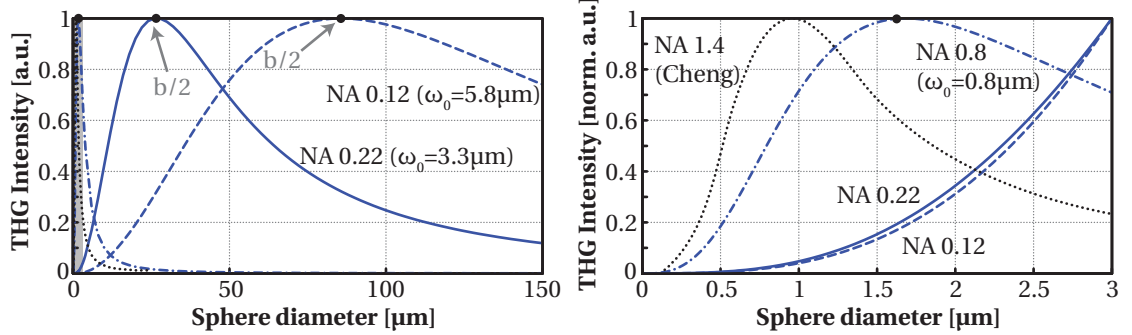


Figure 6.7: Higher harmonic generation from small particles (sphere shaped). Prediction of intensity as a function of the particle diameter for different focal volumes and comparison with the prediction from Cheng et al. [164] for a NA=1.4 case, established with the Green's function formulation. Our calculation is based on the much simpler model based on a gaussian beam approximation described in this chapter. The beam waist ω_0 estimations are based on two dimensional fitting of gaussian beam approximations as shown in figure 7.6. The NA=0.8 beam width parameters have been established by simulating in Zemax the PSF for an *ideal* (aberration free) system focussing into water. The right column is a zoom on the small particles (the curves have been re-normalized for these graphs). The black dots show half the confocal parameter $b/2 = \pi\omega_0^2/\lambda_1$, which appears to be a very accurate prediction for the diameter yielding the maximum THG intensity. All curves are calculated without phase-mismatch ($\Delta k_S = \Delta k_M = 0$). Further on, for small particles ($D \ll b/2$), it can be noticed that the particle diameter dependance of the higher harmonic generation is essentially equal for THG and SHG.

Table 6.1: Linear phase-factor κ_q for some focal volume configurations for water and an ideal dispersion-free solution. The table also gives the refractive index of water according to [167, 168]. The linear phase factors have been calculated by a linear regression weighted with the intensity of excitation intensity. See figure 6.4 for a visualization of the NA=0.22 case. For point emitters the Gouy phase shift arises only in the fundamental wave and is hence only equal to π .

	1250nm	SHG: 625nm	THG: 417nm
<i>Ideal solution without dispersion $\Delta k = 0$</i>			
κ_q (NA=0.12)	7.04×10^3	19.5×10^3	31.6×10^3
κ_q (NA=0.22)	20.1×10^3	62.6×10^3	101.4×10^3
κ_q (NA=0.8)	320.8×10^3	1027.4×10^3	1664.5×10^3
<i>Water</i>			
κ_q (NA=0.12)	7.04×10^3	110.0×10^3	257.8×10^3
κ_q (NA=0.22)	20.1×10^3	153.1×10^3	327.6×10^3
κ_q (NA=0.8)	320.8×10^3	1117.9×10^3	1890.6×10^3
<i>Point emitter case with dispersion for water</i>			
κ_q (NA=0.12)	7.04×10^3	100.2×10^3	236.7×10^3
κ_q (NA=0.22)	20.1×10^3	121.8×10^3	260.0×10^3
κ_q (NA=0.8)	320.8×10^3	604.2×10^3	781.0×10^3

volume. Hence $\kappa_q z$ is a linear approximation of the axial phase of the excitation amplitude described by

$$\Theta(z) = q \arctan(z/z_g) - (qk_1 - k_q)z \quad (6.14)$$

where for the gaussian beam approximation $z_g = b/2 = \pi\omega_0^2/\lambda_1$.

Figure 6.4 shows the linear phase approximations for our setup for two cases: a perfect phase matching as well as a typical phase-mismatch corresponding to water. For best results, the linear regression has been weighted with the intensity of the beam. Table 6.1 gives an overview of some calculated linear phase factors for further optical configurations. It is interesting to notice that the resulting terms are not very different for the case with and without phase-mismatch. This is a result of the weighted regression: for water, the predominant phase transition inside the focal volume is the Gouy phase-shift and not the linear phase-ramp induced by the phase-mismatch.

With the approximation for the excitation amplitude given in above equation 6.13, we derive an analytical expression for the normalized autocorrelation of the q th harmonic generation intensity

$$G(\tau) = \frac{\langle I_q(t+\tau)I_q(t) \rangle - \langle I_q(t) \rangle^2}{\langle I_q(t) \rangle^2} = \frac{\langle \delta I_q(t+\tau)\delta I_q(t) \rangle}{\langle I_q(t) \rangle^2} \quad (6.15)$$

where $I_q(t)$ is the q th harmonic generation intensity at time t , $\langle I_q(t) \rangle$ is the corresponding time-averaged intensity and $\delta I_q(t) = I_q(t) - \langle I_q(t) \rangle$ is the intensity fluctuation at time t .

We consider each particle as a point scatterer under brownian motion. Under these conditions we express the intensity of the scatterers by [70]

$$I_q(t) = \left| \int \chi_S^{(q)} A_q(\mathbf{r}) c(\mathbf{r}, t) dV \right|^2 \quad (6.16)$$

where $\chi_S^{(q)}$ denotes the q th-order susceptibility of the particle and $c(\mathbf{r}, t)$ denotes the concentration of particles.

The derivation of the autocorrelation theory is rather lengthy in notation, please refer to appendix B for the intermediate steps. As a result we find that the normalized autocorrelation of the higher harmonic intensity can be written as

$$G(\tau) = \frac{\langle \delta I_q(t + \tau) \delta I_q(t) \rangle}{\langle I_q(t) \rangle^2} = \frac{G_1(\tau) + G_2(\tau) + G_3(\tau) + G_4(\tau)}{G_m(\tau)} \quad (6.17)$$

Where the individual terms are given by

$$\begin{aligned} G_1(\tau) &= N \frac{\left[\exp\left(-z_{0,q}^2 \kappa_q^2\right) + \exp\left(-\frac{z_{0,q}^2 \kappa_q^2 (\tau / (S_q^2 \tau_{D,q}) + 1)}{(\tau / (S_q^2 \tau_{D,q}) + 2)}\right) \right]}{\left(\frac{\tau}{2\tau_{D,q}} + 1\right) \sqrt{\frac{\tau}{S_q^2 \tau_{D,q}} + 2}} \\ G_2(\tau) &= \frac{\left[\exp\left(-z_{0,q}^2 \kappa_q^2\right) + \exp\left(-\frac{z_{0,q}^2 \kappa_q^2 (2\tau / (S_q^2 \tau_{D,q}) + 1)}{2\tau / (S_q^2 \tau_{D,q}) + 3}\right) + 2 \exp\left(-\frac{z_{0,q}^2 \kappa_q^2 (\tau / (S_q^2 \tau_{D,q}) + 1)}{2\tau / (S_q^2 \tau_{D,q}) + 3}\right) \right]}{\left(\frac{2\tau}{\tau_{D,q}} + 3\right) \sqrt{\frac{2\tau}{S_q^2 \tau_{D,q}} + 3}} \\ G_3(\tau) &= \frac{1}{N} \frac{\left[4 \exp\left(-\frac{z_{0,q}^2 \kappa_q^2 (2\tau / (S_q^2 \tau_{D,q}) + 1)}{4(\tau / (S_q^2 \tau_{D,q}) + 1)}\right) + 2 + \exp\left(-z_{0,q}^2 \kappa_q^2\right) + \exp\left(-\frac{z_{0,q}^2 \kappa_q^2 \tau / (S_q^2 \tau_{D,q})}{\tau / (S_q^2 \tau_{D,q}) + 1}\right) \right]}{64 \left(\frac{\tau}{\tau_{D,q}} + 1\right) \sqrt{\frac{\tau}{S_q^2 \tau_{D,q}} + 1}} \\ G_4(\tau) &= \frac{\left[\exp\left(-z_{0,q}^2 \kappa_q^2\right) + 2 \exp\left(-\frac{z_{0,q}^2 \kappa_q^2 (\tau / (S_q^2 \tau_{D,q}) + 1)}{\tau / (S_q^2 \tau_{D,q}) + 2}\right) + \exp\left(-\frac{z_{0,q}^2 \kappa_q^2 \tau / (2S_q^2 \tau_{D,q})}{\tau / (2S_q^2 \tau_{D,q}) + 1}\right) \right]}{16 \left(\frac{\tau}{2\tau_{D,q}} + 1\right)^2 \left(\frac{\tau}{2S_q^2 \tau_{D,q}} + 1\right)} \\ G_m(\tau) &= \frac{1}{64} \left[\sqrt{2} \left(1 + \exp\left(-z_{0,q}^2 \kappa_q^2 / 2\right)\right) + 8N \exp\left(-z_{0,q}^2 \kappa_q^2 / 2\right) \right]^2 \end{aligned} \quad (6.18)$$

Here $\tau_{D,q} = w_{0,q}^2 / (4D)$ defines the lateral diffusion time with D in $[m^2/s]$ the diffusion coefficient, $S_q = z_{0,q} / w_{0,q}$ is a structural parameter and $N = \langle c \rangle \pi^{3/2} \omega_0^2 z_0 / q^{3/2} = \langle c \rangle \pi^{3/2} \omega_0^2 z_{0,q}$

describes the average number of molecules inside the observation volume. Further on we have used $z_{0,q} = z_0/\sqrt{q}$ and similarly $\omega_{0,q} = \omega_0/\sqrt{q}$ for more compact notation.

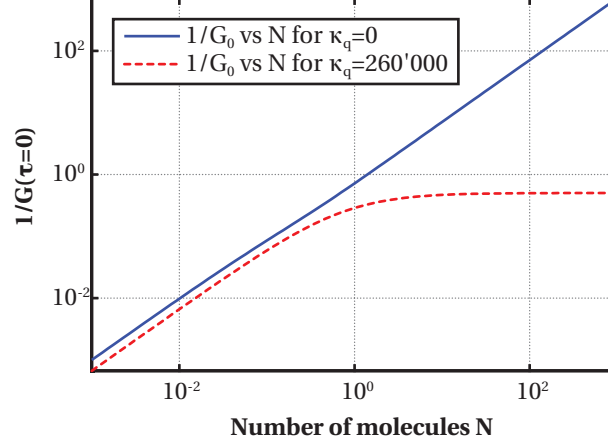


Figure 6.8: NLCS model - plot of the relationship between $1/G(\tau=0)$ and the number of molecules N inside the focal volume for the case without linear phase-factor $\kappa_q = 0$ and the case with a linear phase-factor $\kappa_q = 260.0 \times 10^3$ corresponding to THG emission from point source emitters in water with an objective with NA=0.22. The focal volume is estimated by $\omega_0 = 2.7\mu\text{m}$ and $z_0 = 53.5\mu\text{m}$ (see Fig. 7.6).

The derivation yielded a model for the non-linear correlation spectroscopy autocorrelation that is significantly more complex than the model for fluorescence correlation spectroscopy (FCS). As demonstrated by figure 6.9, all the resulting terms $G_1(\tau)$ to $G_4(\tau)$ play an important role for certain values of N and κ_q . As a result we propose to keep this complicated model as a base for the fitting. It should be noted that keeping all the four terms does not result in a more complicated fitting model in terms of the parameters to be fitted: as in FCS we only need to fit the number of molecules N and the diffusion time $\tau_{D,q}$ while the other parameters can be assumed known by calculations of the point-spread function.

It is noteworthy that for the nonlinear-correlation spectroscopy with a linear phase-factor corresponding typically to THG with an objective with NA=0.22, the autocorrelation becomes independent of N for larger number of molecules inside the observation volume as demonstrated in figure 6.8. The effect stems from the coherent interaction between the particles. This suggests that the technique is potentially applicable in fundamentally higher concentrations than FCS, since the resulting correlation amplitude will not drop to 0 for large N as in FCS.

6.2.1 Coherent correlation spectroscopy with flow components

In our experiments, we found that the strong laser power acts as an optical force that pushes the particles through the focus by radiation pressure. As a result it is required to extend

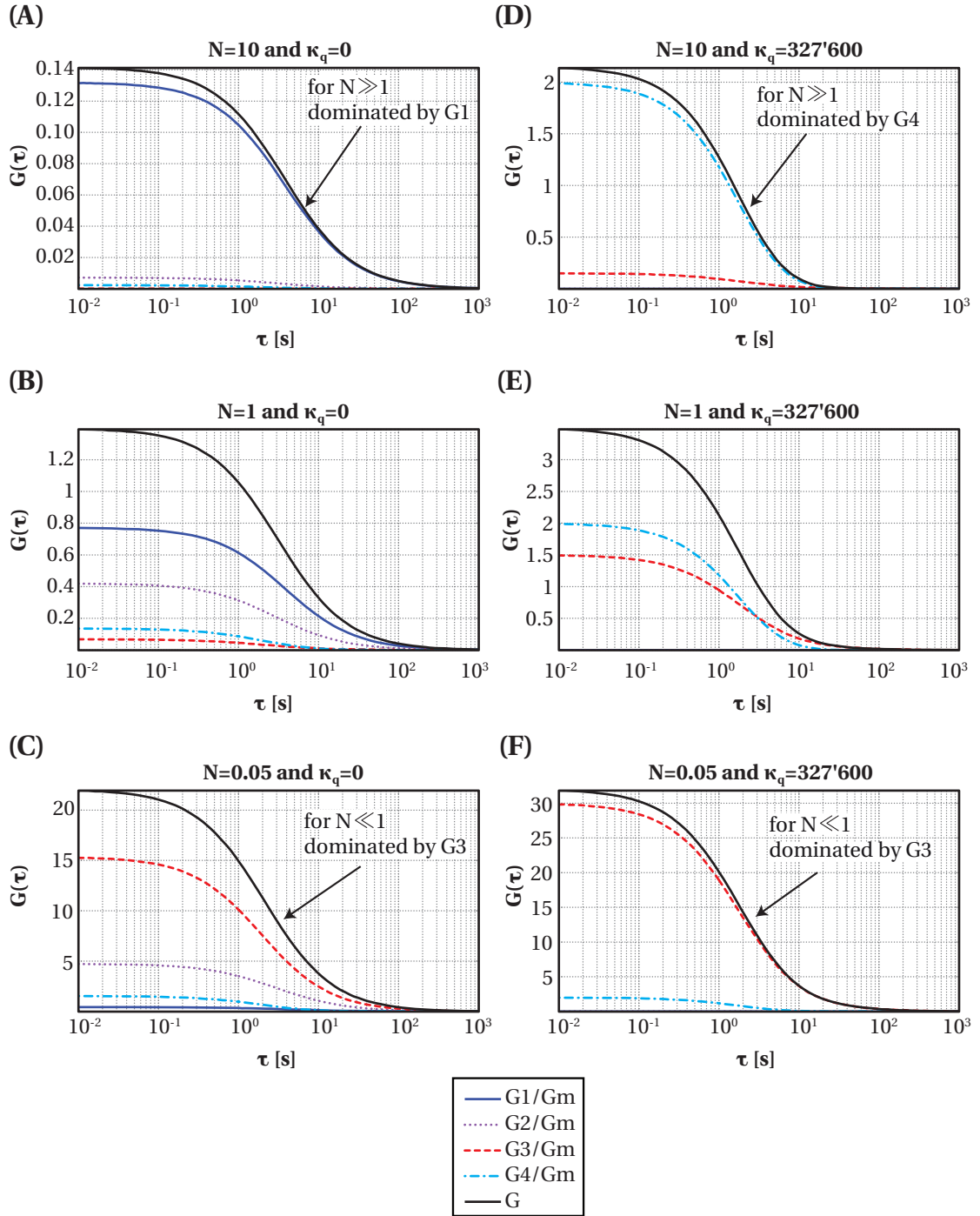


Figure 6.9: NLCS model - a plot of the various G -terms defined in equation 6.18 at different concentrations ($\propto N$) and in (A-C) for a linear phase-factor $\kappa_q = 0$ and in (D-E) $\kappa_q = 327.6 \times 10^3$ corresponding to the case of third-harmonic generation in water with an objective of $NA=0.22$ (see table 6.1). The correlation spectroscopy simulation has been done for PS-beads with a diameter of 700nm. As visible on this comparison, although for certain cases, some of the four G -terms are dominating the resulting sum, all of them are important in a certain range of N and κ_q -values. The focal volume is estimated by $\omega_0 = 2.7\mu\text{m}$ and $z_0 = 53.5\mu\text{m}$ (see Fig. 7.6).

the autocorrelation model with flow components. The full derivation is further detailed in appendix B. As a result we find that all the four terms we have derived for the case without flow, are modified. As a particularity of the coherent model, we find cosine terms in the resulting correlation functions (see equation B.30 as an example) which stem from our linear phase factor that we have added to the model. For the case of an axial flow these terms lead to oscillations of the autocorrelation curve as seen in Fig. 6.10.

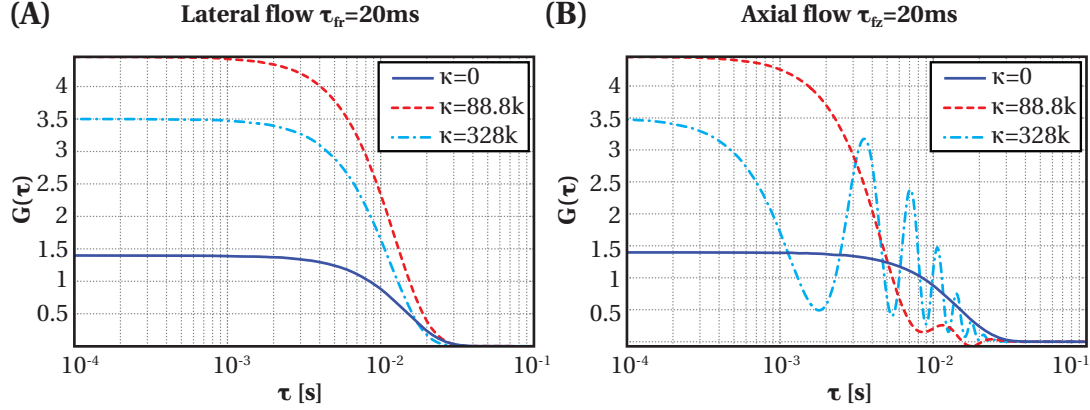


Figure 6.10: NLCS model with flow components. Autocorrelations for lateral and axial flows for different linear phase factors κ . The graph predicts that the axial flow leads to oscillatory behavior of the autocorrelation (depending on the phase factor). We used $N = 1$, $q=3$ for THG and diffusion properties for 700nm PS-spheres in water.

6.2.2 Estimation of flow velocities due to optical forces

The effect of radiation pressure induced acceleration of particles has been studied more than 40 years ago by A. Ashkin [169]. The model that he proposed for the acceleration of particles is based on the transfer of momentum from a photon to an object upon reflection on its surface. The radiation force along the optical axis (or scattering force) that is exerted on a particle can be described by [170, 171]

$$\mathbf{F}_{\text{radiation}} = \frac{\sigma n_m}{c} \langle \mathbf{S} \rangle \quad (6.19)$$

where σ is the scattering cross-section, n_m is the refractive index of the medium, c the speed of light and $\langle \mathbf{S} \rangle$ is the time-averaged Poynting vector. The scattering cross-section is given by [171]

$$\sigma = \frac{8}{3} \pi k^4 \left(\frac{m^2 - 1}{m^2 + 2} \right)^2 r^6 \quad (6.20)$$

Where $k = n_m 2\pi/\lambda$ is the wavenumber, $m = n_p/n_m$ the ratio of the refractive index of the particle and medium and r is the radius of the particle.

The maximum velocity that the particle can obtain is limited by the Stokes law for the drag force [172]

$$F_{\text{drag}} = -6\pi\eta r v \quad (6.21)$$

where η is the dynamic viscosity, r the radius of the particle and v the velocity of the particle. The maximum velocity is found when the drag force is equal to the radiation force, hence we find

$$v_{\text{max}} = \frac{4k^4 n_m r^5 \langle S \rangle (n_m^2 - n_p^2)^2}{9c\eta (2n_m^2 + n_p^2)^2} = \frac{4k^4 n_m r^5 P (n_m^2 - n_p^2)^2}{9c\eta \omega_0^2 \pi (2n_m^2 + n_p^2)^2} \quad (6.22)$$

Where P is the laser power and ω_0 is the beam-waist. With the help of the above formula, we calculate that a 700 nm polystyrene (PS) sphere would be accelerated to a velocity of $v_{\text{max}} \approx 3.0$ m/s if illuminated with a laser power of 240 mW focussed to a beam-waist of $\omega_0 = 2.7 \mu\text{m}$ (NA=0.22). This corresponds to a transition time through the focus of $\tau_{fz} = z_0/v_z \approx 18.1 \mu\text{s}$ for $z_0 = 53.5 \mu\text{m}$. Similarly for the case with the lower NA-objective (NA=0.12) we predict $v_{\text{max}} \approx 0.9$ m/s and $\tau_{fz} \approx 180.3 \mu\text{s}$. We have neglected the gradient forces in this approximation [171]. For the case of high NA objectives, the later can lead to a trapping of the particles.

For the case of focussing into a solution of freely diffusing particles, v_{max} can be used as an upper boundary for the expected mean velocity. However it is more reasonable to assume that only few particles are being accelerated to the full speed during their passage through the focal volume. The observed correlation curve will thus rather be defined by a $v_{\text{mean}} = \zeta v_{\text{max}}$. Calculation of $\zeta < 1$ is beyond the scope of this thesis. It should take into account a model for the force-field and the Brownian motion of the particles.

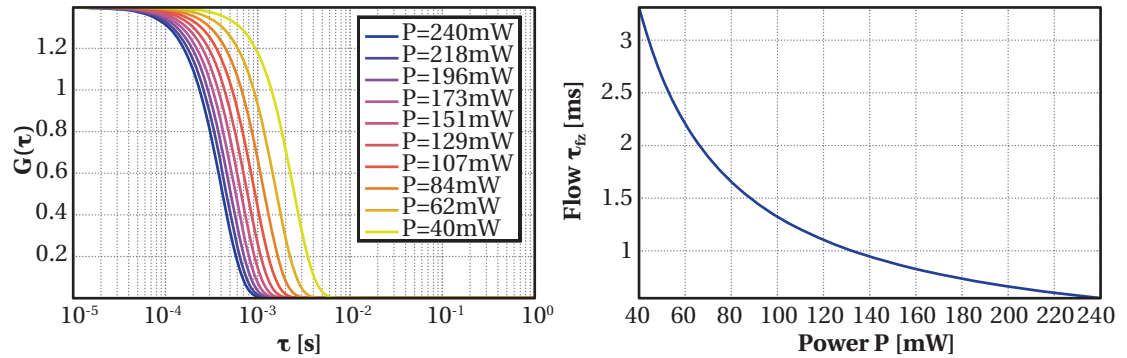


Figure 6.11: Plot of the power dependency of the NLCS model with radiation pressure induced flow. The calculation assumes a linear phase-factor $\kappa_q = 0$ with an objective with NA=0.22. The focal volume is estimated by $\omega_0 = 2.7 \mu\text{m}$ and $z_0 = 53.5 \mu\text{m}$ (see Fig. 7.6). The calculation assumes that all particles are accelerated immediately to a velocity v_{max} .

7 Nonlinear correlation spectroscopy (NLCS) - Setup and Experiments

7.1 Mode-locked Cr:forsterite laser

Our investigations for non-linear correlation spectroscopy rely on a customized Cr:forsterite laser originally conceived by V. Shcheslavskiy. The gain medium is a Chromium-activated Forsterite single crystal, $\text{Mg}_2\text{SiO}_4:\text{Cr}^{4+}$ or in short Cr:F. This crystal has a very broad fluorescence band between 680 to 1400nm [173].

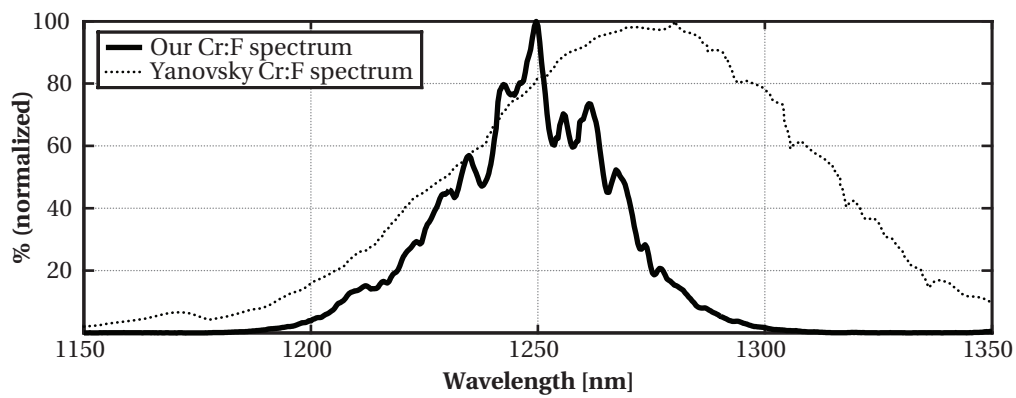


Figure 7.1: Spectrum of the Cr:F laser output in mode-locked mode in comparison to the spectrum of the Cr:F laser built by Yanovsky et al. [174]

Our customized laser system consists of a 15mm Cr:F crystal in a long resonator designed for high peak powers at a repetition rate of ≈ 25.4 MHz. Figure 7.2 shows a drawing of the cavity design. The laser is pumped by a Ytterbium fiber laser (YLD-10-1064-LP, IPG Laser GmbH) at 1064nm with 9W output. Table 7.1 gives an overview of all the components. The crystal is held in a "sandwich" structure between two Peltier cooling elements for precise temperature control necessary for stable resonator condition and to minimize the thermal lensing within

the gain element. For best laser-output stability the crystal is purged by a continuous (but weak) flow of nitrogen, which is cooled and stabilized in temperature by the water circuitry. The laser cavity contains a prism pair for the group velocity dispersion (GVD) control.

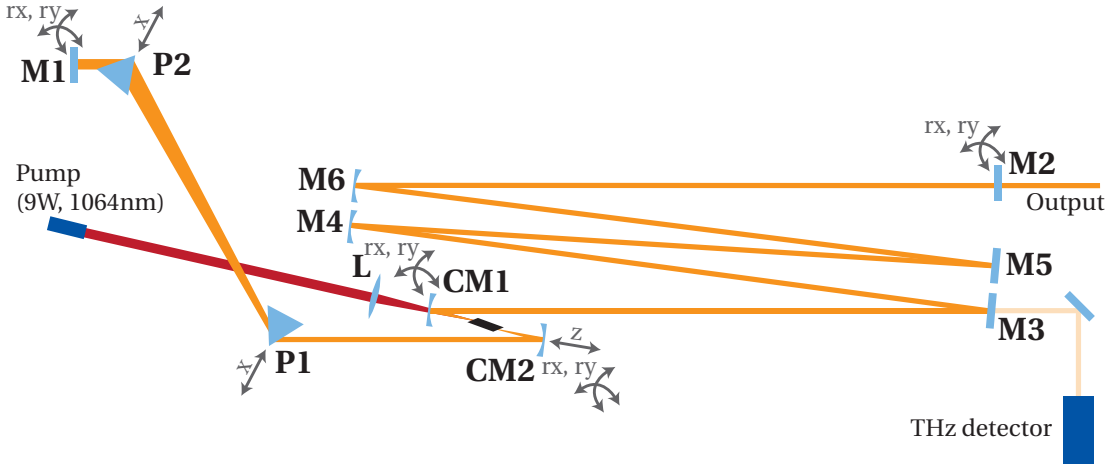


Figure 7.2: Schematic drawing of the Cr:forsterite laser cavity. The details of each element are given in table 7.1 and the output characteristics are given in table 7.2.

A Terahertz detector (125 MHz bandwidth, TIA-500, Terahertz Technologies Inc.) allows to measure the intracavity pulses by monitoring the small leakage behind a dichroic mirror. This allows to monitor the mode-locking without disturbing the laser action and without the need of the full laser output.

The pulse duration is in the femtosecond regime, in order to characterize the pulse duration, one has to rely on a measurement based on an autocorrelation of the pulse [175]. We have employed an interferometric autocorrelator (FEMTOLASERS Produktions GmbH with modifications - see Fig. 7.4 for a drawing). Figure 7.3 shows a typical measurement of the laser pulse duration. Further we characterized the spectrum using a fiber based spectrometer (Ando AQ-6315B) to measure the spectrum of the laser output (see figure 7.1). The beam diameter

Table 7.1: Cr:F laser components (purchased from Optics-M, Moscow, Russia)

Item	Description
Crystal	Cr:forsterite (15mm length)
CM1, CM2	Curved dichroic broadband mirrors (radius of curvature 150mm, R@1250>99.8%, T@1067>92%)
M1, M3, M5	Dichroic broadband mirror (R@1250>99.8%)
M4, M6	Spherical curved mirror (radius of curvature 2000mm)
M2	Output coupler (8.5%)
P1, P2	Brewster cut prisms (SF 14)
Pump	Ytterbium fiber laser (YLD-10-1064-LP, IPG Laser GmbH)
L	Pump lens (f=150mm)

7.2 Nonlinear correlation spectroscopy setup

Table 7.2: Typical values of the Cr:F laser characteristics. The values correspond to pump-power of 9W at 1064nm with the Cr:F crystal regulated at a temperature of 3°C.

	Value	Figure
Cr:F laser output		
Central wavelength λ_0	1249.0nm	7.1
Bandwith $\Delta\lambda$	36.1nm	7.1
Output power	241mW	
Pulse duration	56.3fs	7.3
Pulse repetition rate	25.39MHz	
Peak power	148.3kW	
Beam waist	2mm	

has been characterized by a scanning slit beam profiler (BP104-IR, Thorlabs Inc.). Table 7.2 gives an overview of all the characteristic parameters for the Cr:F laser.

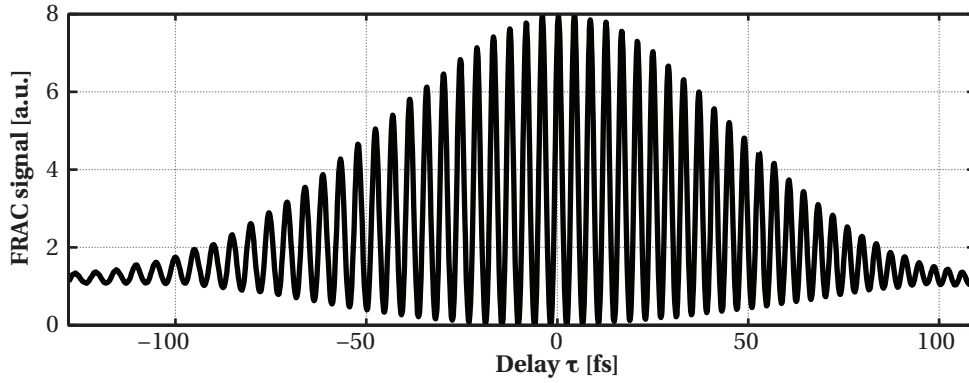


Figure 7.3: Fringe-resolved autocorrelation (FRAC) of the Cr:F laser pulse as measured by the auto-correlator shown in figure 7.4. The shown graph corresponds to an average of twenty measurements for better SNR. The pulse duration can be estimated by counting the number of fringes N above the 50% line. The pulse duration is then given by $N\Delta\tau/B$ where $B=1.897$ for sech^2 pulse shapes and the fringe spacing can be estimated by $\Delta\tau = \lambda_0/c$ [176]. This yields 56.3 fs for this FRAC-trace. The system is bandwidth-limited ($\Delta\tau=45.4$ fs for sech^2 pulses with our given spectrum).

7.2 Nonlinear correlation spectroscopy setup

We have based the setup for correlation spectroscopy analysis on a flowcell made out of quartz (Suprasil), providing very low background contributions and a broadband transmission between 200-2500nm (137-QS 1mm, Hellma GmbH & Co. KG). The focussing of the fundamental laser beam and the collection have been done with aspheric lenses ($f=4.51$ mm and $f=8$ mm). Figure 7.5 shows an overview of the setup with all components.

The aspheric lenses have been designed for observing a sample through a coverslide with a thickness of 170 μm . In order to be sure that the performance is still within acceptable range,

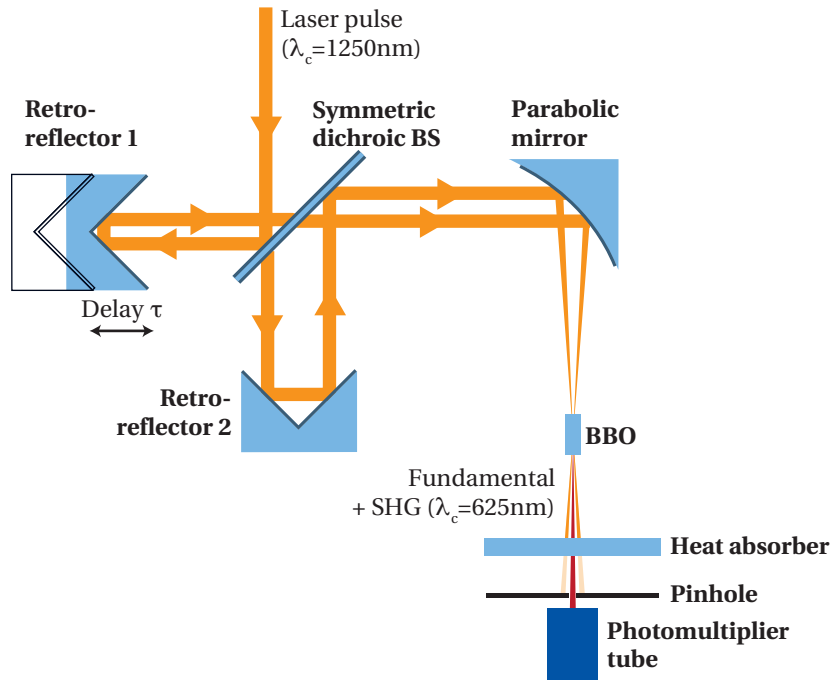


Figure 7.4: Interferometric autocorrelator for pulse length characterizations. The device employs a symmetric dichroic beamsplitter instead of the conventional Michelson interferometer design to improve the symmetry of the splitting of the pulses [177]. The optical parts have been manufactured and assembled by Femtolasers, Austria (Femtometer). We employ a BBO crystal (0.5mm thickness, type-II, Castech) for second harmonic generation. The addition of the heat-absorbing glass yields highly improved background rejection yielding more sensitive measurements. The delay τ is adjusted by a piezo actuator (3043, PX 100, Piezosystem Jena) driven by a piezo driver (MDT-694, Thorlabs Inc.) connected to a function generator (triangular waveform with frequency of 3Hz). The signal output from the photomultiplier tube is low-pass filtered by analog electronics and displayed by a digital oscilloscope (TDS 220, Tektronix) connected to computer for digital acquisition. Figure 7.3 shows a typical autocorrelation trace measured with this device.

we have performed a calculation of the point-spread-function (PSF) of the system through the 1mm flowcell-wall-thickness in an optical design program (Zemax). The result is shown in figure 7.6. The results of this simulation have also been used for the theoretical analysis in the previous section 6.

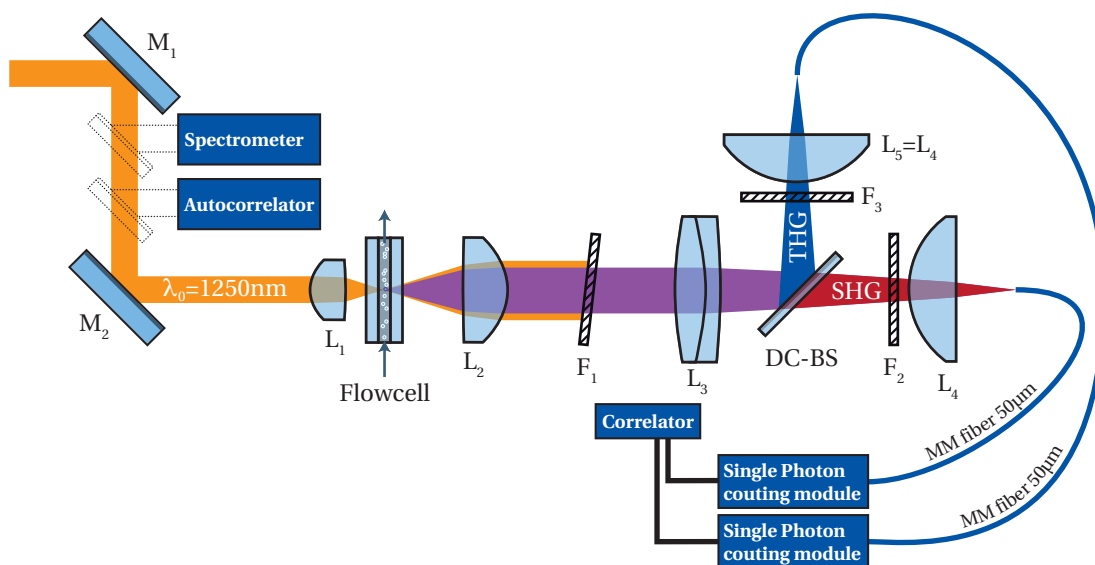
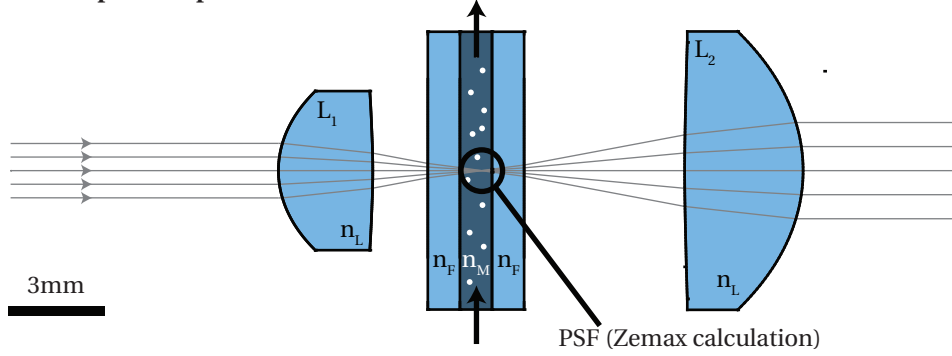
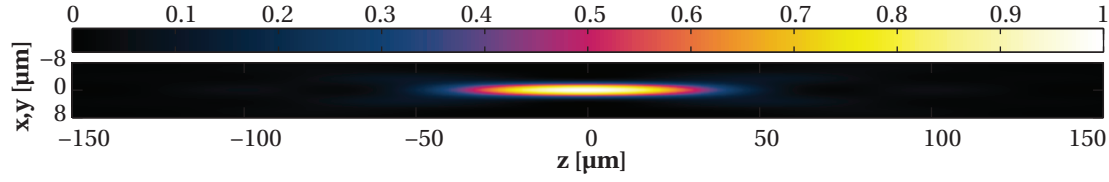


Figure 7.5: Nonlinear correlation spectroscopy setup. The setup consists of two aspheric lenses L_1 , L_2 (See Fig. 7.6 for details), a **flowcell** (137-QS 1mm, Hellma), a tube lens system L_3 , L_4 , L_5 (effective focal length of $f=80\text{mm}$ by combination of a NIR-achromatic lens $f_{L3}=160\text{mm}$ and a singlet lens for each channel with $f_{L4,L5}=30\text{mm}$), a heat absorber F_1 , a dichroic beamsplitter **DC-BS** (500dcxr, Chroma Inc.), a filter for SHG-emission F_2 (HQ630/60m-2P, Chroma Inc.), a THG-filter F_3 (HQ450sp-2P, Chroma Inc.), two **multimode fibers** (AFS50/125Y, Thorlabs Inc.), two fiber-coupled **single photon counting modules** (SPCM-AQR-14-FC, PerkinElmer) and a hardware **correlator** (Flex02-12D/C, Correlator.com). M_1 , M_2 are broadband gold mirrors for beam alignment.

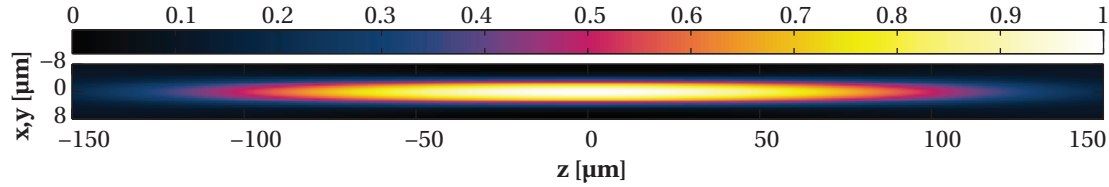
(A) Flow cell setup with aspheric lenses



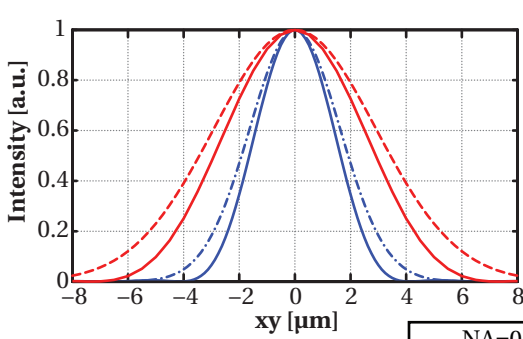
(B) NA=0.22 – Zemax PSF calculation



(C) NA=0.12 (L_2 swapped with L_1) – Zemax PSF calculation



(D) Intensity profile along xy



(E) Intensity profile along z

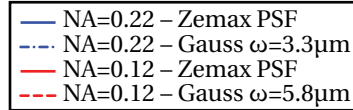
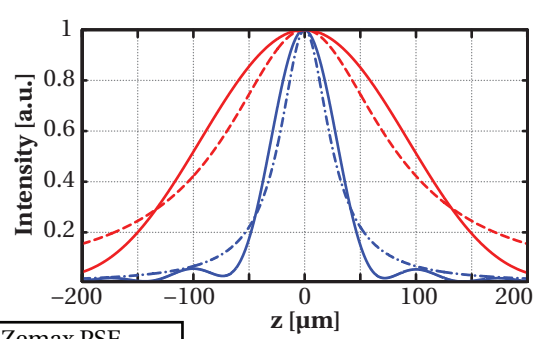


Figure 7.6: (A) A drawing of the flow cell setup with the focussing lens L_1 ($f=4.51\text{mm}$, $\text{NA}=0.55$, Glass=Corning C0550, #350230, Thorlabs Inc.) and collection lens L_2 ($f=8\text{mm}$, $\text{NA}=0.5$, Glass=Corning C0550, #350240, Thorlabs Inc.). The flow cell is made of 2 glass covers (Suprasil) of 1mm thickness and a flow chamber of 1mm thickness. (B) Calculation of the point-spread-function (PSF) as predicted by Zemax (Huygens PSF calculation) for gaussian input beam with 2mm waist. (C) An alternative setup configuration with lenses L_1 and L_2 being swapped. Calculation of the PSF with Zemax. (D, E) Intensity profiles along xy and z for both cases. The Profiles are overlaid by the profile of a *two*-dimensional fit of a gaussian beam. Notice the difference to the fitted gaussian beam, which is due to the fundamentally different aspect ratios between xy and z for the gaussian beam approximation and the simulation. The gaussian beam parameters has been used for the higher harmonic generation predictions in figure 6.4. When fitting the profiles for the $\text{NA}=0.22$ case only by *one*-dimensional gaussian fits, one finds $\omega_0 = 2.7\mu\text{m}$ and $z_0 = 53.5\mu\text{m}$ and for $\text{NA}=0.12$ one finds $\omega_0 = 4.8\mu\text{m}$ and $z_0 = 168.6\mu\text{m}$.

7.3 Nonlinear correlation spectroscopy (NLCS) results

7.3.1 Materials

For the measurements, we used aqueous solutions of polystyrene spheres (Polysciences Inc.) of different sizes (109nm, 202nm, 356nm, 771nm, 992nm, 2061nm and 2834nm with 10% size accuracy according to the manufacturer) at various dilutions. The solutions have been shaken, sonicated and flown through the observation flow-cell for several minutes prior to the measurement to ensure good mixing of the slightly precipitating suspensions. After each measurement, the flow cell has been first rinsed by 50ml of water, then 10ml of ethanol, followed by thorough rinsing with water for 20min (with approximately 200ml). Introduction of the new solution has only been done, once the photon trace of the water showed no remaining particles in a 1min observation window. However, even this thorough procedure was not able to remove all particles from the tubing and flow system. In addition we hence implemented a software based artifact removal as detailed below.

For the measurements with KNbO_3 , we have used nanoparticles prepared by mechanical grinding, followed by selected centrifugation and deposition (FEE - Forschungsinstitut für mineralische und metallische Werkstoffe Edelsteine/Edelmetalle GmbH, Dr. D. Rytz). The particles have then been prepared with a micelle-layer for protection and aggregation hinderance. They have been prepared by C. Kasparian from GAP-Biophotonics Geneva from a solution of DSPE-PEG, chloroforme and KNbO_3 -particles by selectively evaporating the chloroform to produce a film of DSPE-PEG+particles that forms micelles upon resuspension in ultrapure water.

The flow setup was driven by a peristaltic pump (Reglo Digital, Ismatec). For measurements with lateral flow, we regulated the later at a speed of 1 ml/min.

7.3.2 NLCS artifact removal

We were using a flow-cell setup for our measurements. This allowed a convenient exchange of solutions and observations in a cell with very low background contributions. However it has the disadvantage that the tubings cannot be replaced after every measurement. In practice even after thorough rinsing with water and ethanol for 20min there were still some spurious particles (or aggregates) from previous measurements inside the flow system. In correlation spectroscopy techniques (such as FCS or NLCS), these bright aggregates can cause important distortions of the resulting autocorrelation curve even for a single and rapid passage through the focal volume. To overcome this limitation we have implemented a selective piecewise post-acquisition correlation algorithm published by Ries et al. [178]. The algorithm removes pieces of the photon-trace that yield to aberrated correlation curves. Which significantly improves the accuracy of the measurement in a semi-automatic way. Figure shows an example of two

typical autocorrelation curves: an artifact-free curve where the post-acquisition correlation fits perfectly to the autocorrelation from the hardware correlator and a curve with an important sample artifact, where the post-acquisition correlation differs significantly from the hardware autocorrelation.

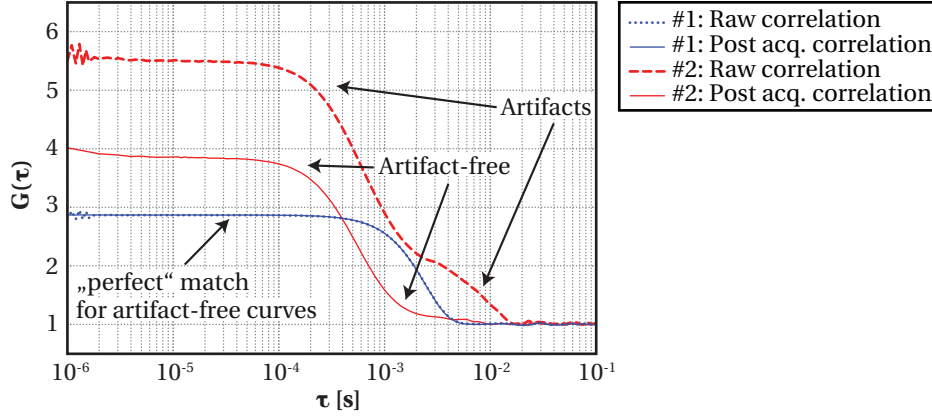


Figure 7.7: NLCS measurement artifact removal by selective piecewise post-acquisition correlation as published by Ries et al. [178]. In measurement 1, the 60s photon trace has been subdivided in 30 parts, where all of them have been used. For measurement 2, we used only 22 of the 30 parts to remove the artifacts.

7.3.3 Polystyrene spheres diffusion

Figure 7.8 shows the main result from these measurements. We have varied the laser power with a neutral density filter and looked at the diffusion of Polystyrene spheres of 700nm. As predicted by Ashkin, we have observed a significant power dependency for the flow velocity which stems from the radiation pressure induced acceleration. As already mentioned in the theory part (Section 6.2.2) the measured velocities were slightly below the predicted v_{\max} . Nevertheless the result follows rather closely the predictions given in figure 6.11. The optical forces are weak and hence when adding a lateral flow to the measurement, the power dependency for the diffusion time, disappears almost entirely. This is a nice indirect proof of the nature of the effect. It is further interesting, to notice that the number of molecules inside the volume varies with the laser power as well. The volume increases with increasing laser power, and hence the number of molecules as well. A plot of N vs the incident power is shown in figure 7.9 (B). The same graph also shows nicely the third-power dependency of the emitted third harmonic generation light. All the curves have been fitted with $\kappa = 0$. In fact this parameter, although interesting, has to be chosen very carefully because it leads to a highly unstable fitting. As visible in figure 6.10 on page 78, values of κ close to 100k, lead to a modification of the apparant diffusion constant as perceived by eye (and the fit), as a result, slight modifications in κ will induce large modifications of the diffusion constant and the fitting becomes unstable.

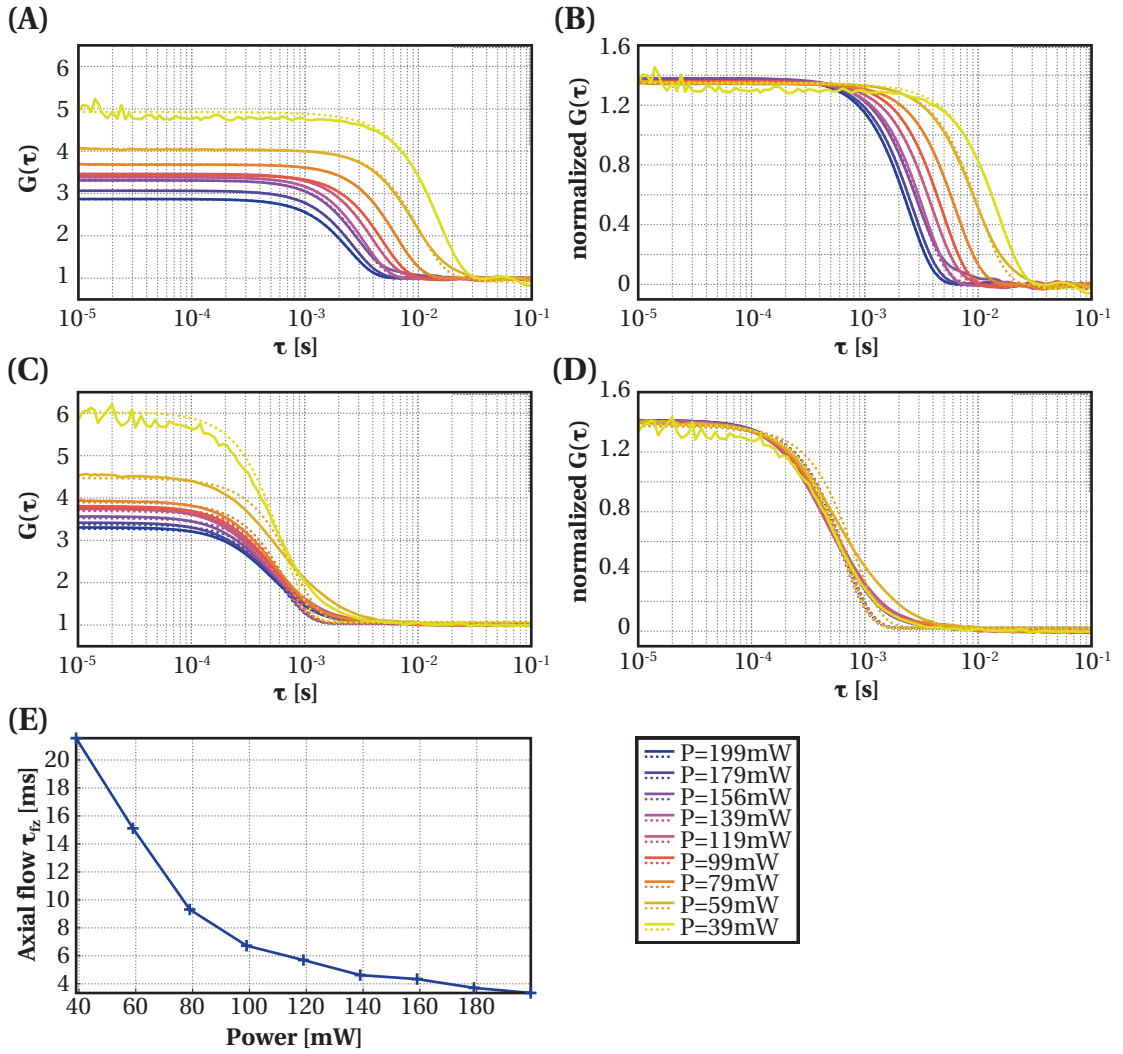


Figure 7.8: NLCS measurement of the radiation pressure effect in function of the incident power for 700nm PS spheres in water. **(A-B)** Measurement of the "free" diffusion (solid lines) and fit by NLCS model with flow (dotted lines). The radiation pressure effect is clearly visible, similar to the model predictions in figure 6.11. The fitted axial flow values have been plotted in **(E)**. **(C-D)** When adding a small lateral flow (1ml/min) by the peristaltic pump, the weak optical forces are no longer dominating, and the radiation pressure dependency disappears. For all fitting of the curves we fixed $\kappa = 0$. The curves in (A) and (C) have been plotted with a background correction.

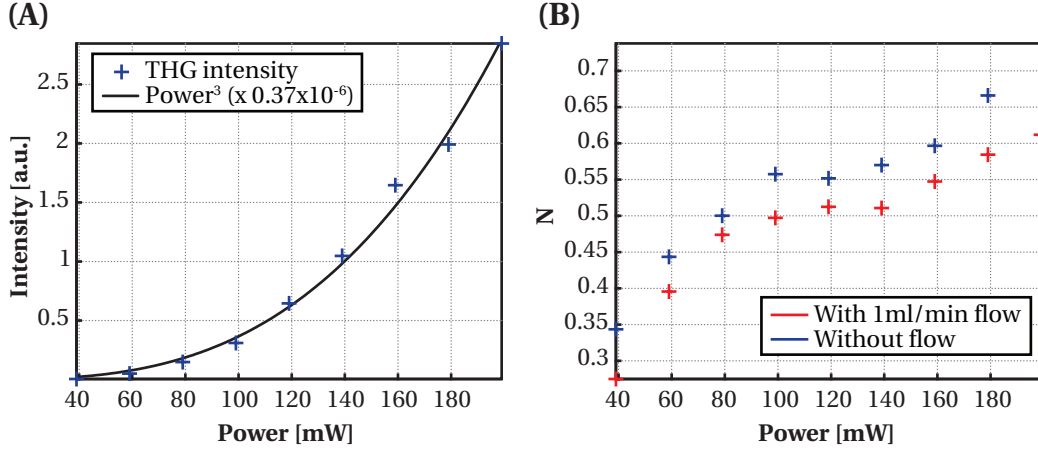


Figure 7.9: NLCS measurement of 700nm PS spheres: (A) power dependency of the emitted third harmonic generation with a third-power dependency fit (black line) and (B) number of molecules inside the focal volume. The values for N have been corrected by the background intensity by $N = N_{\text{fit}} \times \left(1 - \frac{I_{\text{BG}}}{I}\right)^{-2}$.

For future work it would be interesting to investigate further into this issue. In particular in figure 7.8 (B), some oscillations are visible for the yellow (low intensity) curves, which clearly indicate the validity of our flow model with the additional cosine-terms. Further on, it is interesting that the curve with added lateral flow (Fig. 7.8 (D)) has a significant "hump" at its bottom which the fit fails to take into consideration. This might be another indication for a phase factor.

In a second experiment we have modified the size of the polystyrene beads. The resulting curves are shown in figure 7.10. As visible on the graphs, all sizes $< 1 \mu\text{m}$ diameter are strongly affected by a flow component leading to a fast decay of the correlation curve. The spheres with the largest diameter of $2 \mu\text{m}$ and $2.8 \mu\text{m}$ however, show a slower decay, indicating that the brownian motion induced diffusion speed of these spheres "starts" to play a role. Very interesting is also the dependency of the third-harmonic power as a function of the sphere diameter (Fig. 7.10 B). The result of this measurement has been predicted in the previous chapter on Figure 6.7 on page 73. Multiplying the calculated model with a constant scaling factor, leads to a very good agreement between the measurements and the theoretical prediction. The good agreement is even more visible when plotting the result with a logarithmic scaling (Fig. 7.10 C)

7.3.4 KNbO₃-nanoparticle diffusion observed in SHG and THG

In a final experiment, we have looked at NLCS curves for KNbO₃-nanoparticles. These particles are based on a non-centrosymmetric non-linear crystal and can generate second harmonic

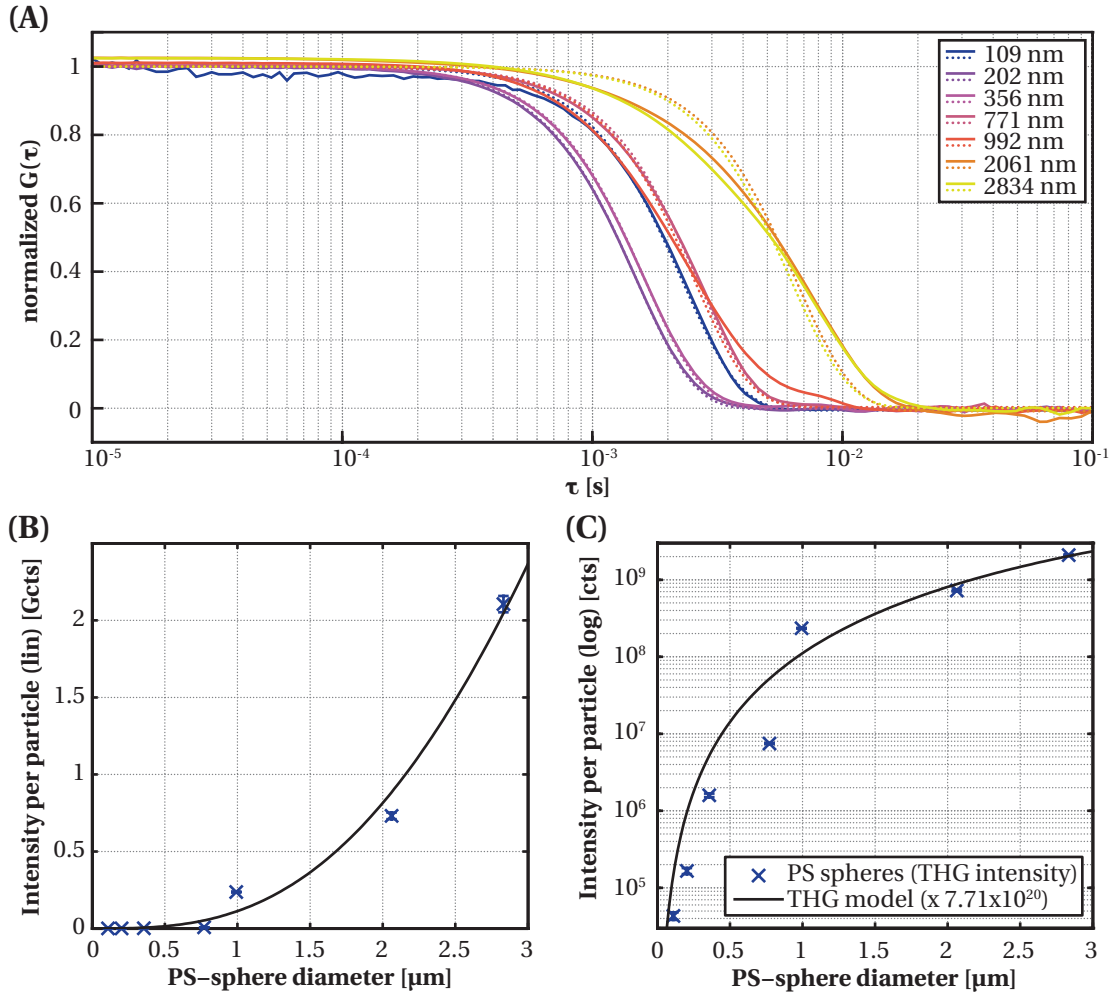


Figure 7.10: (A) NLCS curves for polystyrene (PS) spheres with different diameters. Fit: τ_{fit} =3.34, 2.39, 2.67, 4.38, 10.18 and 9.48 ms. (B-C) THG intensity vs sphere diameter with an overlay of the scaled THG-intensity model for NA=0.22 discussed in Fig. 6.7. To avoid detector saturation, a neutral density filter was added for big sphere diameters (992nm and 2061nm with ND 2.0 and 2834nm with ND 3.0).

light upon illumination with short laser pulses. Figure 7.11 shows NLCS-curves for these particles. In addition we have found that these particles generate a strong THG-signal. The interesting thing about this combined emission is the fact that it allows to characterize the focal volume dependancy on the harmonic order. As predicted by theory, the focal volume where third-harmonic generation can appear, is smaller than for the corresponding SHG. This is visible on the NLCS-curves in two ways: first of all the amount of molecules in the focus are very different ($N_{\text{SHG}} = 187.6 \times 10^{-3}$ and $N_{\text{THG}} = 8.5 \times 10^{-3}$) and secondly the diffusion times are different. For the case of SHG, the curve shows a similar "hump" as the observations we have made with PS with lateral flow. The effect could presumably also stem from the linear phase factor, since it is expected to be very different for SHG and THG. However since in a first step, we have fixed $\kappa = 0$, an accurate fitting was impossible and the fitting algorithm, used

$\tau_{D,q}$ to take care of the differences. As a result the values for the diffusion are not comparable otherwise than by visual inspection of the graph.

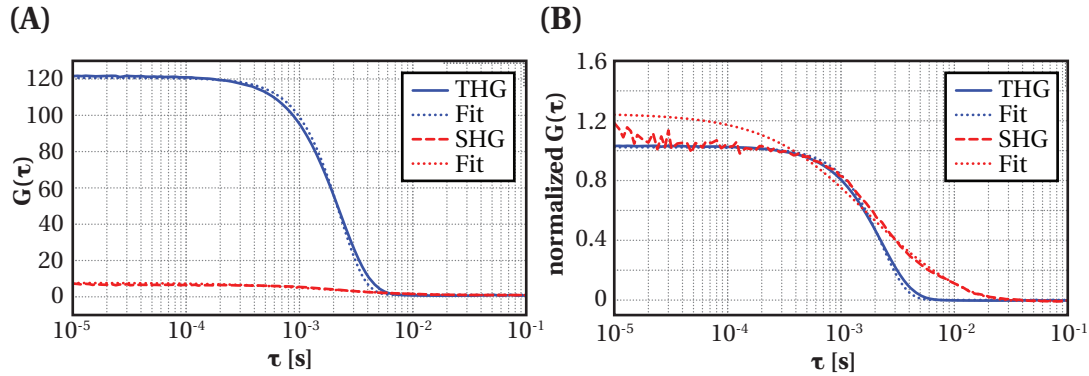


Figure 7.11: NLCS of KNbO_3 -particle diffusion in SHG and THG

7.3.5 Conclusion

NLCS has been successfully applied to some preliminary systems providing first results and showing some of the particularities of the method in comparison to other spectroscopy correlation techniques such as FCS and CARS-CS.

These preliminary results open the door for further investigations based on the theoretical framework and the available measuring platform. As future perspectives, it would be interesting to look into sensing in complex environments (such as blood serum) and whether the combined THG and SHG from the KNbO_3 -nanoparticles can be used as an interesting reporter for diffusion related studies in these environments in a test tube as well as *in vivo*.

Afterword **Part III**

8 Conclusion and Outlook

This thesis aimed to develop and apply a novel concept for functional high resolution microscopy, named *triplet lifetime imaging* and in a second part to develop *nonlinear correlation spectroscopy (NLCS)*, a novel concept for spectroscopy based on the non-linear optical interaction of a femto-second laser pulse with nanoparticles.

8.1 Triplet Lifetime Imaging

In a first part, the theoretical foundations of the method have been done, including a simple analytical model, describing the fluorescence emission under a modulated excitation. The theory has then been used to discuss from a theoretical point of view, the requirements for an ideal fluorophore for this imaging modality.

After discussing the triplet lifetime imaging setup, further details on the processing have been outlined. Imaging in the context of biology leads to massive amounts of data especially for functional imaging where temporal evolutions are assessed with many hundred images per measurement session. An efficient processing platform of these images is an important requirement in order to be able to draw conclusions from the experiments and rapidly test and apply novel processing algorithms. A major part of the work of this thesis has been spent for the development of a versatile Matlab application that allows the processing and display of images with batch processing capability. The platform also allows the creation of automatical image based masks as well as rapid user drawn masking that allow subsequently a selective averaging of the data of interest. This platform has been extensively used for the uptake assessment imaging. Not only the processing of the images for the fitting has been proved, advances for an appropriate image display of the triplet lifetime data have also been made.

We have outlined a concept for functional wide-field microscopy which is able to image the triplet kinetics of fluorescent probes. Using a rapidly modulated excitation and a slow camera,

spatio-temporal variations of the triplet state kinetics of many standard fluorophores can be assessed.

Firstly, we validated our concept on thin TMR films deposited on microscope cover slips. An oxygen depletion experiment resulted in a proportional decrease of the measured triplet relaxation rate $k_T (= 1/\tau_T)$ as predicted by the well known Stern-Volmer equation. Secondly, measurements of the oxygen consumption of single smooth muscle cells A7r5 showed a mono-exponential decay of the intracellular oxygen concentration upon stimulated contraction. The decay started without measurable delay and had a characteristic decay time of 40 s, which is in good agreement with measured oxygen consumption in skeletal muscle fibers reported by Hogan et al. [128].

In our opinion, the proposed triplet state imaging concept is a valid tool for investigating the inter- and intracellular oxygen concentration variations in live cells or small tissue fragments. It is particularly attractive because it is able to image the metabolism of live cells with a time resolution in the order of a second at a state-of-the-art spatial resolution and field of view.

Further on, the technique has been applied successfully in two entirely different contexts: imaging of the cellular uptake mechanism as well as the sensing of DNA. For the first, the triplet lifetime yielded interesting additional information on the cellular processes and metabolism that is otherwise inaccessible.

The work of this thesis opened this new field of imaging for application from a theoretical and practical point of view for biological systems. Furthermore, the theoretical work allowed the emergence of a novel idea for super-resolution microscopy, named triplet SOFI. This concept opens an entirely new field for future developments and has been submitted for a european patent application.

8.2 Nonlinear correlation spectroscopy

In a second part of this thesis, a novel concept for spectroscopy has been developed. In a first step, the theory for the generation of higher harmonics from small nanoparticles has been outlined. The work extended previous work on higher harmonic generation intensity as a function of the object diameter and allowed the accurate predictions of the size-dependance for third as well as second harmonic generation with a simple model. The theory has then been extended by the development of the coherent autocorrelation function for a system with an arbitrary phase-factor definition and with additional flow components. The theoretical predictions from this model, demonstrate in particular that nonlinear correlation spectroscopy is highly interesting for its ability to yield correlation amplitudes even under very strong sample concentrations.

However a potential drawback of the technique has been identified. Since the nonlinear interaction requires high laser intensities in order to yield a higher harmonic signal, there is noticeable radiation pressure acting on the particles under observation. As a result, the particles are *pushed* in axial direction through the focus at a much higher speed than their natural brownian motion. The effect disappears efficiently, when applying a lateral flow to the observed solution. The optical forces are weak, and hence the applied lateral flow predominates the measurement.

In subsequent work, we have observed nonlinear particles based on non-centrosymmetric materials. These particles showed both a strong second as well as third harmonic generation intensity when passing through the focal volume allowing the practical determination of the different dimensions of the generation volumes as predicted also by theory.

As a conclusion, this preliminary work on nonlinear correlation spectroscopy, opens a door for future research on sensing and novel imaging concepts.

9 Acknowledgements

This whole thesis would not have been possible without the help of the many persons that I was fortunate to meet and interact with during my thesis at the Laboratoire d'Optique Biomédicale (LOB). I would like to thank them since not only I met inspiring collaborators, but I also made good friends during this time.

First of all I would like to thank Prof. Theo Lasser for accepting me in his lab and for the trust he had and continues to have in me and my research. I am very grateful for the freedom he was giving me for my research. His way of dealing with work and his lab members, creates a very positive atmosphere in the team and pushes the research of his lab in a positively challenging and stimulating way. I would like to thank him for the countless discussions and his scientific and personal support.

I had the pleasure to share my office for three years with Iwan Märki. I am very grateful for our scientific discussions, for his advice, his patience and his imperturbable character which made it a particular pleasure to collaborate with him.

I would also like to thank Marcel Leutenegger for all the fruitful discussions we had together. Every discussion brought the projects a step further and I would like to thank him for sharing his vast knowledge about optics&programming. In particular I would also like to thank him for the great time we had during our explorations by car of the US West shore after the BIOS conference in 2009.

A particular thank goes to my brother, Stefan Geissbühler. For me, it is a particular pleasure to be able to collaborate scientifically with a member of my family. I would like to thank him for his collaboration both on the Triplet SOFI and the nonlinear-correlation spectroscopy project and for his sound and reliable way of working.

I am very grateful to Noelia Bocchio. Her help in sample preparation was highly appreciated and improved dramatically the scientific quality of this work. We also had many fruitful scientific discussions together where I appreciated her scientific and rigorous way of thinking. But I would like to thank her particularly for her availability and the good mood she brought to the lab.

Chapter 9. Acknowledgements

I would like to thank Claudio Dellagiacoma for the collaborations we did together on the Triplet SOFI and the many interesting discussions. But in particular it was a pleasure to do the teaching of the Biomicroscopy lecture together with him.

Many thanks to Vladislav Shcheslavskiy for his highly valuable support during the nonlinear-correlation spectroscopy project and especially for having accepted the troubles to fly back to our lab for a Cr:F laser support session.

A particular word of thanks goes to Thiemo Spielmann. I was very fortunate to supervise him during his semester and master projects. His engagement for the projects was outstanding and the Triplet Lifetime Imaging would not have been possible in this form without his work. I am also thankful to Roland Vulliamy for the work he did on this same project during his master project.

Many thanks also to Aurélie Formey for the outstanding cell preparations and handling during the oxygen consumption experiments and the countless coffee-break discussions we had together.

Many thanks goes also to Zuzana Kadlecova for the collaboration with her. Her challenging and scientifically rigorous working mentality was a tremendous source of motivation for the extended triplet lifetime applications on the cellular uptake process. I would also like to thank Virginie Bachmann and Mattia Matasci for their support during that project.

Many thanks also to Prof. Rainer Leitgeb for his valuable ideas and his engagement for the k-microscopy project. It was a true pleasure to collaborate with him and being able to profit of his vast scientific knowledge.

I would also like to thank Martin Villiger, for the interesting discussions we shared together, for his effective help and ideas and for the good times we had together since starting our studies at EPFL together in 2001.

I am very grateful to Erica Martin-Williams for interesting discussions and for proof-reading many of my texts and manuscripts.

Further on, I would like to thank Prof. Dimitri Van De Ville for his work on the linear regression algorithm for the triplet lifetime fitting. If I would estimate the time that his tremendously faster algorithm has saved me during the image processing, I think I owe him several years!

A big word of thanks goes also to Prof. Boris Hinz and Prof. Kai Johnsson for their support of the triplet lifetime project. Both have made fundamental contributions without which the project would not have been possible.

I am very grateful also to Luigi Bonacina for his commitment on the non-linear correlation spectroscopy project and the valuable discussions with him.

Many thanks also to Prof. Jacques-Edouard Moser for the time he has offered to me and Zuzana to discuss the triplet lifetime project.

I would also like to thank Jan Dorn, Sandra Ritz, Serena Belegriou and Prof. Eva-Kathrin Sinner for the collaboration on the FuSyMEM project. For me, the discussions with all of them have been a good source of new knowledge on biology.

I would like to thank Frank Van Mourik, Vincent Vassallo from Spectra-Physics and Chandra Nathala from Femtolasers for discussions about alignment of the Cr:F laser.

I would like to thank Prof. Christophe Moser, Prof. Jacques-Edouard Moser, Christian Eggeling and Luigi Bonacina for accepting to be on my thesis committee. I'm very grateful for their reviewing of this manuscript and their fruitful and interesting feedback and remarks.

Then I would also like to thank all current and former LOB group members for the good working spirit, the great moments we shared at conferences and lab outings and also for the multiple interesting scientific and non-scientific discussions. I would like to thank Christophe Pache, Antonio Lopez, Akihiro Sato, Corinne Berclaz, Arno Bouwens, Nicolas Durand, Thomas Sidler, Stéphane Broillet, Annick Mayor as well as Arnaud Mader, Adrian Bachmann, Kai Hassler, Ramachandra Rao, Denis Ivanov, Roland Michaely, Alberto Bilenca and Michael Friedrich.

A particular word of thanks goes also to Fabienne Ubezio and Judith Chaubert who made my life much easier from an administrative point of view and much nicer from a personal interaction point of view! What a great pleasure to be welcomed every morning at the lab with your great smiles!

Then I would also like to thank Pedro Pascoal for his help with soft lithography, and José Artacho from BIOP for lending a phase-contrast objective whenever needed.

On a personal level, I am very grateful for all the moments I was spending besides my Ph.D. in music&theater rehearsals&performances. Among them I would like to thank the Polyssons, Stéphanie Burkhard, Ioana Benteiu and the CLOP, Fanny Gsteiger and Yves Vocanson for the moments they kept me away from work and for their friendship. I would also like to thank all my friends for their support and understanding during my thesis.

Many profound thanks go to my whole family (Annette, Samuel, Stefan, Senka, Michael, Lukas, Susanne and Walter) for all their support and their patience during my whole studies.

My deepest thank goes to my girlfriend, Sarra Harbi, who shared all the ups and downs of my thesis and supported me throughout this period. I would like to thank her for her love.

Lausanne, 22 July 2011, M. Geissbühler

My religion consists of a humble admiration
of the illimitable superior spirit who reveals
himself in the slight details we are able to
perceive with our frail and feeble mind.

Albert Einstein (1879 - 1955)

Appendix Part IV

A Triplet lifetime imaging: Derivation of average fluorescence intensity

The derivation in this chapter was developed during a semester project and a master project by Thiemo Spielmann [179] under my guidance. It builds on an Ansatz by Marcel Leutenegger [180]. Since the full derivation has so far only been published in the form of a semester project report as well as a master project report [179], I decided to include it in the appendix of my thesis, to make it openly available. A similar derivation has been published by J. Widengren et al. [68]. Our proposition extends this solution for a periodic excitation and an iso-dosis of light illumination.

We start from the second order differential equation 2.4 from page 17 and the ansatz 2.5. We have already identified the constant term b . Let us now write the characteristic equation for the relaxation rate k

$$\tau_S \tau_T k^2 + \left(\tau_S + \tau_T + \frac{\tau_S \tau_T}{\tau_{ex}} \right) k + \left(1 + \frac{\tau_S}{\tau_{ex}} + \frac{\Phi_T \tau_T}{\tau_{ex}} \right) = 0 \quad (\text{A.1})$$

We consider a rectangular pulsed excitation of duration t_p starting at $t = 0$ followed by an *off* period.

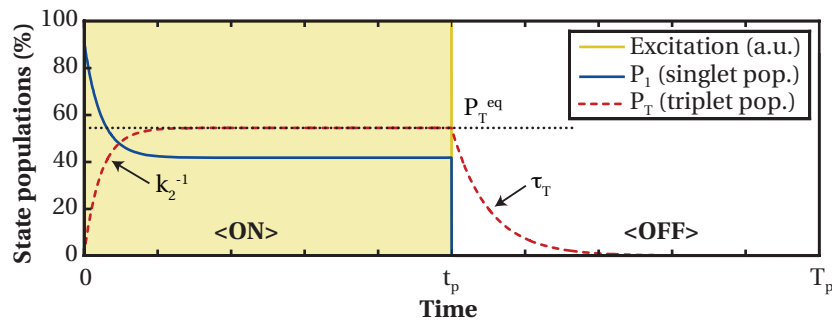


Figure A.1: Model for the evolution of the electronic state populations upon modulated excitation. We assume a periodic rectangular pulse shaped excitation that we divide in an *on* period with a pulse width of t_p and *off* period with a duration of $(T_p - t_p)$.

Appendix A. Triplet lifetime imaging: Derivation of average fluorescence intensity

For the pulse ($1/\tau_{ex} > 0$), the characteristic equation yields the following solution

$$\begin{aligned}
 k_{1,2} = & -\frac{-\left(\tau_S + \tau_T + \frac{\tau_S \tau_T}{\tau_{ex}}\right) \mp \sqrt{\left(\tau_S + \tau_T + \frac{\tau_S \tau_T}{\tau_{ex}}\right)^2 - 4\tau_S \tau_T \left(1 + \frac{\tau_S}{\tau_{ex}} + \frac{\Phi_T \tau_T}{\tau_{ex}}\right)}}{2\tau_S \tau_T} \\
 = & -\frac{1}{2} \left(\frac{1}{\tau_{ex}} + \frac{1}{\tau_S} + \frac{1}{\tau_T} \right) \mp \sqrt{\frac{1}{4} \left(\frac{1}{\tau_{ex}} + \frac{1}{\tau_S} - \frac{1}{\tau_T} \right)^2 - \frac{\Phi_T}{\tau_S \tau_{ex}}}
 \end{aligned} \tag{A.2}$$

It can be shown that $\tau_{ex} = \tau_S$ is a pole of k_1 . By inserting this pole into the above equation A.2 we find

$$\begin{aligned}
 k_1|_{\tau_{ex}=\tau_S} = & -\frac{1}{2} \left(\frac{2}{\tau_S} + \tau_T \right) - \sqrt{\frac{1}{4} \left(\frac{2}{\tau_S} - \frac{1}{\tau_T} \right)^2 - \frac{\Phi_T}{\tau_S^2}} \\
 = & -\frac{1}{2} \left(\frac{2}{\tau_S} + \tau_T \right) - \sqrt{\left(\frac{1}{\tau_S} - \frac{1}{2\tau_T} \right)^2 - \frac{\Phi_T}{\tau_S^2}} \\
 = & -\frac{1}{2} \left(\frac{2}{\tau_S} + \tau_T \right) - \sqrt{\left(\frac{1-\Phi_T}{\tau_S^2} - \frac{1}{\tau_S \tau_T} + \frac{1}{4\tau_T^2} \right)^2}
 \end{aligned}$$

Since we can assume $\Phi_T \ll 1$ we can simplify this to

$$\begin{aligned}
 k_1|_{\tau_{ex}=\tau_S} \approx & -\frac{1}{2} \left(\frac{2}{\tau_S} + \tau_T \right) - \sqrt{\frac{1}{4} \left(\frac{2}{\tau_S} - \frac{1}{\tau_T} \right)^2} \\
 \approx & -\frac{2}{\tau_S}
 \end{aligned}$$

And hence we can rewrite k_1 with a single pole at $\tau_{ex} = \tau_S$

$$\begin{aligned}
 k_1 \approx & -\frac{1}{\tau_S} \left(\frac{\tau_S}{\tau_{ex}} + 1 \right) \\
 \approx & -(\tau_{ex}^{-1} + \tau_S^{-1})
 \end{aligned} \tag{A.3}$$

In a similar way, it can be shown that $\tau_{ex} = (\tau_S + \Phi_T \tau_T)$ is a pole of k_2 . By inserting this pole into the above equation A.2 we find

$$\begin{aligned}
 k_2|_{\tau_{ex}=(\tau_S+\Phi_T\tau_T)} = & -\frac{1}{2} \left(\frac{1}{\tau_S + \Phi_T \tau_T} + \frac{1}{\tau_S} + \tau_T \right) \\
 & + \sqrt{\frac{1}{4} \left(\frac{1}{\tau_S + \Phi_T \tau_T} + \frac{1}{\tau_S} - \frac{1}{\tau_T} \right)^2 - \frac{\Phi_T}{\tau_S(\tau_S + \Phi_T \tau_T)}} \\
 = & -\frac{1}{2} \left(\frac{1}{\tau_S + \Phi_T \tau_T} + \frac{1}{\tau_S} + \tau_T \right) \\
 & + \sqrt{\frac{1}{4} \left[\left(\frac{1}{\tau_S + \Phi_T \tau_T} \right)^2 + 2 \left(\frac{1}{\tau_S \tau_T} \frac{\tau_T - \tau_S - \Phi_T \tau_T}{\tau_S + \Phi_T \tau_T} \right) + \left(\frac{\tau_T - \tau_S}{\tau_S \tau_T} \right)^2 \right]}
 \end{aligned}$$

We can assume $\Phi_T \tau_T \ll \tau_T$, which simplifies the above equation to

$$\begin{aligned} k_2|_{\tau_{ex}=(\tau_S+\Phi_T\tau_T)} &\approx -\frac{1}{2} \left(\frac{1}{\tau_S+\Phi_T\tau_T} + \frac{1}{\tau_S} + \tau_T \right) \\ &\quad + \sqrt{\frac{1}{4} \left[\left(\frac{1}{\tau_S+\Phi_T\tau_T} \right)^2 + 2 \left(\frac{1}{\tau_S\tau_T} \frac{\tau_T-\tau_S}{\tau_S+\Phi_T\tau_T} \right) + \left(\frac{\tau_T-\tau_S}{\tau_S\tau_T} \right)^2 \right]} \\ &\approx -\frac{1}{2} \left(\frac{1}{\tau_S+\Phi_T\tau_T} + \frac{1}{\tau_S} + \tau_T \right) + \sqrt{\frac{1}{4} \left(\frac{1}{\tau_S+\Phi_T\tau_T} + \frac{1}{\tau_S} - \frac{1}{\tau_T} \right)^2} \\ &\approx -\frac{1}{\tau_T} \end{aligned}$$

And hence we can rewrite k_2 with a single pole at $\tau_{ex} = (\tau_S + \Phi_T \tau_T)$

$$\begin{aligned} k_2 &= -\frac{1}{\tau_T} \left(\frac{\tau_S + \Phi_T \tau_T}{\tau_S + \frac{\Phi_T \tau_T}{1 + \frac{\tau_S + \Phi_T \tau_T}{\tau_{ex}}}} \right) \\ &= -\frac{1}{\tau_T} \left(\frac{(\tau_S + \Phi_T \tau_T)(\tau_{ex} + \tau_S + \Phi_T \tau_T)}{\tau_{ex}(\tau_S + \Phi_T \tau_T) + \tau_S(\tau_S + \Phi_T \tau_T)} \right) \\ &= -\frac{1}{\tau_T} \left(\frac{\tau_{ex} + \tau_S + \Phi_T \tau_T}{\tau_{ex} + \tau_S} \right) \end{aligned} \tag{A.4}$$

It is interesting to rewrite this rate with the help of equation 2.6

$$\frac{1}{k_2} = -\tau_T(1 - P_T^{\text{eq}}) \tag{A.5}$$

Using these rates, we can express the temporal evolution of the triplet population at the onset of the pulse as according to equation 2.5 and 2.6 as

$$\begin{aligned} P_T^{\text{on}}(t) &= a_1 \exp(k_1 t) + a_2 \exp(k_2 t) + P_T^{\text{eq}} \\ &\approx a_2 \exp(k_2 t) + P_T^{\text{eq}} \end{aligned} \tag{A.6}$$

Where we have neglected the rate k_1 , since for the timescale of interest, this exponential decay can be considered immediate since $-k_1 \ll -k_2$.

Starting again from equation 2.4, we derive the characteristic equation for the *off* period ($1/\tau_{ex} = 0$).

$$k^2 + \left(\frac{\tau_S + \tau_T}{\tau_S \tau_T} \right) k + 1 = 0 \tag{A.7}$$

which can be easily simplified to yield

$$\begin{aligned} k_{3,4} &= \frac{-\left(\frac{\tau_S + \tau_T}{\tau_S \tau_T} \right) \pm \sqrt{\left(\frac{\tau_S + \tau_T}{\tau_S \tau_T} \right)^2 - 4}}{2} \\ &= \left\{ -\frac{1}{\tau_S}; -\frac{1}{\tau_T} \right\} \end{aligned} \tag{A.8}$$

Hence with these rates we can write the triplet population for the case without excitation (after the pulse) as

$$\begin{aligned} P_T^{\text{off}}(t) &= a_3 \exp\left(-\frac{t}{\tau_S}\right) + a_4 \exp\left(-\frac{t}{\tau_T}\right) \\ &\approx a_4 \exp\left(-\frac{t}{\tau_T}\right) \end{aligned} \tag{A.9}$$

Appendix A. Triplet lifetime imaging: Derivation of average fluorescence intensity

Where we employed $\tau_S \ll \tau_T$ as approximation. Hence in summary, the triplet population evolution during a rectangular pulse shaped excitation with a duration of t_p is described by

$$P_T(t) = \begin{cases} a_2 \exp(k_2 t) + P_T^{\text{eq}} & \text{for } 0 < t < t_p \\ a_4 \exp\left(-\frac{1}{\tau_T}(t - t_p)\right) & \text{for } t > t_p \end{cases} \quad (\text{A.10})$$

The boundary conditions must be chosen to ensure a continuity of the triplet population. For the moment when the excitation is stopped (at $t = t_p$) we find:

$$\begin{aligned} P_T(t_p^+) &= P_T(t_p^-) \\ a_4 &= a_2 \exp(k_2 t_p) + P_T^{\text{eq}} \end{aligned} \quad (\text{A.11})$$

Further on, for a periodic excitation with a periodicity of T_p , the triplet population at the beginning must be equal to the population at the end and hence

$$\begin{aligned} P_T(0^+) &= P_T(T_p^-) \\ a_2 + P_T^{\text{eq}} &= a_4 \exp\left(-\frac{1}{\tau_T}(T_p - t_p)\right) \end{aligned} \quad (\text{A.12})$$

Hence by inserting the first boundary condition A.11 into the second A.12, we find

$$a_2 = -\frac{P_T^{\text{eq}} \left(1 - \exp\left(-\frac{1}{\tau_T}(T_p - t_p)\right)\right)}{1 - \exp\left(-\frac{1}{\tau_T}(T_p - t_p) + k_2 t_p\right)} \quad (\text{A.13})$$

We are interested in deriving an expression for the average fluorescence intensity. Hence we need to use the above expression to find the evolution of the singlet population. We start from the third equation of the rate equations 2.1 to find

$$\begin{aligned} P_I &= \frac{\tau_S}{\Phi_T} \left(\frac{dP_T}{dt} + \frac{1}{\tau_T} P_T \right) \\ &= \begin{cases} \frac{\tau_S}{\Phi_T} \left(a_2 k_2 \exp(k_2 t) + a_2 \frac{1}{\tau_T} \exp(k_2 t) + \frac{1}{\tau_T} P_T^{\text{eq}} \right) & \text{for } 0 < t < t_p \\ \frac{\tau_S}{\Phi_T} \left(a_4 \frac{1}{\tau_T} \exp\left(-\frac{1}{\tau_T}(t - t_p)\right) + a_4 \frac{1}{\tau_T} \exp\left(-\frac{1}{\tau_T}(t - t_p)\right) \right) & \text{for } t > t_p \end{cases} \\ &= \begin{cases} \frac{\tau_S}{\Phi_T} \left(a_2 \left(k_2 + \frac{1}{\tau_T} \right) \exp(k_2 t) + \frac{1}{\tau_T} P_T^{\text{eq}} \right) & \text{for } 0 < t < t_p \\ 0 & \text{for } t > t_p \end{cases} \end{aligned} \quad (\text{A.14})$$

The fluorescence intensity that is detected, can be expressed by

$$\overline{I_{F'}(\vec{r})} = \eta' \Gamma(\vec{r}) \Phi_F \frac{\overline{P_I}}{\tau_S} \quad (\text{A.15})$$

Where \overline{P}_l is the time averaged singlet state population over one period and $\Gamma(\vec{r})$ is the local concentration of fluorophores, η' is a conversion factor between the emitted intensity and the digital readout of the camera. With the help of equation A.14 we calculate

$$\begin{aligned}\overline{P}_l &= \frac{1}{T_p} \int_0^{T_p} P_l dt = \frac{1}{T_p} \int_0^{t_p} P_l dt \\ &= \frac{1}{T_p} \int_0^{t_p} \frac{\tau_S}{\Phi_T} \left(a_2 \left(k_2 + \frac{1}{\tau_T} \right) \exp(k_2 t) + \frac{1}{\tau_T} P_T^{\text{eq}} \right) dt \\ &= \frac{1}{T_p} \frac{\tau_S}{\Phi_T} \left(a_2 \frac{1}{k_2} \left(k_2 + \frac{1}{\tau_T} \right) (\exp(k_2 t_p) - 1) + \frac{1}{\tau_T} P_T^{\text{eq}} t_p \right)\end{aligned}\quad (\text{A.16})$$

since with the help of equation A.5 we find

$$\frac{1}{k_2} \left(k_2 + \frac{1}{\tau_T} \right) = \left(1 + \frac{1}{\tau_T k_2} \right) = \left(1 + \frac{1}{\tau_T} (-\tau_T(1 - P_T^{\text{eq}})) \right) = P_T^{\text{eq}} \quad (\text{A.17})$$

it follows

$$\begin{aligned}\overline{P}_l &= \frac{1}{T_p} \frac{\tau_S}{\Phi_T} P_T^{\text{eq}} \left(a_2 (\exp(k_2 t_p) - 1) + \frac{1}{\tau_T} t_p \right) \\ &= \frac{1}{T_p} \frac{\tau_S}{\Phi_T} P_T^{\text{eq}} \left(-\frac{P_T^{\text{eq}} (1 - \exp(-\frac{1}{\tau_T}(T_p - t_p)))}{1 - \exp(-\frac{1}{\tau_T}(T_p - t_p) + k_2 t_p)} (\exp(k_2 t_p) - 1) + \frac{1}{\tau_T} t_p \right)\end{aligned}\quad (\text{A.18})$$

Insertion into equation A.15 yields directly the desired mean fluorescence intensity

$$\begin{aligned}\overline{I_F(\vec{r})} &= \eta' \Gamma(\vec{r}) \Phi_F \frac{1}{\tau_S} \times \frac{1}{T_p} \frac{\tau_S}{\Phi_T} P_T^{\text{eq}} \frac{t_p}{\tau_T} \left(1 - \frac{\tau_T P_T^{\text{eq}} (1 - \exp(-\frac{(T_p - t_p)}{\tau_T}))}{1 - \exp(-\frac{(T_p - t_p)}{\tau_T} + k_2 t_p)} \times \frac{(\exp(k_2 t_p) - 1)}{t_p} \right) \\ &= \gamma(\vec{r}) t_p \left(1 - \frac{\tau_T P_T^{\text{eq}} (1 - \exp(-\frac{(T_p - t_p)}{\tau_T}))}{1 - \exp(-\frac{(T_p - t_p)}{\tau_T} + k_2 t_p)} \times \frac{(\exp(k_2 t_p) - 1)}{t_p} \right)\end{aligned}\quad (\text{A.19})$$

where we have defined $\eta = \eta'/T_p$ and

$$\gamma(\vec{r}) = \eta \Gamma(\vec{r}) \frac{\Phi_F}{\tau_{\text{ex}} + \tau_S + \Phi_T \tau_T} \quad (\text{A.20})$$

Finally the average fluorescence intensity for an iso-dosis of light exposure is simply given by dividing equation A.19 by t_p

$$\overline{I_F(\vec{r})} = \gamma(\vec{r}) \left(1 - \frac{\tau_T P_T^{\text{eq}} (1 - \exp(-\frac{(T_p - t_p)}{\tau_T}))}{1 - \exp(-\frac{(T_p - t_p)}{\tau_T} + k_2 t_p)} \times \frac{(\exp(k_2 t_p) - 1)}{t_p} \right) \quad (\text{A.21})$$

B Nonlinear correlation spectroscopy - Autocorrelation theory

The development of the autocorrelation function has been done together with my brother S. Geissbuehler. I decided to include it in the appendix of my thesis for completeness of the nonlinear correlation spectroscopy part, although the derivation is rather lengthy.

The goal is to derive an analytical expression for the normalized autocorrelation of the q th harmonic generation intensity

$$G(\tau) = \frac{\langle I_q(t+\tau)I_q(t) \rangle - \langle I_q(t) \rangle^2}{\langle I_q(t) \rangle^2} = \frac{\langle \delta I_q(t+\tau)\delta I_q(t) \rangle}{\langle I_q(t) \rangle^2} \quad (\text{B.1})$$

where $I_q(t)$ is the q th harmonic generation intensity at time t , $\langle I_q(t) \rangle$ is the corresponding time-averaged intensity and $\delta I_q(t) = I_q(t) - \langle I_q(t) \rangle$ is the intensity fluctuation at time t .

We start by approximating our focal volume with a three-dimensional gaussian volume as given in equation 6.13 on page 72 including a linear axial phase factor that can incorporate a phase mismatch or an approximation of the Gouy phase shift. We separate the expression into real and complex parts and define $A_q^*(\mathbf{r})$ for shorter notation

$$\begin{aligned} A_q(\mathbf{r}) &\approx A_{q0} \exp\left(-\frac{x^2+y^2}{\omega_0^2/q}\right) \exp\left(-\frac{z^2}{z_0^2/q}\right) \exp(-i\kappa_q z) \\ &= A_{q0} \exp\left(-\frac{x^2+y^2}{\omega_0^2/q}\right) \exp\left(-\frac{z^2}{z_0^2/q}\right) (\cos(\kappa_q z) - i \sin(\kappa_q z)) \\ &= A_q^*(\mathbf{r}) (\cos(\kappa_q z) - i \sin(\kappa_q z)) \end{aligned} \quad (\text{B.2})$$

with this, we write the intensity on the detector for the q th harmonic signal as

$$\begin{aligned} I_q(t) &= \left| \int \chi_s^{(q)} A_q(\mathbf{r}) c(\mathbf{r}, t) dV \right|^2 \\ &= |\chi_s^{(q)}|^2 \left(\left(\int A_q^*(\mathbf{r}) \cos(\kappa_q z) c(\mathbf{r}, t) dV \right)^2 + |\chi_s^{(q)}|^2 \left(\int A_q^*(\mathbf{r}) \sin(\kappa_q z) c(\mathbf{r}, t) dV \right)^2 \right) \end{aligned} \quad (\text{B.3})$$

Appendix B. Nonlinear correlation spectroscopy - Autocorrelation theory

With Fubini's theorem $\left(\int f(x)dx\right)^2 = \iint f(x_1)f(x_2)dx_1dx_2$ we can rewrite this into

$$I_q(t) = |\chi_s^{(q)}|^2 \iint A_q^*(\mathbf{r}_1)A_q^*(\mathbf{r}_2)\cos(\kappa_q z_1)\cos(\kappa_q z_2)c(\mathbf{r}_1, t)c(\mathbf{r}_2, t)dV_1dV_2 \\ + |\chi_s^{(q)}|^2 \iint A_q^*(\mathbf{r}_1)A_q^*(\mathbf{r}_2)\sin(\kappa_q z_1)\sin(\kappa_q z_2)c(\mathbf{r}_1, t)c(\mathbf{r}_2, t)dV_1dV_2 \quad (\text{B.4})$$

As proposed by Palmer et al. [181] we separate the concentration terms using $c(\mathbf{r}, t) = \langle c \rangle + \delta c(\mathbf{r}, t)$ yielding

$$I_q(t) = |\chi_s^{(q)}|^2 \iint A_q^*(\mathbf{r}_1)A_q^*(\mathbf{r}_2)\cos(\kappa_q z_1)\cos(\kappa_q z_2) \\ \times [\langle c \rangle^2 + \langle c \rangle(\delta c(\mathbf{r}_1, t) + \delta c(\mathbf{r}_2, t)) + \delta c(\mathbf{r}_1, t)\delta c(\mathbf{r}_2, t)] dV_1dV_2 \\ + |\chi_s^{(q)}|^2 \iint A_q^*(\mathbf{r}_1)A_q^*(\mathbf{r}_2)\sin(\kappa_q z_1)\sin(\kappa_q z_2) \\ \times [\langle c \rangle^2 + \langle c \rangle(\delta c(\mathbf{r}_1, t) + \delta c(\mathbf{r}_2, t)) + \delta c(\mathbf{r}_1, t)\delta c(\mathbf{r}_2, t)] dV_1dV_2 \quad (\text{B.5})$$

We will now perform the time average of this signal. According to our definition for the concentration terms above $\langle \delta c(\mathbf{r}_i, t) \rangle = 0$. Further on, we can use the definitions from Palmer et al. [181]

$$f_{mn}(\mathbf{r}_1, \mathbf{r}_2, \dots, \mathbf{r}_{m+n}, \tau) = \langle \delta c(\mathbf{r}_1, t + \tau) \cdot \delta c(\mathbf{r}_2, t + \tau) \cdots \delta c(\mathbf{r}_m, t + \tau) \\ \cdot \delta c(\mathbf{r}_{m+1}, t) \cdot \delta c(\mathbf{r}_{m+2}, t) \cdots \delta c(\mathbf{r}_{m+n}, t) \rangle \\ - \langle \delta c(\mathbf{r}_1, t + \tau) \cdot \delta c(\mathbf{r}_2, t + \tau) \cdots \delta c(\mathbf{r}_m, t + \tau) \rangle \\ \cdot \langle \delta c(\mathbf{r}_{m+1}, t) \cdot \delta c(\mathbf{r}_{m+2}, t) \cdots \delta c(\mathbf{r}_{m+n}, t) \rangle \quad (\text{B.6})$$

Hence we identify $\langle \delta c(\mathbf{r}_1, t) \delta c(\mathbf{r}_2, t) \rangle = f_{11}(\mathbf{r}_1, \mathbf{r}_2, 0)$. And according to equations B11 and B10 in [181] we can write $f_{11}(\mathbf{r}_1, \mathbf{r}_2, 0) = \langle c \rangle \delta(\mathbf{r}_1 - \mathbf{r}_2)$. As a result it follows

$$\langle I_q(t) \rangle = \langle c \rangle^2 |\chi_s^{(q)}|^2 \iint A_q^*(\mathbf{r}_1)A_q^*(\mathbf{r}_2)\cos(\kappa_q z_1)\cos(\kappa_q z_2)dV_1dV_2 \\ + \langle c \rangle |\chi_s^{(q)}|^2 \int \left(A_q^*(\mathbf{r})\right)^2 \cos^2(\kappa_q z) dV \\ + \langle c \rangle^2 |\chi_s^{(q)}|^2 \iint A_q^*(\mathbf{r}_1)A_q^*(\mathbf{r}_2)\sin(\kappa_q z_1)\sin(\kappa_q z_2)dV_1dV_2 \\ + \langle c \rangle |\chi_s^{(q)}|^2 \int \left(A_q^*(\mathbf{r})\right)^2 \sin^2(\kappa_q z) dV \quad (\text{B.7})$$

Starting from equation B.4 we can derive an expression for the autocorrelation of the intensity signal as follows

$$\langle I_q(t + \tau)I_q(t) \rangle = |\chi_s^{(q)}|^4 \iiint \langle c(\mathbf{r}_1, t + \tau)c(\mathbf{r}_2, t + \tau)c(\mathbf{r}_3, t)c(\mathbf{r}_4, t) \rangle \prod_{i=1}^4 A_q^*(\mathbf{r}_i)\cos(\kappa_q z_i) dV_i \\ + 2|\chi_s^{(q)}|^4 \iiint \langle c(\mathbf{r}_1, t + \tau)c(\mathbf{r}_2, t + \tau)c(\mathbf{r}_3, t)c(\mathbf{r}_4, t) \rangle \\ \times \cos(\kappa_q z_1)\cos(\kappa_q z_3)\sin(\kappa_q z_2)\sin(\kappa_q z_4) \prod_{i=1}^4 A_q^*(\mathbf{r}_i) dV_i \\ + |\chi_s^{(q)}|^4 \iiint \langle c(\mathbf{r}_1, t + \tau)c(\mathbf{r}_2, t + \tau)c(\mathbf{r}_3, t)c(\mathbf{r}_4, t) \rangle \prod_{i=1}^4 A_q^*(\mathbf{r}_i)\sin(\kappa_q z_i) dV_i \quad (\text{B.8})$$

As a useful alternative to equation B.7, let us directly express the *squared* time-average of the signal by starting from equation B.4 to yield

$$\begin{aligned}
\langle I_q(t) \rangle^2 &= |\chi_s^{(q)}|^4 \iiint \langle c(\mathbf{r}_1, t) c(\mathbf{r}_2, t) \rangle \langle c(\mathbf{r}_3, t) c(\mathbf{r}_4, t) \rangle \prod_{i=1}^4 A_q^*(\mathbf{r}_i) \cos(\kappa_q z_i) dV_i \\
&\quad + 2 |\chi_s^{(q)}|^4 \iiint \langle c(\mathbf{r}_1, t) c(\mathbf{r}_2, t) \rangle \langle c(\mathbf{r}_3, t) c(\mathbf{r}_4, t) \rangle \\
&\quad \times \cos(\kappa_q z_1) \cos(\kappa_q z_2) \sin(\kappa_q z_3) \sin(\kappa_q z_4) \prod_{i=1}^4 A_q^*(\mathbf{r}_i) dV_i \\
&\quad + |\chi_s^{(q)}|^4 \iiint \langle c(\mathbf{r}_1, t) c(\mathbf{r}_2, t) \rangle \langle c(\mathbf{r}_3, t) c(\mathbf{r}_4, t) \rangle \prod_{i=1}^4 A_q^*(\mathbf{r}_i) \sin(\kappa_q z_i) dV_i
\end{aligned} \tag{B.9}$$

Since all integrands of sine functions in equations B.8 and B.9 are anti-symmetric around the origin $\mathbf{r} = \{0, 0, 0\}$, the addends two and three are 0. Equation B.8 can thus be simplified to

$$\langle I_q(t + \tau) I_q(t) \rangle = |\chi_s^{(q)}|^4 \iiint \underbrace{\langle c(\mathbf{r}_1, t + \tau) c(\mathbf{r}_2, t + \tau) c(\mathbf{r}_3, t) c(\mathbf{r}_4, t) \rangle}_{\mathcal{C}_1(\mathbf{r}_1, \mathbf{r}_2, \mathbf{r}_3, \mathbf{r}_4, t, \tau)} \prod_{i=1}^4 A_q^*(\mathbf{r}_i) \cos(\kappa_q z_i) dV_i \tag{B.10}$$

and for equation B.9 we find

$$\begin{aligned}
\langle I_q(t) \rangle^2 &= |\chi_s^{(q)}|^4 \iiint \underbrace{\langle c(\mathbf{r}_1, t) c(\mathbf{r}_2, t) \rangle \langle c(\mathbf{r}_3, t) c(\mathbf{r}_4, t) \rangle}_{\mathcal{C}_2(\mathbf{r}_1, \mathbf{r}_2, \mathbf{r}_3, \mathbf{r}_4, t, \tau)} \prod_{i=1}^4 A_q^*(\mathbf{r}_i) \cos(\kappa_q z_i) dV_i \\
&= |\chi_s^{(q)}|^4 \iiint \left[\langle c \rangle^4 + 2 \langle c \rangle^3 \delta(\mathbf{r}_1 - \mathbf{r}_2) + \langle c \rangle^2 \delta(\mathbf{r}_1 - \mathbf{r}_2) \delta(\mathbf{r}_3 - \mathbf{r}_4) \right] \\
&\quad \times \prod_{i=1}^4 A_q^*(\mathbf{r}_i) \cos(\kappa_q z_i) dV_i
\end{aligned} \tag{B.11}$$

As a quick cross-check, we see that equation B.11 is equal to the square of B.7 if the same assumptions are made.

The term with the time average of concentrations in equation B.10 can be simplified with the help of the equations and definitions in [181]:

$$\begin{aligned}
\mathcal{C}_1(\mathbf{r}_1, \mathbf{r}_2, \mathbf{r}_3, \mathbf{r}_4, t, \tau) &\equiv \langle c(\mathbf{r}_1, t + \tau) c(\mathbf{r}_2, t + \tau) c(\mathbf{r}_3, t) c(\mathbf{r}_4, t) \rangle \\
&= (\langle c \rangle + \delta c(\mathbf{r}_1, t + \tau)) (\langle c \rangle + \delta c(\mathbf{r}_2, t + \tau)) \\
&\quad \times (\langle c \rangle + \delta c(\mathbf{r}_3, t)) (\langle c \rangle + \delta c(\mathbf{r}_4, t)) \\
&= \langle c \rangle^4 \\
&\quad + \langle c \rangle^2 \langle \delta c(\mathbf{r}_1, t + \tau) \delta c(\mathbf{r}_2, t + \tau) \rangle + \langle c \rangle^2 \langle \delta c(\mathbf{r}_1, t + \tau) \delta c(\mathbf{r}_3, t) \rangle \\
&\quad + \langle c \rangle^2 \langle \delta c(\mathbf{r}_1, t + \tau) \delta c(\mathbf{r}_4, t) \rangle + \langle c \rangle^2 \langle \delta c(\mathbf{r}_2, t + \tau) \delta c(\mathbf{r}_3, t) \rangle \\
&\quad + \langle c \rangle^2 \langle \delta c(\mathbf{r}_2, t + \tau) \delta c(\mathbf{r}_4, t) \rangle + \langle c \rangle^2 \langle \delta c(\mathbf{r}_3, t) \delta c(\mathbf{r}_4, t) \rangle \\
&\quad + \langle c \rangle \langle \delta c(\mathbf{r}_1, t + \tau) \delta c(\mathbf{r}_2, t + \tau) \delta c(\mathbf{r}_3, t) \rangle \\
&\quad + \langle c \rangle \langle \delta c(\mathbf{r}_1, t + \tau) \delta c(\mathbf{r}_2, t + \tau) \delta c(\mathbf{r}_4, t) \rangle \\
&\quad + \langle c \rangle \langle \delta c(\mathbf{r}_1, t + \tau) \delta c(\mathbf{r}_3, t) \delta c(\mathbf{r}_4, t) \rangle \\
&\quad + \langle c \rangle \langle \delta c(\mathbf{r}_2, t + \tau) \delta c(\mathbf{r}_3, t) \delta c(\mathbf{r}_4, t) \rangle \\
&\quad + \langle \delta c(\mathbf{r}_1, t + \tau) \delta c(\mathbf{r}_2, t + \tau) \delta c(\mathbf{r}_3, t) \delta c(\mathbf{r}_4, t) \rangle
\end{aligned} \tag{B.12}$$

Using the definition of equation B.6 we rewrite this as

$$\begin{aligned}
 \mathcal{C}_1(\mathbf{r}_1, \mathbf{r}_2, \mathbf{r}_3, \mathbf{r}_4, t, \tau) = & \langle c \rangle^4 + \langle c \rangle^2 f_{11}(\mathbf{r}_1, \mathbf{r}_2, 0) + \langle c \rangle^2 f_{11}(\mathbf{r}_1, \mathbf{r}_3, \tau) \\
 & + \langle c \rangle^2 f_{11}(\mathbf{r}_1, \mathbf{r}_4, \tau) + \langle c \rangle^2 f_{11}(\mathbf{r}_2, \mathbf{r}_3, \tau) \\
 & + \langle c \rangle^2 f_{11}(\mathbf{r}_2, \mathbf{r}_4, \tau) + \langle c \rangle^2 f_{11}(\mathbf{r}_3, \mathbf{r}_4, 0) \\
 & + \langle c \rangle f_{21}(\mathbf{r}_1, \mathbf{r}_2, \mathbf{r}_3, \tau) + \langle c \rangle f_{21}(\mathbf{r}_1, \mathbf{r}_2, \mathbf{r}_4, \tau) \\
 & + \langle c \rangle f_{12}(\mathbf{r}_1, \mathbf{r}_3, \mathbf{r}_4, \tau) + \langle c \rangle f_{12}(\mathbf{r}_2, \mathbf{r}_3, \mathbf{r}_4, \tau) \\
 & + f_{22}(\mathbf{r}_1, \mathbf{r}_2, \mathbf{r}_3, \mathbf{r}_4, \tau) + f_{11}(\mathbf{r}_1, \mathbf{r}_2, 0) f_{11}(\mathbf{r}_3, \mathbf{r}_4, 0)
 \end{aligned} \tag{B.13}$$

According to Steinberg [182], fluctuation signals of systems in equilibrium can be reversed in time, since the resulting noise has statistical properties that are invariant in time. Therefore $f_{n,m}(t) = f_{m,n}(t)$ and hence we can write the above equation as

$$\begin{aligned}
 \mathcal{C}_1(\mathbf{r}_1, \mathbf{r}_2, \mathbf{r}_3, \mathbf{r}_4, t, \tau) = & \langle c \rangle^4 + \langle c \rangle^2 f_{11}(\mathbf{r}_1, \mathbf{r}_2, 0) + \langle c \rangle^2 f_{11}(\mathbf{r}_1, \mathbf{r}_3, \tau) \\
 & + \langle c \rangle^2 f_{11}(\mathbf{r}_1, \mathbf{r}_4, \tau) + \langle c \rangle^2 f_{11}(\mathbf{r}_2, \mathbf{r}_3, \tau) \\
 & + \langle c \rangle^2 f_{11}(\mathbf{r}_2, \mathbf{r}_4, \tau) + \langle c \rangle^2 f_{11}(\mathbf{r}_3, \mathbf{r}_4, 0) \\
 & + \langle c \rangle f_{12}(\mathbf{r}_3, \mathbf{r}_1, \mathbf{r}_2, -\tau) + \langle c \rangle f_{12}(\mathbf{r}_4, \mathbf{r}_1, \mathbf{r}_2, -\tau) \\
 & + \langle c \rangle f_{12}(\mathbf{r}_1, \mathbf{r}_3, \mathbf{r}_4, \tau) + \langle c \rangle f_{12}(\mathbf{r}_2, \mathbf{r}_3, \mathbf{r}_4, \tau) \\
 & + f_{22}(\mathbf{r}_1, \mathbf{r}_2, \mathbf{r}_3, \mathbf{r}_4, \tau) + f_{11}(\mathbf{r}_1, \mathbf{r}_2, 0) f_{11}(\mathbf{r}_3, \mathbf{r}_4, 0) \\
 = & \langle c \rangle^4 + \langle c \rangle^2 f_{11}(\mathbf{r}_1, \mathbf{r}_2, 0) + \langle c \rangle^2 f_{11}(\mathbf{r}_1, \mathbf{r}_3, \tau) \\
 & + \langle c \rangle^2 f_{11}(\mathbf{r}_1, \mathbf{r}_4, \tau) + \langle c \rangle^2 f_{11}(\mathbf{r}_2, \mathbf{r}_3, \tau) \\
 & + \langle c \rangle^2 f_{11}(\mathbf{r}_2, \mathbf{r}_4, \tau) + \langle c \rangle^2 f_{11}(\mathbf{r}_3, \mathbf{r}_4, 0) \\
 & + \langle c \rangle f_{12}(\mathbf{r}_3, \mathbf{r}_1, \mathbf{r}_2, \tau) + \langle c \rangle f_{12}(\mathbf{r}_4, \mathbf{r}_1, \mathbf{r}_2, \tau) \\
 & + \langle c \rangle f_{12}(\mathbf{r}_1, \mathbf{r}_3, \mathbf{r}_4, \tau) + \langle c \rangle f_{12}(\mathbf{r}_2, \mathbf{r}_3, \mathbf{r}_4, \tau) \\
 & + f_{22}(\mathbf{r}_1, \mathbf{r}_2, \mathbf{r}_3, \mathbf{r}_4, \tau) + f_{11}(\mathbf{r}_1, \mathbf{r}_2, 0) f_{11}(\mathbf{r}_3, \mathbf{r}_4, 0)
 \end{aligned} \tag{B.14}$$

The entitites f_{mn} have been calculated by Palmer et al. [181] in his equations B11. Using these solutions we find

$$\begin{aligned}
 \mathcal{C}_1(\mathbf{r}_1, \mathbf{r}_2, \mathbf{r}_3, \mathbf{r}_4, t, \tau) = & \langle c \rangle^4 + \langle c \rangle^3 \delta(\mathbf{r}_1 - \mathbf{r}_2) + \frac{\langle c \rangle^3}{(4\pi D\tau)^{3/2}} \exp\left(-\frac{\|\mathbf{r}_1 - \mathbf{r}_3 + \mathbf{V}\tau\|^2}{4D\tau}\right) \\
 & + \frac{\langle c \rangle^3}{(4\pi D\tau)^{3/2}} \exp\left(-\frac{\|\mathbf{r}_1 - \mathbf{r}_4 + \mathbf{V}\tau\|^2}{4D\tau}\right) + \frac{\langle c \rangle^3}{(4\pi D\tau)^{3/2}} \exp\left(-\frac{\|\mathbf{r}_2 - \mathbf{r}_3 + \mathbf{V}\tau\|^2}{4D\tau}\right) \\
 & + \frac{\langle c \rangle^3}{(4\pi D\tau)^{3/2}} \exp\left(-\frac{\|\mathbf{r}_2 - \mathbf{r}_4 + \mathbf{V}\tau\|^2}{4D\tau}\right) + \langle c \rangle^3 \delta(\mathbf{r}_3 - \mathbf{r}_4) \\
 & + \frac{\langle c \rangle^2 \delta(\mathbf{r}_1 - \mathbf{r}_2)}{(4\pi D\tau)^{3/2}} \exp\left(-\frac{\|\mathbf{r}_1 - \mathbf{r}_3 + \mathbf{V}\tau\|^2}{4D\tau}\right) + \frac{\langle c \rangle^2 \delta(\mathbf{r}_1 - \mathbf{r}_2)}{(4\pi D\tau)^{3/2}} \exp\left(-\frac{\|\mathbf{r}_1 - \mathbf{r}_4 + \mathbf{V}\tau\|^2}{4D\tau}\right) \\
 & + \frac{\langle c \rangle^2 \delta(\mathbf{r}_3 - \mathbf{r}_4)}{(4\pi D\tau)^{3/2}} \exp\left(-\frac{\|\mathbf{r}_1 - \mathbf{r}_3 + \mathbf{V}\tau\|^2}{4D\tau}\right) + \frac{\langle c \rangle^2 \delta(\mathbf{r}_3 - \mathbf{r}_4)}{(4\pi D\tau)^{3/2}} \exp\left(-\frac{\|\mathbf{r}_2 - \mathbf{r}_3 + \mathbf{V}\tau\|^2}{4D\tau}\right) \\
 & + \frac{\langle c \rangle \delta(\mathbf{r}_1 - \mathbf{r}_2) \delta(\mathbf{r}_3 - \mathbf{r}_4)}{(4\pi D\tau)^{3/2}} \exp\left(-\frac{\|\mathbf{r}_1 - \mathbf{r}_3 + \mathbf{V}\tau\|^2}{4D\tau}\right) \\
 & + \frac{\langle c \rangle^2}{64\pi^3 D^3 \tau^3} \exp\left(-\frac{\|\mathbf{r}_1 - \mathbf{r}_3 + \mathbf{V}\tau\|^2}{4D\tau}\right) \exp\left(-\frac{\|\mathbf{r}_2 - \mathbf{r}_4 + \mathbf{V}\tau\|^2}{4D\tau}\right) \\
 & + \frac{\langle c \rangle^2}{64\pi^3 D^3 \tau^3} \exp\left(-\frac{\|\mathbf{r}_1 - \mathbf{r}_4 + \mathbf{V}\tau\|^2}{4D\tau}\right) \exp\left(-\frac{\|\mathbf{r}_2 - \mathbf{r}_3 + \mathbf{V}\tau\|^2}{4D\tau}\right) \\
 & + \langle c \rangle^2 \delta(\mathbf{r}_1 - \mathbf{r}_2) \delta(\mathbf{r}_3 - \mathbf{r}_4)
 \end{aligned} \tag{B.15}$$

Here we have included a term $\mathbf{V}\tau$ as proposed by Palmer et al. [181] that takes care of an eventual additional flow component. The flow is assumed to be uniform over the sample volume, in other words we assume simply an additional uniform translation with a velocity vector \mathbf{V} . It is generally a valid approximation for many types of flows, since the observation volume can be considered small compared to the dimension of the flow profile.

In a similar way, we can simplify the correlation term in equation B.11

$$\begin{aligned}
\mathcal{C}_2(\mathbf{r}_1, \mathbf{r}_2, \mathbf{r}_3, \mathbf{r}_4, t, \tau) &\equiv \langle c(\mathbf{r}_1, t) c(\mathbf{r}_2, t) \rangle \langle c(\mathbf{r}_3, t) c(\mathbf{r}_4, t) \rangle \\
&= (\langle c \rangle^2 + \langle \delta c(\mathbf{r}_1, t) \delta c(\mathbf{r}_2, t) \rangle) (\langle c \rangle^2 + \langle \delta c(\mathbf{r}_3, t) \delta c(\mathbf{r}_4, t) \rangle) \\
&= \langle c \rangle^4 + \langle c \rangle^2 \langle \delta c(\mathbf{r}_1, t) \delta c(\mathbf{r}_2, t) \rangle + \langle c \rangle^2 \langle \delta c(\mathbf{r}_3, t) \delta c(\mathbf{r}_4, t) \rangle \\
&\quad + \langle \delta c(\mathbf{r}_1, t) \delta c(\mathbf{r}_2, t) \rangle \langle \delta c(\mathbf{r}_3, t) \delta c(\mathbf{r}_4, t) \rangle \\
&= \langle c \rangle^4 + \langle c \rangle^3 \delta(\mathbf{r}_1 - \mathbf{r}_2) + \langle c \rangle^3 \delta(\mathbf{r}_3 - \mathbf{r}_4) \\
&\quad + \langle c \rangle^2 \delta(\mathbf{r}_1 - \mathbf{r}_2) \delta(\mathbf{r}_3 - \mathbf{r}_4)
\end{aligned} \tag{B.16}$$

Let us now focus on the autocorrelation of the intensity fluctuations by using equation B.16 for the simplification to yield

$$\begin{aligned}
\langle \delta I_q(t + \tau) \delta I_q(t) \rangle &= \langle I_q(t + \tau) I_q(t) \rangle - \langle I_q(t) \rangle^2 \\
&= |\chi_s^{(q)}|^4 \iiint \left[\frac{\langle c \rangle^3}{(4\pi D\tau)^{3/2}} \exp\left(-\frac{\|\mathbf{r}_1 - \mathbf{r}_3 + \mathbf{V}\tau\|^2}{4D\tau}\right) + \frac{\langle c \rangle^3}{(4\pi D\tau)^{3/2}} \exp\left(-\frac{\|\mathbf{r}_1 - \mathbf{r}_4 + \mathbf{V}\tau\|^2}{4D\tau}\right) \right. \\
&\quad + \frac{\langle c \rangle^3}{(4\pi D\tau)^{3/2}} \exp\left(-\frac{\|\mathbf{r}_2 - \mathbf{r}_3 + \mathbf{V}\tau\|^2}{4D\tau}\right) + \frac{\langle c \rangle^3}{(4\pi D\tau)^{3/2}} \exp\left(-\frac{\|\mathbf{r}_2 - \mathbf{r}_4 + \mathbf{V}\tau\|^2}{4D\tau}\right) \\
&\quad + \frac{\langle c \rangle^2 \delta(\mathbf{r}_1 - \mathbf{r}_2)}{(4\pi D\tau)^{3/2}} \exp\left(-\frac{\|\mathbf{r}_1 - \mathbf{r}_3 + \mathbf{V}\tau\|^2}{4D\tau}\right) + \frac{\langle c \rangle^2 \delta(\mathbf{r}_1 - \mathbf{r}_2)}{(4\pi D\tau)^{3/2}} \exp\left(-\frac{\|\mathbf{r}_1 - \mathbf{r}_4 + \mathbf{V}\tau\|^2}{4D\tau}\right) \\
&\quad + \frac{\langle c \rangle^2 \delta(\mathbf{r}_3 - \mathbf{r}_4)}{(4\pi D\tau)^{3/2}} \exp\left(-\frac{\|\mathbf{r}_1 - \mathbf{r}_3 + \mathbf{V}\tau\|^2}{4D\tau}\right) + \frac{\langle c \rangle^2 \delta(\mathbf{r}_3 - \mathbf{r}_4)}{(4\pi D\tau)^{3/2}} \exp\left(-\frac{\|\mathbf{r}_2 - \mathbf{r}_3 + \mathbf{V}\tau\|^2}{4D\tau}\right) \\
&\quad + \frac{\langle c \rangle \delta(\mathbf{r}_1 - \mathbf{r}_2) \delta(\mathbf{r}_3 - \mathbf{r}_4)}{(4\pi D\tau)^{3/2}} \exp\left(-\frac{\|\mathbf{r}_1 - \mathbf{r}_3 + \mathbf{V}\tau\|^2}{4D\tau}\right) \\
&\quad + \frac{\langle c \rangle^2}{64\pi^3 D^3 \tau^3} \exp\left(-\frac{\|\mathbf{r}_1 - \mathbf{r}_3 + \mathbf{V}\tau\|^2}{4D\tau}\right) \exp\left(-\frac{\|\mathbf{r}_2 - \mathbf{r}_4 + \mathbf{V}\tau\|^2}{4D\tau}\right) \\
&\quad \left. + \frac{\langle c \rangle^2}{64\pi^3 D^3 \tau^3} \exp\left(-\frac{\|\mathbf{r}_1 - \mathbf{r}_4 + \mathbf{V}\tau\|^2}{4D\tau}\right) \exp\left(-\frac{\|\mathbf{r}_2 - \mathbf{r}_3 + \mathbf{V}\tau\|^2}{4D\tau}\right) \right] \\
&\quad \prod_{i=1}^4 A_q^*(\mathbf{r}_i) \cos(\kappa_q z_i) dV_i \\
&= |\chi_s^{(q)}|^4 \iiint \left[\frac{\langle c \rangle^3}{2(\pi D\tau)^{3/2}} \exp\left(-\frac{\|\mathbf{r}_1 - \mathbf{r}_3 + \mathbf{V}\tau\|^2}{4D\tau}\right) + \frac{\langle c \rangle^2 \delta(\mathbf{r}_1 - \mathbf{r}_2)}{2(\pi D\tau)^{3/2}} \exp\left(-\frac{\|\mathbf{r}_1 - \mathbf{r}_3 + \mathbf{V}\tau\|^2}{4D\tau}\right) \right. \\
&\quad + \frac{\langle c \rangle \delta(\mathbf{r}_1 - \mathbf{r}_2) \delta(\mathbf{r}_3 - \mathbf{r}_4)}{(4\pi D\tau)^{3/2}} \exp\left(-\frac{\|\mathbf{r}_1 - \mathbf{r}_3 + \mathbf{V}\tau\|^2}{4D\tau}\right) \\
&\quad \left. + \frac{\langle c \rangle^2}{32\pi^3 D^3 \tau^3} \exp\left(-\frac{\|\mathbf{r}_1 - \mathbf{r}_4 + \mathbf{V}\tau\|^2}{4D\tau}\right) \exp\left(-\frac{\|\mathbf{r}_2 - \mathbf{r}_3 + \mathbf{V}\tau\|^2}{4D\tau}\right) \right] \\
&\quad \prod_{i=1}^4 A_q^*(\mathbf{r}_i) \cos(\kappa_q z_i) dV_i \\
&= g_1(\tau) + g_2(\tau) + g_3(\tau) + g_4(\tau)
\end{aligned} \tag{B.17}$$

All what remains is the integration of these respective terms. This step is really lengthy in notation since it is a twelve-fold integration for each of these four terms corresponding to four different space variables in three directions. It is best resolved by computer assisted simplification using a tool such as Mathematica. The calculation is best started with the integrations in z for most compact results. For the interested reader, the Mathematica-notebooks of the calculation can be found on the EPFL infoscience server [183].

B.1 Solution for pure diffusion ($V=0$)

As a result for this particular case, we find the following

$$\begin{aligned}
 g_1(\tau) &= \frac{A_{0,q}^4 \left| \chi_s^{(q)} \right|^4 \langle c \rangle^3 \pi^{9/2} w_0^6 z_0^3 \left[\exp\left(-\frac{z_0^2 \kappa_q^2}{q}\right) + \exp\left(-\frac{z_0^2 \kappa_q^2 (z_0^2 + 4Dq\tau)}{2q(z_0^2 + 2Dq\tau)}\right) \right]}{\sqrt{2} q^{9/2} \left(\frac{2Dq\tau}{w_0^2} + 1 \right) \sqrt{\frac{2qD\tau}{z_0^2} + 1}} \\
 &= \frac{A_{0,q}^4 \left| \chi_s^{(q)} \right|^4 \langle c \rangle^3 \pi^{9/2} w_{0,q}^6 z_{0,q}^3 \left[\exp\left(-z_{0,q}^2 \kappa_q^2\right) + \exp\left(-\frac{z_{0,q}^2 \kappa_q^2 (4D\tau/z_{0,q}^2 + 1)}{2(2D\tau/z_{0,q}^2 + 1)}\right) \right]}{\left(\frac{2D\tau}{w_{0,q}^2} + 1 \right) \sqrt{\frac{4D\tau}{z_{0,q}^2} + 2}} \\
 &= \frac{A_{0,q}^4 \left| \chi_s^{(q)} \right|^4 N^3 \left[\exp\left(-z_{0,q}^2 \kappa_q^2\right) + \exp\left(-\frac{z_{0,q}^2 \kappa_q^2 (4D\tau/z_{0,q}^2 + 1)}{2(2D\tau/z_{0,q}^2 + 1)}\right) \right]}{\left(\frac{2D\tau}{w_{0,q}^2} + 1 \right) \sqrt{\frac{4D\tau}{z_{0,q}^2} + 2}}
 \end{aligned} \tag{B.18}$$

Where we have defined $z_{0,q} = z_0/\sqrt{q}$ and similarly $w_{0,q} = w_0/\sqrt{q}$ and further we have defined $N = \langle c \rangle \pi^{3/2} \omega_0^2 z_0/q^{3/2} = \langle c \rangle \pi^{3/2} \omega_{0,q}^2 z_{0,q}$

$$\begin{aligned}
 g_2(\tau) &= \frac{A_{0,q}^4 \left| \chi_s^{(q)} \right|^4 \langle c \rangle^2 \pi^3 w_0^4 z_0^2 \left[\exp\left(-\frac{z_0^2 \kappa_q^2}{q}\right) + \exp\left(-\frac{z_0^2 \kappa_q^2 (8Dq\tau + z_0^2)}{q(8Dq\tau + 3z_0^2)}\right) + 2 \exp\left(-\frac{z_0^2 \kappa_q^2 (4Dq\tau + z_0^2)}{q(8Dq\tau + 3z_0^2)}\right) \right]}{q^3 \left(\frac{8Dq\tau}{w_0^2} + 3 \right) \sqrt{\frac{8Dq\tau}{z_0^2} + 3}} \\
 &= \frac{A_{0,q}^4 \left| \chi_s^{(q)} \right|^4 N^2 \left[\exp\left(-z_{0,q}^2 \kappa_q^2\right) + \exp\left(-\frac{z_{0,q}^2 \kappa_q^2 (8D\tau/z_{0,q}^2 + 1)}{8D\tau/z_{0,q}^2 + 3}\right) + 2 \exp\left(-\frac{z_{0,q}^2 \kappa_q^2 (4D\tau/z_{0,q}^2 + 1)}{8D\tau/z_{0,q}^2 + 3}\right) \right]}{\left(\frac{8D\tau}{w_{0,q}^2} + 3 \right) \sqrt{\frac{8D\tau}{z_{0,q}^2} + 3}}
 \end{aligned} \tag{B.19}$$

$$\begin{aligned}
 g_3(\tau) &= \frac{A_{0,q}^4 \left| \chi_s^{(q)} \right|^4 \langle c \rangle \pi^{3/2} w_0^2 z_0 \left[4 \exp\left(-\frac{z_0^2 \kappa_q^2 (8Dq\tau/z_0^2 + 1)}{4q(4Dq\tau/z_0^2 + 1)}\right) + 2 + \exp\left(-\frac{z_0^2 \kappa_q^2}{q}\right) + \exp\left(-\frac{4D\kappa_q^2 \tau}{4Dq\tau/z_0^2 + 1}\right) \right]}{64 q^{3/2} \left(\frac{4Dq\tau}{w_0^2} + 1 \right) \sqrt{\frac{4Dq\tau}{z_0^2} + 1}} \\
 &= \frac{A_{0,q}^4 \left| \chi_s^{(q)} \right|^4 N \left[4 \exp\left(-\frac{z_{0,q}^2 \kappa_q^2 (8D\tau/z_{0,q}^2 + 1)}{4(4D\tau/z_{0,q}^2 + 1)}\right) + 2 + \exp\left(-z_{0,q}^2 \kappa_q^2\right) + \exp\left(-\frac{4D\kappa_q^2 \tau}{4D\tau/z_{0,q}^2 + 1}\right) \right]}{64 \left(\frac{4D\tau}{w_{0,q}^2} + 1 \right) \sqrt{\frac{4D\tau}{z_{0,q}^2} + 1}}
 \end{aligned} \tag{B.20}$$

$$\begin{aligned}
 g_4(\tau) &= \frac{A_{0,q}^4 \left| \chi_s^{(q)} \right|^4 \langle c \rangle^2 \pi^3 w_0^4 z_0^2 \left[\exp\left(-\frac{z_0^2 \kappa_q^2}{q}\right) + 2 \exp\left(-\frac{z_0^2 \kappa_q^2 (4Dq\tau + z_0^2)}{2q(2Dq\tau + z_0^2)}\right) + \exp\left(-\frac{2Dz_0^2 \kappa_q^2 \tau}{2Dq\tau + z_0^2}\right) \right]}{16q^3 \left(\frac{2Dq\tau}{w_{0,q}^2} + 1 \right)^2 \left(\frac{2Dq\tau}{z_0^2} + 1 \right)} \\
 &= \frac{A_{0,q}^4 \left| \chi_s^{(q)} \right|^4 N^2 \left[\exp\left(-z_{0,q}^2 \kappa_q^2\right) + 2 \exp\left(-\frac{z_{0,q}^2 \kappa_q^2 (4D\tau/z_{0,q}^2 + 1)}{2(2D\tau/z_{0,q}^2 + 1)}\right) + \exp\left(-\frac{2D\kappa_q^2 \tau}{2D\tau/z_{0,q}^2 + 1}\right) \right]}{16 \left(\frac{2D\tau}{w_{0,q}^2} + 1 \right)^2 \left(\frac{2D\tau}{z_{0,q}^2} + 1 \right)}
 \end{aligned} \tag{B.21}$$

The mean intensity is best calculated with equation B.7 to yield

$$\begin{aligned}
 \langle I_q(t) \rangle &= \frac{A_{0,q}^2 \left| \chi_s^{(q)} \right|^2 \langle c \rangle \pi^{3/2} w_0^2 z_0 \left[\sqrt{2} \left(1 + \exp\left(-\frac{z_0^2 \kappa_q^2}{2q}\right) \right) q^{3/2} + \exp\left(-\frac{z_0^2 \kappa_q^2}{2q}\right) 8 \langle c \rangle \pi^{3/2} w_0^2 z_0 \right]}{8q^3} \\
 &= \frac{1}{8} A_{0,q}^2 \left| \chi_s^{(q)} \right|^2 \langle c \rangle \pi^{3/2} w_{0,q}^2 z_{0,q} \left[\sqrt{2} \left(1 + \exp\left(-z_{0,q}^2 \kappa_q^2 / 2\right) \right) + \exp\left(-z_{0,q}^2 \kappa_q^2 / 2\right) 8 \langle c \rangle \pi^{3/2} w_{0,q}^2 z_{0,q} \right] \\
 &= \frac{1}{8} A_{0,q}^2 \left| \chi_s^{(q)} \right|^2 N \left[\sqrt{2} \left(1 + \exp\left(-z_{0,q}^2 \kappa_q^2 / 2\right) \right) + 8N \exp\left(-z_{0,q}^2 \kappa_q^2 / 2\right) \right]
 \end{aligned} \tag{B.22}$$

The final step is to combine all the intermediate results to yield the normalized autocorrelation of the q th harmonic generation intensity

$$\begin{aligned}
 G(\tau) &= \frac{\langle \delta I_q(t + \tau) \delta I_q(t) \rangle}{\langle I_q(t) \rangle^2} \\
 &= \frac{g_1(\tau) + g_2(\tau) + g_3(\tau) + g_4(\tau)}{\langle I_q(t) \rangle^2} \\
 &= \frac{G_1(\tau) + G_2(\tau) + G_3(\tau) + G_4(\tau)}{G_m(\tau)}
 \end{aligned} \tag{B.23}$$

where we define for more compact notation $G_x(\tau) = g_x(\tau) / \left(A_{0,q}^2 \left| \chi_s^{(q)} \right|^2 N \right)^2$

$$\begin{aligned}
 G_1(\tau) &= N \frac{\left[\exp\left(-z_{0,q}^2 \kappa_q^2\right) + \exp\left(-\frac{z_{0,q}^2 \kappa_q^2 (4D\tau/z_{0,q}^2 + 1)}{2(2D\tau/z_{0,q}^2 + 1)}\right) \right]}{\left(\frac{2D\tau}{w_{0,q}^2} + 1 \right) \sqrt{\frac{4D\tau}{z_{0,q}^2} + 2}} \\
 G_2(\tau) &= \frac{\left[\exp\left(-z_{0,q}^2 \kappa_q^2\right) + \exp\left(-\frac{z_{0,q}^2 \kappa_q^2 (8D\tau/z_{0,q}^2 + 1)}{8D\tau/z_{0,q}^2 + 3}\right) + 2 \exp\left(-\frac{z_{0,q}^2 \kappa_q^2 (4D\tau/z_{0,q}^2 + 1)}{8D\tau/z_{0,q}^2 + 3}\right) \right]}{\left(\frac{8D\tau}{w_{0,q}^2} + 3 \right) \sqrt{\frac{8D\tau}{z_{0,q}^2} + 3}} \\
 G_3(\tau) &= \frac{1}{N} \frac{\left[4 \exp\left(-\frac{z_{0,q}^2 \kappa_q^2 (8D\tau/z_{0,q}^2 + 1)}{4(4D\tau/z_{0,q}^2 + 1)}\right) + 2 + \exp\left(-z_{0,q}^2 \kappa_q^2\right) + \exp\left(-\frac{4D\kappa_q^2 \tau}{4D\tau/z_{0,q}^2 + 1}\right) \right]}{64 \left(\frac{4D\tau}{w_{0,q}^2} + 1 \right) \sqrt{\frac{4D\tau}{z_{0,q}^2} + 1}} \\
 G_4(\tau) &= \frac{\left[\exp\left(-z_{0,q}^2 \kappa_q^2\right) + 2 \exp\left(-\frac{z_{0,q}^2 \kappa_q^2 (4D\tau/z_{0,q}^2 + 1)}{2(2D\tau/z_{0,q}^2 + 1)}\right) + \exp\left(-\frac{2D\kappa_q^2 \tau}{2D\tau/z_{0,q}^2 + 1}\right) \right]}{16 \left(\frac{2D\tau}{w_{0,q}^2} + 1 \right)^2 \left(\frac{2D\tau}{z_{0,q}^2} + 1 \right)} \\
 G_m(\tau) &= \frac{1}{64} \left[\sqrt{2} \left(1 + \exp\left(-z_{0,q}^2 \kappa_q^2 / 2\right) \right) + 8N \exp\left(-z_{0,q}^2 \kappa_q^2 / 2\right) \right]^2
 \end{aligned} \tag{B.24}$$

Appendix B. Nonlinear correlation spectroscopy - Autocorrelation theory

For even more compact notation, let us define the lateral diffusion time as $\tau_{D,q} = \omega_{0,q}^2/(4D)$ and further let us define a structural parameter $S_q = z_{0,q}/\omega_{0,q}$, hence it follows that $z_{0,q}^2/(4D) = S_q^2 \tau_{D,q}$. Hence we identify

$$\begin{aligned}
 G_1(\tau) &= N \frac{\left[\exp\left(-z_{0,q}^2 \kappa_q^2\right) + \exp\left(-\frac{z_{0,q}^2 \kappa_q^2 (\tau/(S_q^2 \tau_{D,q})+1)}{(\tau/(S_q^2 \tau_{D,q})+2)}\right) \right]}{\left(\frac{\tau}{2\tau_{D,q}} + 1\right) \sqrt{\frac{\tau}{S_q^2 \tau_{D,q}} + 2}} \\
 G_2(\tau) &= \frac{\left[\exp\left(-z_{0,q}^2 \kappa_q^2\right) + \exp\left(-\frac{z_{0,q}^2 \kappa_q^2 (2\tau/(S_q^2 \tau_{D,q})+1)}{2\tau/(S_q^2 \tau_{D,q})+3}\right) + 2 \exp\left(-\frac{z_{0,q}^2 \kappa_q^2 (\tau/(S_q^2 \tau_{D,q})+1)}{2\tau/(S_q^2 \tau_{D,q})+3}\right) \right]}{\left(\frac{2\tau}{\tau_{D,q}} + 3\right) \sqrt{\frac{2\tau}{S_q^2 \tau_{D,q}} + 3}} \\
 G_3(\tau) &= \frac{1}{N} \frac{\left[4 \exp\left(-\frac{z_{0,q}^2 \kappa_q^2 (2\tau/(S_q^2 \tau_{D,q})+1)}{4(\tau/(S_q^2 \tau_{D,q})+1)}\right) + 2 + \exp\left(-z_{0,q}^2 \kappa_q^2\right) + \exp\left(-\frac{z_{0,q}^2 \kappa_q^2 \tau/(S_q^2 \tau_{D,q})}{\tau/(S_q^2 \tau_{D,q})+1}\right) \right]}{64 \left(\frac{\tau}{\tau_{D,q}} + 1\right) \sqrt{\frac{\tau}{S_q^2 \tau_{D,q}} + 1}} \\
 G_4(\tau) &= \frac{\left[\exp\left(-z_{0,q}^2 \kappa_q^2\right) + 2 \exp\left(-\frac{z_{0,q}^2 \kappa_q^2 (\tau/(S_q^2 \tau_{D,q})+1)}{\tau/(S_q^2 \tau_{D,q})+2}\right) + \exp\left(-\frac{z_{0,q}^2 \kappa_q^2 \tau/(2S_q^2 \tau_{D,q})}{\tau/(2S_q^2 \tau_{D,q})+1}\right) \right]}{16 \left(\frac{\tau}{2\tau_{D,q}} + 1\right)^2 \left(\frac{\tau}{2S_q^2 \tau_{D,q}} + 1\right)} \\
 G_m(\tau) &= \frac{1}{64} \left[\sqrt{2} \left(1 + \exp\left(-z_{0,q}^2 \kappa_q^2/2\right)\right) + 8N \exp\left(-z_{0,q}^2 \kappa_q^2/2\right) \right]^2
 \end{aligned} \tag{B.25}$$

In order to write this more compact let us define

$$\begin{aligned}
 H_1 &= \exp\left(-z_{0,q}^2 \kappa_q^2\right) \\
 H_2(\tau, a, b, c, d) &= \exp\left(-\frac{z_{0,q}^2 \kappa_q^2 (a\tau/(S_q^2 \tau_{D,q}) + b)}{c\tau/(S_q^2 \tau_{D,q}) + d}\right)
 \end{aligned} \tag{B.26}$$

It follows hence for the solutions without flow

$$\begin{aligned}
 G_1(\tau) &= N \frac{[H_1 + H_2(\tau, 1, 1, 1, 2)]}{\left(\frac{\tau}{2\tau_{D,q}} + 1\right) \sqrt{\frac{\tau}{S_q^2 \tau_{D,q}} + 2}} \\
 G_2(\tau) &= \frac{[H_1 + H_2(\tau, 2, 1, 2, 3) + 2H_2(\tau, 1, 1, 2, 3)]}{\left(\frac{2\tau}{\tau_{D,q}} + 3\right) \sqrt{\frac{2\tau}{S_q^2 \tau_{D,q}} + 3}} \\
 G_3(\tau) &= \frac{1}{N} \frac{[2 + H_1 + 4H_2(\tau, 2, 1, 4, 4) + H_2(\tau, 1, 0, 1, 1)]}{64 \left(\frac{\tau}{\tau_{D,q}} + 1\right) \sqrt{\frac{\tau}{S_q^2 \tau_{D,q}} + 1}} \\
 G_4(\tau) &= \frac{[H_1 + 2H_2(\tau, 1, 1, 1, 2) + H_2(\tau, 0.5, 0, 0.5, 1)]}{16 \left(\frac{\tau}{2\tau_{D,q}} + 1\right)^2 \left(\frac{\tau}{2S_q^2 \tau_{D,q}} + 1\right)} \\
 G_m(\tau) &= \frac{1}{64} \left[\sqrt{2} \left(1 + \sqrt{H_1}\right) + 8N \sqrt{H_1} \right]^2
 \end{aligned} \tag{B.27}$$

B.2 Solution for diffusion with flow ($V \neq 0$)

Let us now find the solution for the case with an additional flow component (uniform translation). We have split the flow velocity into lateral and axial flow components. In order to keep the result as compact as possible, we apply directly the same simplifications as before: $z_{0,q} = z_0/\sqrt{q}$ and similarly $\omega_{0,q} = \omega_0/\sqrt{q}$, and the number of molecules in the volume

$N = \langle c \rangle \pi^{3/2} \omega_0^2 z_0 / q^{3/2}$, the lateral diffusion time $\tau_{D,q} = \omega_{0,q}^2 / (4D)$, a structural parameter $S_q = z_{0,q} / \omega_{0,q}$. Further on we define $\tau_{fr} = \omega_0 / \nu_r$ for the lateral transition time across the focal spot and similarly $\tau_{fz} = z_0 / \nu_z$ for the axial transition time.

The complete derivation can be found in the form of a Mathematica notebook on the EPFL infoscience server [183]. As a result we find

$$G_f(\tau) = \frac{G_{f,1}(\tau) + G_{f,2}(\tau) + G_{f,3}(\tau) + G_{f,4}(\tau)}{G_{f,m}(\tau)} \quad (\text{B.28})$$

where

$$G_{f,m}(\tau) = G_m(\tau) \quad (\text{B.29})$$

and

$$\begin{aligned} G_{f,1}(\tau) = & \frac{1}{(\tau + 2\tau_{D,q}) \sqrt{z_{0,q}^2 \left(\frac{\tau}{S_q^2 \tau_{D,q}} + 2 \right)}} 2N \tau_{D,q} z_{0,q} \\ & \left(\exp \left(q \tau^2 \tau_{D,q} \left(-\frac{S_q^2}{\tau_{fz}^2 (2S_q^2 \tau_{D,q} + \tau)} - \frac{1}{\tau_{fr}^2 (\tau + 2\tau_{D,q})} \right) - \kappa^2 z_{0,q}^2 \right) \right. \\ & + \cos \left(\frac{2\kappa \sqrt{q} S_q^2 \tau \tau_{D,q} z_{0,q}}{2S_q^2 \tau_{D,q} \tau_{fz} + \tau \tau_{fz}} \right) \exp \left(q \tau^2 \tau_{D,q} \left(-\frac{S_q^2}{\tau_{fz}^2 (2S_q^2 \tau_{D,q} + \tau)} - \frac{1}{\tau_{fr}^2 (\tau + 2\tau_{D,q})} \right) \right. \\ & \left. \left. - \frac{\kappa^2 z_{0,q}^2 (S_q^2 \tau_{D,q} + \tau)}{2S_q^2 \tau_{D,q} + \tau} \right) \right) \end{aligned} \quad (\text{B.30})$$

The other terms $G_{f,2}(\tau)$, $G_{f,3}(\tau)$ and $G_{f,4}(\tau)$ are even more complex. Due to this, the truly interested reader is referred to the Mathematica notebook that can be found on the EPFL infoscience server [183].

A common feature to all the terms is the expression with the cosinus, leading to oscillations of the resulting autocorrelation curve. This is a particularity of this flow-model that has no similar counterpart in FCS. It stems from the coherent nature of the emitted light, and in particular from the linear phase factor that we have introduced in the model.

C Colormaps (Lookup-tables)

The display of data is an important task that concerns most scientists. A colormap describes the mapping between a data-value and the output (any shade of color or black & white). In particular for the presentation of images that contain several dimensions of information, the design of adequate colormaps (or lookup-tables) is a very important aspect of the data processing and display. During this thesis, several colormaps have been designed. Two common problems with the existing colormaps have been identified: the fact that only very few of them are designed for being printed on color-printers and that almost no existing colormap is designed to be viewed without distortions by persons with a color vision deficiency.

When using traditional printers, the range of available colors is typically reduced to the CMYK-colorspace, which is based on a subtractive color model, which reflects the fact that paper can only be made darker with the addition of ink (addition of 100% of each color component will result in black). This colorspace is fundamentally less broad than the RGB-colorspace (used for screens and projectors) which is an additive color model (addition of 100% of each component results in white). As a result, in the CMYK-colorspace all colors that are achieved by mixtures of its basic components (such as green, orange but also the basic components of the RGB colorspace such as blue and red) are difficult to be reproduced in the same way as on screen. Unfortunately many of the common employed colormaps neglect this aspect and are designed only to "look good on the screen".

Further on, color vision deficiency is a very common problem of our population which affects 8 to 10% of adult caucasian men [184] and 0.4 to 0.5% of adult women. In my personal opinion any colormap employed to display scientific data should ideally be designed in such a way that persons with a color vision problem are able to view and perceive the true data and not being mislead by anything which they are not being able to see. The most common deficiency is a red-green deficiency (Deuteranomaly and Protanomaly) which affects between 8 to 10% of adult men [184]. There exists also a very rare blue-yellow colorblindness (Tritanomaly) affecting some 0.2% of people[185]. Taking into account all different diseases would limit the

Appendix C. Colormaps (Lookup-tables)

display to black and white images, however its obvious that completely omitting any colors does not allow any multi-dimensional display of information, which is a too severe limitation especially in our case with the lifetime images. We have settled hence for a compromise that neglects the rare form of Tritanomaly.

The design of the colormap is done in such a way that people without red-green color vision will perceive the colormap as a linear ramp between blue and yellow, which is perfect for their vision. However in order to employ the richness of colors available to the vast majority of people, the colormap is not only limiting itself to these colors. It is just avoiding colors that would result in a nonlinear color-ramp to persons with red-green color deficiencies.

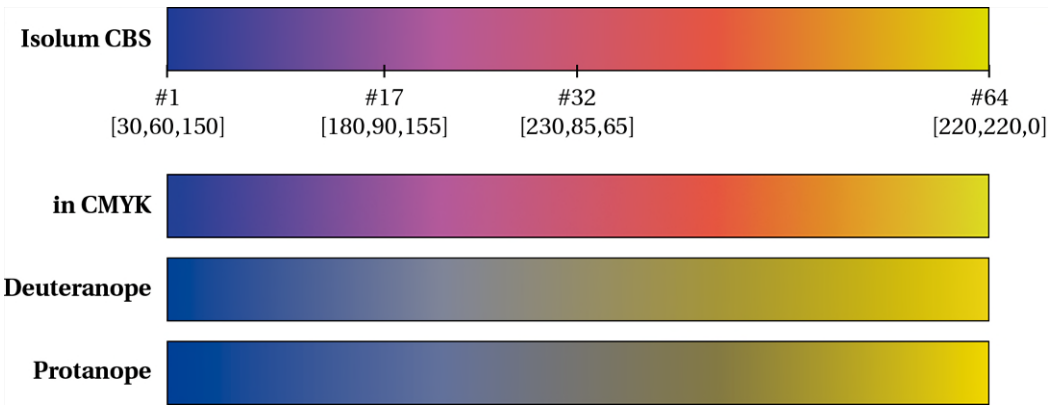


Figure C.1: Isoluminescence ("color-blind-safe"), a colormap design with improved printing capabilities that is more adapted for red-green color vision deficiencies. The values in the square brackets are the RGB-values for the colors at the respective index positions in the map. The lower two lines are simulations of how the colormap would look like to a person with red-green color vision deficiency (Deuteranope and Protanope). The simulation of the color vision deficiency has been done by www.vischeck.com.

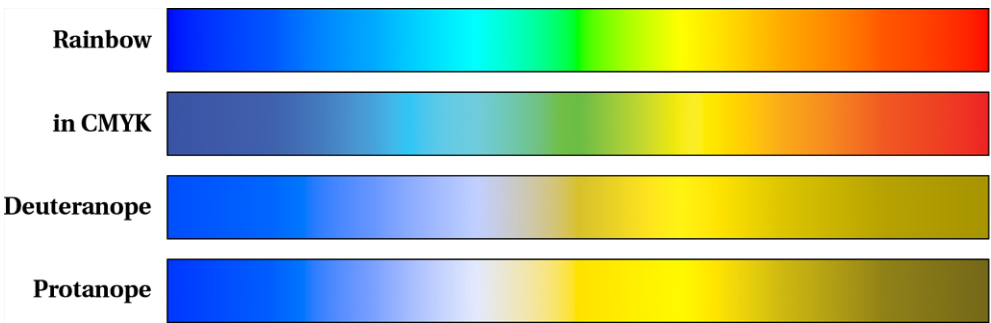


Figure C.2: Rainbow, a colormap design incorporating the full visible spectrum. As expected, when printing this vast range of colors, there will be severe losses. Additionally color vision deficient people will experience difficulties to distinguish data belonging to values which should be "green" versus data that should be "orange" (they will actually see a kind of local maximum around yellow, preventing the distinction between what is left or right of this maximum).

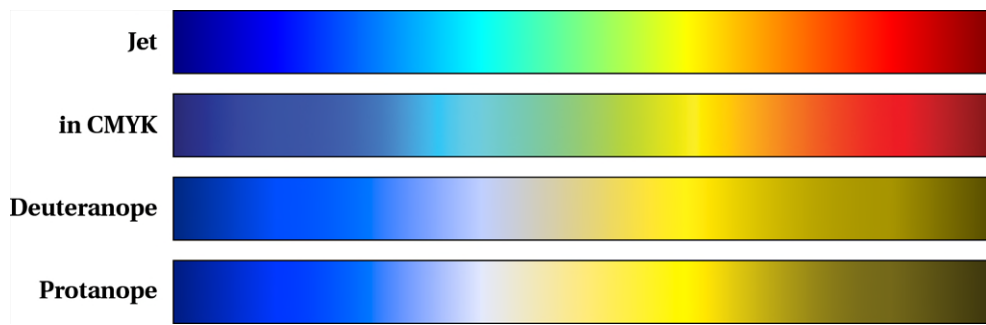


Figure C.3: Jet, the default colormap in Matlab. Not only this colormap does not print very well, it also includes ambiguous colors for people with red-green color vision deficiencies.

All these colormaps are designed for the use with one or more additional channels of information. For the case of lifetime related data this could be the fluorescence intensity being encoded as a transparency map of the respective color and an additional phase-contrast image being encoded in black and white as background.

An additional application for colormaps is a display of a single channel of information. Usually a simple black to white ramp is sufficient to display such data. However, colors can help to emphasize the subtle transitions between the different shades of gray. Two very common maps for this purpose are "hot" in matlab as well as "fire" in ImageJ. We have taken the later and improved it for printing purposes. The resulting colormap can be seen in figure C.4.

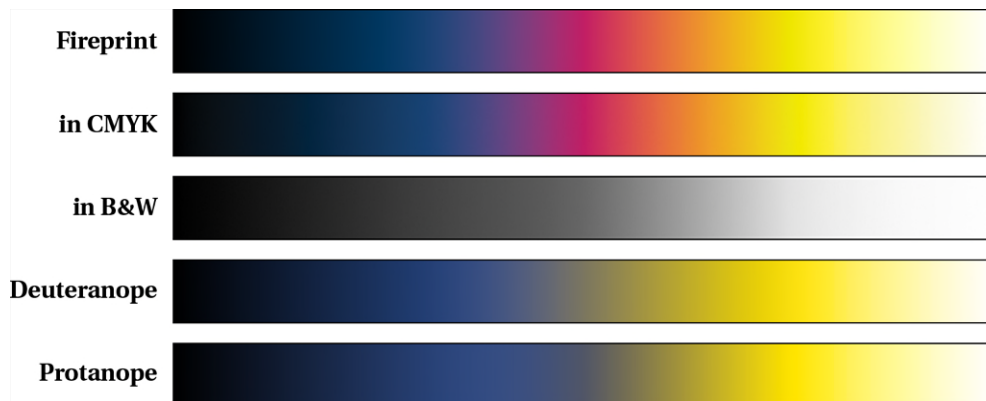


Figure C.4: Fire (optimized for printing), a colormap that helps to emphasize one-dimensional data and prints well not only on colorprinters but also in black and white.

Both of these optimized colormaps ("fireprint" as well as "isolum_cbs") are available for download on the Mathworks MATLAB Central File exchange (www.mathworks.com/matlabcentral/fileexchange/), with the following file numbers 31761 and 31762).

Bibliography

- [1] S. L. Shorte and F. Frischknecht. Imaging cellular and molecular biological functions. Springer-Verlag Berlin Heidelberg, 2007.
- [2] E. Abbe. Beiträge zur Theorie des Mikroskops und der mikroskopischen Wahrnehmung. *Archiv für mikroskopische Anatomie*, 1873.
- [3] A. Diaspro. Nanoscopy and multidimensional optical fluorescence microscopy. CRC Press, Taylor & Francis Group, 2010.
- [4] R. Heintzmann and G. Ficz. Breaking the resolution limit in light microscopy. *Briefings in functional genomics & proteomics*, 5(4):289–301, 2006.
- [5] L. Schermelleh, R. Heintzmann, and H. Leonhardt. A guide to super-resolution fluorescence microscopy. *Journal of Cell Biology*, 190(2):165–175, 2010.
- [6] R. Schmidt, C. A. Wurm, S. Jakobs, J. Engelhardt, A. Egner, and S. W. Hell. Spherical nanosized focal spot unravels the interior of cells. *Nature Methods*, 5(6):539–544, 2008.
- [7] S. W. Hell and J. Wichmann. Breaking the diffraction resolution limit by stimulated emission: stimulated-emission-depletion fluorescence microscopy. *Optics Letters*, 19(11):780–782, 1994.
- [8] S. W. Hell. Toward fluorescence nanoscopy. *Nature Biotechnology*, 21(11):1347–1355, 2003.
- [9] S. W. Hell, R. Schmidt, and A. Egner. Diffraction-unlimited three-dimensional optical nanoscopy with opposing lenses. *Nature Photonics*, 3(7):381, 2009.
- [10] M. Rust, M. Bates, and X. Zhuang. Sub-diffraction-limit imaging by stochastic optical reconstruction microscopy (STORM). *Nature Methods*, 2006.
- [11] S. T. Hess, T. P. K. Girirajan, and M. D. Mason. Ultra-High Resolution Imaging by Fluorescence Photoactivation Localization Microscopy. *Biophysical Journal*, 91(11):4258–4272, 2006.

Bibliography

- [12] T. Dertinger, R. Colyera, G. Iyer, S. Weiss, and J. Enderlein. Fast, background-free, 3D super-resolution optical fluctuation imaging (SOFI). *Proceedings of the National Academy of Sciences of the United States of America*, 106(52):22287–22292, 2009.
- [13] S. Hell. Fundamental improvement of resolution with a 4Pi-confocal fluorescence microscope using two-photon excitation. *Optics Communications*, 93(5-6):277–282, 1992.
- [14] Gustafsson, Agard, and Sedat. I5M: 3D widefield light microscopy with better than 100 nm axial resolution. *Journal of Microscopy*, 195(1):10–16, 1999.
- [15] M. A. A. Neil, R. Juskaitis, and T. Wilson. Method of obtaining optical sectioning by using structured light in a conventional microscope. *Optics Letters*, 22(24):1905, 1997.
- [16] M. G. L. Gustafsson. Surpassing the lateral resolution limit by a factor of two using structured illumination microscopy. *Journal of Microscopy*, 198(2):82–87, 2000.
- [17] G. Cragg and P. So. Lateral resolution enhancement with standing evanescent waves. *Optics Letters*, 25(1):46–48, 2000.
- [18] H. J. T. Frohn and A. Stemmer. True optical resolution beyond the Rayleigh limit achieved by standing wave illumination. *Proceedings of the National Academy of Sciences*, 97(13):7232–7236, 2000.
- [19] J. Frohn, H. Knapp, and A. Stemmer. Three-dimensional resolution enhancement in fluorescence microscopy by harmonic excitation. *Optics Letters*, 26(11):828–830, 2001.
- [20] R. Heintzmann and M. G. L. Gustafsson. Subdiffraction resolution in continuous samples. *Nature Photonics*, 3(7):362, 2009.
- [21] E. Johnsen and O. Shimomura. Preparation and use of aequorin for rapid microdetermination of Ca^{2+} in biological systems. *Nature: New biology*, 237(78):287–288, 1972.
- [22] V. Romoser, P. Hinkle, and A. Persechini. Detection in living cells of Ca^{2+} -dependent changes in the fluorescence emission of an indicator composed of two green fluorescent protein variants linked by a calmodulin-binding sequence. A new class of fluorescent indicators. *Journal of Biological Chemistry*, 272(20):13270–13274, 1997.
- [23] N. Pavillon, A. Benke, D. Boss, C. Moratal, J. Kühn, P. Jourdain, C. Depeursinge, P. Magistretti, and P. Marquet. Cell morphology and intracellular ionic homeostasis explored with a multimodal approach combining epifluorescence and digital holographic microscopy. *Journal of Biophotonics*, 3(7):432–436, 2010.
- [24] W. Rumsey, J. Vanderkooi, and D. Wilson. Imaging of phosphorescence: A novel method for measuring oxygen distribution in perfused tissue. *Science*, 241(4873):1649–1651, 1988.

-
- [25] M. C. Hogan. Phosphorescence quenching method for measurement of intracellular PO₂ in isolated skeletal muscle fibers. *Journal of Applied Physiology*, 86(2):720–724, 1999.
- [26] A. Raabe, D. V. D. Ville, M. Leutenegger, A. Szelényi, E. Hattingen, R. Gerlach, V. Seifert, C. Hauger, A. Lopez, R. Leitgeb, M. Unser, E. Martin-Williams, and T. Lasser. Laser Doppler imaging for intraoperative human brain mapping. *NeuroImage*, 44(4):1284–1289, 2009.
- [27] A. Serov and T. Lasser. High-speed laser Doppler perfusion imaging using an integrating CMOS image sensor. *Optics Express*, 13(17):6416–6428, 2005.
- [28] B. Grajciar, M. Pircher, A. Fercher, and R. Leitgeb. Parallel Fourier domain optical coherence tomography for in vivo measurement of the human eye. *Optics Express*, 13(4):1131–1137, 2005.
- [29] G. Koenderink, Z. Dogic, F. Nakamura, P. Bendix, F. MacKintosh, J. Hartwig, T. Stossel, and D. Weitz. An active biopolymer network controlled by molecular motors. *Proceedings of the National Academy of Sciences of the United States of America*, 106(36):15192–15197, 2009.
- [30] C. Plathow and W. Weber. Tumor cell metabolism imaging. *Journal of Nuclear Medicine*, 49(SUPPL.6):43S–63S, 2008.
- [31] D. Magde, E. Elson, and W. Webb. Thermodynamic fluctuations in a reacting system measurement by fluorescence correlation spectroscopy. *Physical Review Letters*, 29(11):705–708, 1972.
- [32] R. Rigler, U. Mets, J. Widengren, and P. Kask. Fluorescence correlation spectroscopy with high count rate and low background: Analysis of translational diffusion. *Eur Biophys J*, 22(3):169–175, 1993.
- [33] R. Begley, A. B. Harvey, and R. Byer. Coherent anti-Stokes Raman spectroscopy. *Applied physics letters*, 25(7):387–390, 1974.
- [34] B. Berne and R. Pecora. Light Scattering as a Probe of Fast-Reaction Kinetics - Depolarized Spectrum of Rayleigh Scattered Light from a Chemically Reacting Medium. *J Chem Phys*, 50(2):783–&, 1969.
- [35] R. Pecora. Doppler Shifts in Light Scattering from Pure Liquids + Polymer Solutions. *J Chem Phys*, 40(6):1604–&, 1964.
- [36] W. Schrof, J. Klingler, S. Rozouvan, and D. Horn. Raman correlation spectroscopy: A method for studying chemical composition and dynamics of disperse systems. *Physical Review E - Statistical Physics, Plasmas, Fluids, and Related Interdisciplinary Topics*, 57(3 SUPPL. A):R2523–R2526, 1998.

Bibliography

- [37] N. Chandel and G. Budinger. The cellular basis for diverse responses to oxygen. *Free Radical Biology and Medicine*, 42(2):165–174, 2007.
- [38] R. Springett and H. Swartz. Measurements of oxygen in vivo: Overview and perspectives on methods to measure oxygen within cells and tissues. *Antioxidants and Redox Signaling*, 9(8):1295–1301, 2007.
- [39] J. Vanderkooi, G. Maniara, T. Green, and D. Wilson. An optical method for measurement of dioxygen concentration based upon quenching of phosphorescence. *Journal of Biological Chemistry*, 262(12):5476–5482, 1987.
- [40] J. Vanderkooi, W. Wright, and M. Erecinska. Oxygen gradients in mitochondria examined with delayed luminescence from excited-state triplet probes. *Biochemistry*, 29(22):5332–5338, 1990.
- [41] W. Xu. Oxygen sensors based on luminescence quenching: Interactions of metal complexes with the polymer supports. *Anal Chem*, 66(23):4133–4141, 1994.
- [42] P. Hartmann, M. Leiner, and M. Lippitsch. Luminescence quenching behavior of an oxygen sensor based on a Ru(II) complex dissolved in polystyrene. *Anal Chem*, 67(1):88–93, 1995.
- [43] J. Demas, B. DeGraff, and P. Coleman. Oxygen sensors based on luminescence quenching. *Anal Chem*, 71(23):793A–800A, 1999.
- [44] D. B. Papkovsky. New oxygen sensors and their application to biosensing. *Sensors and Actuators, B: Chemical*, B29(1-3):213–218, 1995.
- [45] O. Finikova, P. Chen, Z. Ou, K. Kadish, and S. Vinogradov. Dynamic quenching of porphyrin triplet states by two-photon absorbing dyes: Towards two-photon-enhanced oxygen nanosensors. *Journal of Photochemistry and Photobiology A: Chemistry*, 198(1):75–84, 2008.
- [46] O. Finikova, A. Lebedev, A. Aprelev, T. Troxler, F. Gao, C. Garnacho, S. Muro, R. Hochstrasser, and S. Vinogradov. Oxygen microscopy by two-photon-excited phosphorescence. *ChemPhysChem*, 9(12):1673–1679, 2008.
- [47] Y.-E. Koo, Y. Cao, R. Kopelman, S. Koo, M. Brasuel, and M. Philbert. Real-Time Measurements of Dissolved Oxygen Inside Live Cells by Organically Modified Silicate Fluorescent Nanosensors. *Anal Chem*, 76(9):2498–2505, 2004.
- [48] R. Evans, P. Douglas, J. Williams, and D. Rochester. A novel luminescence-based colorimetric oxygen sensor with a "traffic light" response. *Journal of Fluorescence*, 16(2):201–206, 2006.
- [49] H. Gerritsen, R. Sanders, A. Draaijer, C. Ince, and Y. Levine. Fluorescence lifetime imaging of oxygen in living cells. *Journal of Fluorescence*, 7(1):11–15, 1997.

-
- [50] D. Sud and M.-A. Mycek. Calibration and validation of an optical sensor for intracellular oxygen measurements. *Journal of Biomedical Optics*, 14(2):020506, 2009.
- [51] E. Mik, T. Johannes, C. Zuurbier, A. Heinen, J. Houben-Weerts, G. Balestra, J. Stap, J. Beek, and C. Ince. In vivo mitochondrial oxygen tension measured by a delayed fluorescence lifetime technique. *Biophysical Journal*, 95(8):3977–3990, 2008.
- [52] E. Mik, J. Stap, M. Sinaasappel, J. Beek, J. Aten, T. van Leeuwen, and C. Ince. Mitochondrial PO₂ measured by delayed fluorescence of endogenous protoporphyrin IX. *Nature Methods*, 3(11):939–945, 2006.
- [53] E. Mik, C. Ince, O. Eerbeek, A. Heinen, J. Stap, B. Hooibrink, C. Schumacher, G. Balestra, T. Johannes, J. Beek, A. Nieuwenhuis, P. van Horssen, J. Spaan, and C. Zuurbier. Mitochondrial oxygen tension within the heart. *Journal of Molecular and Cellular Cardiology*, 46(6):943–951, 2009.
- [54] T. Sandén, G. Persson, P. Thyberg, H. Blom, and J. Widengren. Monitoring kinetics of highly environment sensitive states of fluorescent molecules by modulated excitation and time-averaged fluorescence intensity recording. *Anal Chem*, 79(9):3330–41, 2007.
- [55] T. Sandén, G. Persson, and J. Widengren. Transient state imaging for microenvironmental monitoring by laser scanning microscopy. *Anal Chem*, 80(24):9589–9596, 2008.
- [56] J. Reece, L. A. Urry, M. L. Cain, S. A. Wasserman, P. V. Minorsky, and R. B. Jackson. Campbell biology - Ninth edition. Pearson Education Inc., 2011.
- [57] C. Kindig, K. Kelley, R. Howlett, C. Stary, and M. C. Hogan. Assessment of O₂ uptake dynamics in isolated single skeletal myocytes. *Journal of Applied Physiology*, 94(1):353–357, 2003.
- [58] K. Hassler, P. Rigler, H. Blom, R. Rigler, J. Widengren, and T. Lasser. Dynamic disorder in horseradish peroxidase observed with total internal reflection fluorescence correlation spectroscopy. *Optics Express*, 15(9):5366–5375, 2007.
- [59] P. Schwille, J. Bieschke, and F. Oehlenschläger. Kinetic investigations by fluorescence correlation spectroscopy: The analytical and diagnostic potential of diffusion studies. *Biophysical Chemistry*, 66(2-3):211–228, 1997.
- [60] S. Wennmalm, L. Edman, and R. Rigler. Conformational fluctuations in single DNA molecules. *Proceedings of the National Academy of Sciences of the United States of America*, 94(20):10641–10646, 1997.
- [61] L. Edman, Ü. Mets, and R. Rigler. Conformational transitions monitored for single molecules in solution. *Proceedings of the National Academy of Sciences of the United States of America*, 93(13):6710–6715, 1996.
- [62] J. R. Lakowicz. Principles of Fluorescence Spectroscopy. Springer, page 954, 2006.

Bibliography

- [63] P. Schwille, J. Korch, and W. Webb. Fluorescence correlation spectroscopy with single-molecule sensitivity on cell and model membranes. *Cytometry*, 36(3):176–182, 1999.
- [64] J. Korch, P. Schwille, W. Webb, and G. Feigenson. Characterization of lipid bilayer phases by confocal microscopy and fluorescence correlation spectroscopy. *Proc Natl Acad Sci USA*, 96(15):8461–8466, 1999.
- [65] C. Eggeling, C. Ringemann, R. Medda, G. Schwarzmann, K. Sandhoff, S. Polyakova, V. N. Belov, B. Hein, C. V. Middendorff, A. Schönle, and S. W. Hell. Direct observation of the nanoscale dynamics of membrane lipids in a living cell. *Nature*, 457(7233):1159–1162, 2009.
- [66] J. Strömquist, A. Chmyrov, S. Johansson, A. Andersson, L. Mäler, and J. Widengren. Quenching of Triplet State Fluorophores for Studying Diffusion-Mediated Reactions in Lipid Membranes. *Biophysical Journal*, 99(11):3821–3830, 2010.
- [67] N. Durand, C. Dellagiocoma, R. Goetschmann, A. Bertsch, I. Märki, T. Lasser, and P. Renaud. Direct observation of transitions between surface-dominated and bulk diffusion regimes in nanochannels. *Anal Chem*, 81(13):5407–5412, 2009.
- [68] J. Widengren, U. Mets, and R. Rigler. Fluorescence correlation spectroscopy of triplet states in solution: A theoretical and experimental study. *Journal of Physical Chemistry*, 99(36):13368–13379, 1995.
- [69] T. Hellerer, A. Schiller, G. Jung, and A. Zumbusch. Coherent anti-stokes Raman scattering (CARS) correlation spectroscopy. *ChemPhysChem*, 3(7):630–633, 2002.
- [70] J.-X. Cheng, E. O. Potma, and S. Xie. Coherent anti-Stokes Raman scattering correlation spectroscopy: Probing dynamical processes with chemical selectivity. *Journal of Physical Chemistry A*, 106(37):8561–8568, 2002.
- [71] B. Valeur. *Molecular Fluorescence: Principles and Applications*. Wiley-VCH, 2002.
- [72] N. Turro, V. Ramamurthy, and J. Scaiano. *Modern molecular photochemistry of organic molecules*. University Science Books, Sausalito, California, 2010.
- [73] G. Stokes. On the Change of Refrangibility of Light. *Philosophical Transactions of the Royal Society of London*, 142:463–562, 1852.
- [74] A. Jablonski. Über den Mechanismus der Photolumineszenz von Farbstoffphosphoren. *Zeitschrift für Physik*, 94(1-2):38–46, 1935.
- [75] J. Moser. Photochemistry (lecture notes). <http://photochemistry.epfl.ch/PC.html>, 2010.
- [76] D. R. Kearns. Physical and chemical properties of singlet molecular oxygen. *Chemical Reviews*, 71(4):395–427, 1971.

-
- [77] M. DeRosa and R. Crutchley. Photosensitized singlet oxygen and its applications. *Coordination Chemistry Reviews*, 233-234:351–371, 2002.
- [78] P. Ogilby. Singlet oxygen: There is indeed something new under the sun. *Chemical Society Reviews*, 39(8):3181–3209, 2010.
- [79] I. MacDonald and T. Dougherty. Basic principles of photodynamic therapy. *Journal of Porphyrins and Phthalocyanines*, 5(2):105–129, 2001.
- [80] P. Han and D. M. Bartels. Temperature dependence of oxygen diffusion in H₂O and D₂O. *Journal of Physical Chemistry*, 100(13):5597–5602, 1996.
- [81] P.-O. Gendron, F. Avaltroni, and K. J. Wilkinson. Diffusion Coefficients of Several Rhodamine Derivatives as Determined by Pulsed Field Gradient–Nuclear Magnetic Resonance and Fluorescence Correlation Spectroscopy. *Journal of Fluorescence*, 18(6):1093–1101, 2008.
- [82] S. Fischkoff and J. Vanderkooi. Oxygen diffusion in biological and artificial membranes determined by the fluorochrome pyrene. *Journal of General Physiology*, 65(5):663–676, 1975.
- [83] S. Chowdhury, V. Bhethanabotla, and R. Sen. Measurement of oxygen diffusivity and permeability in polymers using fluorescence microscopy. *Microscopy and Microanalysis*, 16(6):725–734, 2010.
- [84] D. M. Mackay. Diffusive oxygen emitters for enhancement of aerobic in situ treatment. *Ground Water Monitoring and Remediation*, 22(2):88–98, 2002.
- [85] L. Lindqvist. A Flash Photolysis Study of Fluorescein. *Arkiv . Kemi.*, 16(1-2):79–138, 1961.
- [86] J. Pawley. Handbook of biological confocal microscopy. Springer, 2006.
- [87] I. Gregor, M. Heupel, and E. Thiel. Precise fluorescence measurement for determination of photophysical properties of dyes. *Chemical Physics*, 272(2-3):185–197, 2001.
- [88] L. Song, C. A. G. O. Varma, J. Verhoeven, and H. J. Tanke. Influence of the triplet excited state on the photobleaching kinetics of fluorescein in microscopy. *Biophysical Journal*, 70(6):2959–2968, 1996.
- [89] A. Renn, J. Seelig, and V. Sandoghdar. Oxygen-dependent photochemistry of fluorescent dyes studied at the single molecule level. *Molecular Physics*, 104(3):409–414, 2006.
- [90] G. Donnert, C. Eggeling, and S. Hell. Major signal increase in fluorescence microscopy through dark-state relaxation. *Nature Methods*, 4(1):81–86, 2007.
- [91] G. Donnert, C. Eggeling, and S. Hell. Triplet-relaxation microscopy with bunched pulsed excitation. *Photochemical and Photobiological Sciences*, 8(4):481–485, 2009.

Bibliography

- [92] C. Eggeling, J. Widengren, R. Rigler, and C. A. M. Seidel. Photobleaching of Fluorescent Dyes under Conditions Used for Single-Molecule Detection: Evidence of Two-Step Photolysis. *Anal Chem*, 70(13):2651–2659, 1998.
- [93] J. Widengren and P. Schwille. Characterization of photoinduced isomerization and back-isomerization of the cyanine dye cy5 by fluorescence correlation spectroscopy. *Journal of Physical Chemistry A*, 104(27):6416–6428, 2000.
- [94] H. Blom, A. Chmyrov, K. Hassler, L. Davis, and J. Widengren. Triplet-state investigations of fluorescent dyes at dielectric interfaces using total internal reflection fluorescence correlation spectroscopy. *Journal of Physical Chemistry A*, 113(19):5554–5566, 2009.
- [95] A. Chmyrov. Photo-induced dark states in fluorescence spectroscopy – investigations & applications. Thesis, Royal Institute of Technology, Stockholm, Sweden, 2010.
- [96] R. Kubin and A. N. Fletcher. Fluorescence quantum yields of some rhodamine dyes. *Journal of Luminescence*, 27(4):455–462, 1982.
- [97] R. Menzel and E. Thiel. Intersystem crossing rate constants of rhodamine dyes: Influence of the amino-group substitution. *Chemical Physics Letters*, 291(1-2):237–243, 1998.
- [98] I. Arbeloa and P. Ojeda. Molecular forms of rhodamine B. *Chemical Physics Letters*, 79(2):347–350, 1981.
- [99] A. V. Deshpande and N. Iyer. Correlation of fluorescence and lasing properties in Eosin Y. *Journal of Luminescence*, 46(5):339–344, 1990.
- [100] A. Penzkofer, A. Beidoun, and M. Daiber. Intersystem-crossing and excited-state absorption in eosin Y solutions determined by picosecond double pulse transient absorption measurements. *Journal of Luminescence*, 51(6):297–314, 1992.
- [101] S. Linden and D. C. Neckers. Type I and type II sensitizers based on Rose Bengal onium salts. *Photochemistry and Photobiology*, 47(4):543–550, 1988.
- [102] P. Seybold, M. Gouterman, and J. Callis. Calorimetric, photometric and lifetime determinations of fluorescence yields of fluorescein dyes. *Photochemistry and Photobiology*, 9(3):229–242, 1969.
- [103] F. Stracke, M. Heupel, and E. Thiel. Singlet molecular oxygen photosensitized by Rhodamine dyes: Correlation with photophysical properties of the sensitizers. *Journal of Photochemistry and Photobiology A: Chemistry*, 126(1-3):51–58, 1999.
- [104] G. Patterson, R. Day, and D. Piston. Fluorescent protein spectra. *Journal of Cell Science*, 114(5):837–838, 2001.

-
- [105] S. Jakobs, V. Subramaniam, A. Schönle, T. Jovin, and S. Hell. EGFP and DsRed expressing cultures of *Escherichia coli* imaged by confocal, two-photon and fluorescence lifetime microscopy. *FEBS Letters*, 479(3):131–135, 2000.
- [106] R. E. Campbell, O. Tour, A. E. Palmer, P. A. Steinbach, G. S. Baird, D. A. Zacharias, and R. Y. Tsient. A monomeric red fluorescent protein. *Proc Natl Acad Sci USA*, 99(12):7877–7882, 2002.
- [107] E. M. Merzlyak, J. Goedhart, D. Shcherbo, M. E. Bulina, A. S. Shcheglov, A. F. Fradkov, A. Gaintzeva, K. A. Lukyanov, S. Lukyanov, T. T. W. J. Gadella, and D. M. Chudakov. Bright monomeric red fluorescent protein with an extended fluorescence lifetime. *Nature Methods*, 4(7):555–557, 2007.
- [108] N. C. Shaner, R. E. Campbell, P. A. Steinbach, B. N. G. Giepmans, A. E. Palmer, and R. Y. Tsient. Improved monomeric red, orange and yellow fluorescent proteins derived from *Discosoma* sp. red fluorescent protein. *Nature Biotechnology*, 22(12):1567–1572, 2004.
- [109] M. Geissbuehler, T. Spielmann, A. Formey, I. Märki, M. Leutenegger, B. Hinz, K. Johnson, D. V. D. Ville, and T. Lasser. Triplet imaging of Oxygen consumption during the contraction of a single smooth muscle cell (A7r5). *Biophysical Journal*, 98(2):339–349, 2010.
- [110] A. Korpel. Acousto-optics. Dekker, 1997.
- [111] H. G. Kapitzka. Microscopy from the very beginning. *Technical report*, Carl Zeiss Inc., 1–48, 2011.
- [112] F. Zernike. Phase contrast, a new method for the microscopic observation of transparent objects part II. *Physica*, 9(10):974–986, 1942.
- [113] F. Zernike. Phase contrast, a new method for the microscopic observation of transparent objects. *Physica*, 9(7):686–698, 1942.
- [114] T. Spielmann, H. Blom, M. Geissbuehler, T. Lasser, and J. Widengren. Transient state monitoring by total internal reflection fluorescence microscopy. *Journal of Physical Chemistry B*, 114(11):4035–4046, 2010.
- [115] J. Vogelsang, C. Steinhauer, C. Forthmann, I. H. Stein, B. Person-Skegro, T. Cordes, and P. Tinnefeld. Make them blink: Probes for super-resolution microscopy. *ChemPhysChem*, 11(12):2475–2490, 2010.
- [116] J. Vogelsang, R. Kasper, C. Steinhauer, B. Person, M. Heilemann, M. Sauer, and P. Tinnefeld. A reducing and oxidizing system minimizes photobleaching and blinking of fluorescent dyes. *Angewandte Chemie - International Edition*, 47(29):5465–5469, 2008.
- [117] I. R. Gatland and W. J. Thompson. Parameter bias elimination for log-transformed data with arbitrary error characteristics. *American Journal of Physics*, 61(3):269–272, 1992.

Bibliography

- [118] M. Leutenegger, H. Blom, J. Widengren, C. Eggeling, M. Gösch, R. Leitgeb, and T. Lasser. Dual-color total internal reflection fluorescence cross-correlation spectroscopy. *Journal of Biomedical Optics*, 11(4), 2006.
- [119] O. Stern and M. Volmer. The fading of fluorescence. *Phys Z*, 20:183–188, 1919.
- [120] L.-W. Lo, C. Koch, and D. Wilson. Calibration of oxygen-dependent quenching of the phosphorescence of Pd-meso-tetra (4-carboxyphenyl) porphine: A phosphor with general application for measuring oxygen concentration in biological systems. *Analytical Biochemistry*, 236(1):153–160, 1996.
- [121] D. Rehm and A. Weller. Kinetics of Fluorescence Quenching by Electron and H-Atom Transfer. *Israel J Chem*, 8(2):259–271, 1970.
- [122] J. Widengren, A. Chmyrov, C. Eggeling, P.-Å. Löfdahl, and C. A. M. Seidel. Strategies to improve photostabilities in ultrasensitive fluorescence spectroscopy. *Journal of Physical Chemistry A*, 111(3):429–440, 2007.
- [123] B. Kimes and B. Brandt. Characterization of 2 putative smooth muscle cell lines from rat thoracic aorta. *Experimental Cell Research*, 98(2):349–366, 1976.
- [124] A. Keppler, H. Pick, C. Arrivoli, H. Vogel, and K. Johnsson. Labeling of fusion proteins with synthetic fluorophores in live cells. *Proc Natl Acad Sci USA*, 101(27):9955–9959, 2004.
- [125] A. Keppler, S. Gendreizig, T. Gronemeyer, H. Pick, H. Vogel, and K. Johnsson. A general method for the covalent labeling of fusion proteins with small molecules in vivo. *Nature Biotechnology*, 21(1):86–89, 2003.
- [126] K. Takeda, H. Meyer-Lehnert, J. Kim, and R. Schrier. AVP-induced Ca fluxes and contraction of rat glomerular mesangial cells. *American Journal of Physiology - Renal Fluid and Electrolyte Physiology*, 255(1), 1988.
- [127] C. V. Renterghem, G. Romey, and M. Lazdunski. Vasopressin modulates the spontaneous electrical activity in aortic cells (line A7r5) by acting on three different types of ionic channels. *Proc Natl Acad Sci USA*, 85(23):9365–9369, 1988.
- [128] M. C. Hogan. Fall in intracellular Po₂ at the onset of contractions in *Xenopus* single skeletal muscle fibers. *Journal of Applied Physiology*, 90(5):1871–1876, 2001.
- [129] B. Alberts. Molecular biology of the cell. Garland Science - Taylor&Francis group, 2008.
- [130] G. Baravalle, D. Schober, M. Huber, N. Bayer, R. Murphy, and R. Fuchs. Transferrin recycling and dextran transport to lysosomes is differentially affected by bafilomycin, nocodazole, and low temperature. *Cell and Tissue Research*, 320(1):99–113, 2005.

-
- [131] E. Daro, P. V. D. Sluijs, T. Galli, and I. Mellman. Rab4 and cellubrevin define different early endosome populations on the pathway of transferrin receptor recycling. *Proceedings of the National Academy of Sciences of the United States of America*, 93(18):9559–9564, 1996.
- [132] J. Gruenberg and F. Maxfield. Membrane transport in the endocytic pathway. *Current Opinion in Cell Biology*, 7(4):552–563, 1995.
- [133] R. Ghosh, D. Gelman, and F. Maxfield. Quantification of low density lipoprotein and transferrin endocytic sorting in HEp2 cells using confocal microscopy. *Journal of Cell Science*, 107(8):2177–2189, 1994.
- [134] C. Eggeling, J. Fries, L. Brand, R. Günther, and C. A. M. Seidel. Monitoring conformational dynamics of a single molecule by selective fluorescence spectroscopy. *Proceedings of the National Academy of Sciences of the United States of America*, 95(4):1556–1561, 1998.
- [135] H. Kojima, N. Spataru, Y. Kawata, S.-I. Yano, and I. Vartires. Long-ranged electron interaction between carboxytetramethylrhodamine and fluorescein isothiocyanate bound covalently to DNA, as evidenced by fluorescence quenching. *Journal of Physical Chemistry B*, 102(49):9981–9984, 1998.
- [136] L. Wang, A. Gaigalas, J. Blasic, and M. Holden. Spectroscopic characterization of fluorescein- and tetramethylrhodamine- labeled oligonucleotides and their complexes with a DNA template. *Spectrochimica Acta - Part A: Molecular and Biomolecular Spectroscopy*, 60(12):2741–2750, 2004.
- [137] T. Heinlein, J.-P. Knemeyer, O. Piestert, and M. Sauer. Photoinduced electron transfer between fluorescent dyes and guanosine residues in DNA-hairpins. *Journal of Physical Chemistry B*, 107(31):7957–7964, 2003.
- [138] X. Li, R. Zhu, A. Yu, and X. Zhao. Ultrafast photoinduced electron transfer between tetramethylrhodamine and guanosine in aqueous solution. *Journal of Physical Chemistry B*, 115(19):6265–6271, 2011.
- [139] P. Qu, X. Chen, X. Zhou, X. Li, and X. Zhao. Fluorescence quenching of TMR by guanosine in oligonucleotides. *Science in China, Series B: Chemistry*, 52(10):1653–1659, 2009.
- [140] M. Scholl, Z. Kadlecova, and H.-A. Klok. Dendritic and hyperbranched polyamides. *Progress in Polymer Science (Oxford)*, 34(1):24–61, 2009.
- [141] S. Geissbuehler, C. Dellagiacoma, and T. Lasser. Comparison between SOFI and STORM. *Biomedical Optics Express*, Vol. 2, Issue 3, pp. 408–420, 2(3):408–420, 2011.
- [142] S. van de Linde, S. Wolter, M. Heilemann, and M. Sauer. The effect of photoswitching kinetics and labeling densities on super-resolution fluorescence imaging. *Journal of Biotechnology*, 149(4):260–266, 2010.

Bibliography

- [143] M. Heilemann, S. V. D. Linde, A. Mukherjee, and M. Sauer. Super-resolution imaging with small organic fluorophores. *Angewandte Chemie - International Edition*, 48(37):6903–6908, 2009.
- [144] E. Betzig, G. H. Patterson, R. Sougrat, O. W. Lindwasser, S. Olenych, J. S. Bonifacino, M. W. Davidson, J. Lippincott-Schwartz, and H. F. Hess. Imaging Intracellular Fluorescent Proteins at Nanometer Resolution. *Science*, 313(5793):1642–1645, 2006.
- [145] N. G. Gurskaya, V. Verkhusha, A. S. Shcheglov, D. B. Staroverov, T. V. Chepurnykh, A. F. Fradkov, S. Lukyanov, and K. A. Lukyanov. Engineering of a monomeric green-to-red photoactivatable fluorescent protein induced by blue light. *Nature Biotechnology*, 24(4):461, 2006.
- [146] D. M. Chudakov, V. V. Belousov, A. G. Zaraisky, V. V. Novoselov, D. B. Staroverov, D. B. Zorov, S. Lukyanov, and K. A. Lukyanov. Kindling fluorescent proteins for precise in vivo photolabeling. *Nature Biotechnology*, 21(2):191, 2003.
- [147] G. H. Patterson. A Photoactivatable GFP for Selective Photolabeling of Proteins and Cells. *Science*, 297(5588):1873–1877, 2002.
- [148] J. Widengren, R. Rigler, and U. Mets. Triplet-state monitoring by fluorescence correlation spectroscopy. *Journal of Fluorescence*, 4(3):255–258, 1994.
- [149] M. Leutenegger and T. Lasser. Detection efficiency in total internal reflection fluorescence microscopy. *Opt. Express*, 16(12):8519–8531, 2008.
- [150] A. M. Zheltikov. Coherent anti-stokes Raman scattering: From proof-of-the-principle experiments to femtosecond CARS and higher order wave-mixing generalizations. *Journal of Raman Spectroscopy*, 31(8-9):653–667, 2000.
- [151] P. Maker and R. Terhune. Study of optical effects due to an induced polarization third order in the electric field strength. *Phys. Rev.*, 137(3A):A801–A818, 1965.
- [152] W. Zipfel, R. Williams, R. Christiet, A. Y. Nikitin, B. T. Hyman, and W. Webb. Live tissue intrinsic emission microscopy using multiphoton-excited native fluorescence and second harmonic generation. *Proceedings of the National Academy of Sciences of the United States of America*, 100(12):7075–7080, 2003.
- [153] P. Campagnola, H. A. Clark, W. Mohler, A. Lewis, and L. Loew. Second-harmonic imaging microscopy of living cells. *Journal of Biomedical Optics*, 6(3):277–286, 2001.
- [154] P. Campagnola, M.-D. Wei, A. Lewis, and L. Loew. High-resolution nonlinear optical imaging of live cells by second harmonic generation. *Biophysical Journal*, 77(6):3341–3349, 1999.
- [155] C. Vinegoni, J. Bredfeldt, D. L. Marks, and S. Boppart. Nonlinear optical contrast enhancement for optical coherence tomography. *Optics Express*, 12(2):331–341, 2004.

-
- [156] B. E. Applegate, C. Yang, A. M. Rollins, and J. Izatt. Polarization-resolved second-harmonic-generation optical coherence tomography in collagen. *Optics Letters*, 29(19):2252–2254, 2004.
- [157] D. Yelin and Y. Silberberg. Laser scanning third-harmonic-generation microscopy in biology. *Optics Express*, 5(8):169–175, 1999.
- [158] J. Squier, M. Müller, G. J. Brakenhoff, and K. Wilson. Third harmonic generation microscopy. *Optics Express*, 3(9):315–324, 1998.
- [159] M. Müller, J. Squier, K. Wilson, and G. J. Brakenhoff. 3D microscopy of transparent objects using third-harmonic generation. *J Microsc*, 191(3):266–274, 1998.
- [160] Y. Barad, H. Eisenberg, M. Horowitz, and Y. Silberberg. Nonlinear scanning laser microscopy by third harmonic generation. *Applied Physics Letters*, 70(8):922–924, 1997.
- [161] R. Boyd. Nonlinear optics (chapter 1 and 2). Academic Press, 2008.
- [162] B. E. A. Saleh and M. C. Teich. Fundamentals of photonics (2nd Ed.). Wiley-Interscience, 2007.
- [163] V. Shcheslavskiy, S. Saltiel, A. Faustov, G. I. Petrov, and V. Yakovlev. Third-harmonic Rayleigh scattering: Theory and experiment. *Journal of the Optical Society of America B: Optical Physics*, 22(11):2402–2408, 2005.
- [164] J.-X. Cheng and X. Xie. Green’s function formulation for third-harmonic generation microscopy. *Journal of the Optical Society of America B: Optical Physics*, 19(7):1604–1610, 2002.
- [165] S. Fomichev, S. Popruzhenko, D. F. Zaretsky, and W. Becker. Laser-induced nonlinear excitation of collective electron motion in a cluster. *Journal of Physics B: Atomic, Molecular and Optical Physics*, 36(18):3817–3834, 2003.
- [166] S. Fomichev, S. Popruzhenko, D. F. Zaretsky, and W. Becker. Nonlinear excitation of the Mie resonance in a laser-irradiated cluster. *Optics Express, Vol. 14, Issue 1, pp. 260-269*, 11(19):2433–2439, 2003.
- [167] M. Polyanskiy. Refractive Index Database. <http://refractiveindex.info>, 2011.
- [168] G. M. Hale and M. R. Querry. Optical Constants of Water in the 200-nm to 200-um Wavelength Region. *Appl. Opt., AO*, 12(3):555–563, 1973.
- [169] A. Ashkin. Acceleration and Trapping of Particles by Radiation Pressure. *Physical Review Letters*, 24(4):156–159, 1970.
- [170] A. Ashkin. Forces of a single-beam gradient laser trap on a dielectric sphere in the ray optics regime. *Biophysical Journal*, 61(2 I):569–582, 1992.

Bibliography

- [171] F. Merenda. Micro-Optics for Multiple Laser Trapping in Microfluidics. Thesis, École Polytechnique Fédérale de Lausanne, Switzerland, 2008.
- [172] W. Wright, G. Sonek, and M. Berns. Parametric study of the forces on microspheres held by optical tweezers. *Applied Optics*, 33(9):1735–1748, 1994.
- [173] V. Petričević, S. Gayen, R. Alfano, K. Yamagishi, H. Anzai, and Y. Yamaguchi. Laser action in chromium-doped forsterite. *Applied Physics Letters*, 52(13):1040–1042, 1988.
- [174] V. Yanovsky, Y. Pang, F. Wise, and B. I. Minkov. Generation of 25-fs pulses from a self-mode-locked Cr:forsterite laser with optimized group-delay dispersion. *Optics Letters*, 18(18):1541–1543, 1993.
- [175] J.-C. Diels and W. Rudolph. Ultrashort laser pulse phenomena: fundamentals, techniques, and Applications on a Femtosecond Time Scale. Academic Press, 2006.
- [176] Femtolasers. Femtometer manual. *Technical report*, FEMTOLASERS Produktions GmbH, 1–18, 2000.
- [177] C. Spielmann, L. Xu, and F. Krausz. Measurement of interferometric autocorrelations: Comment. *Applied Optics*, 36(12):2523–2525, 1997.
- [178] J. Ries, M. Bayer, G. Csúcs, R. Dirkx, M. Solimena, H. Ewers, and P. Schwille. Automated suppression of sample-related artifacts in fluorescence correlation spectroscopy. *Optics Express*, 18(11):11073–11082, 2010.
- [179] T. Spielmann. Triplet Imaging by Modulated Excitation, a novel technique to image living cells. Master’s thesis, École Polytechnique Fédérale de Lausanne, Switzerland, 2008.
- [180] M. Leutenegger. Single molecule detection on surfaces. Thesis, École Polytechnique Fédérale de Lausanne, Switzerland, 2007.
- [181] A. G. 3rd Palmer and N. Thompson. Molecular aggregation characterized by high order autocorrelation in fluorescence correlation spectroscopy. *Biophysical Journal*, 52(2):257–270, 1987.
- [182] I. Steinberg. On the time reversal of noise signals. *Biophysical Journal*, 50(1):171–179, 1986.
- [183] M. Geissbuehler, S. Geissbuehler, and T. Lasser. Nonlinear Correlation Spectroscopy (NLCS) Theory. <http://infoscience.epfl.ch/record/167573>, 2011.
- [184] W. Swanson and J. Cohen. Color vision. *Ophthalmology Clinics of North America*, 16(2):179–203, 2003.
- [185] M. Simunovic. Colour vision deficiency. *Eye*, 24(5):747–755, 2010.

Matthias Geissbühler



matthias.geissbuehler@a3.epfl.ch
Born on 28.9.1981 in Bern, Switzerland
Swiss nationality

Education

- | | |
|-----------|---|
| 2007-2011 | Ph.D. thesis in biomedical optics
Laboratoire d'Optique Biomédicale LOB, Prof. Theo Lasser
Swiss Federal Institute of Technology (EPFL), Lausanne |
| 2001-2006 | Master in Micro technology, specialization in Applied Photonics
Swiss Federal Institute of Technology (EPFL), Lausanne
Exchange year at the Indian Institute of Technology Delhi (IITD) |
| 1997-2001 | Gymnasium Langenthal |

Experience and projects

- | | |
|----------------|---|
| 2006 (6months) | Phonak Group, China
Management internship (marketing, sales, finance) |
| 2005-2006 | Master-Project "High Resolution Optical Microscopy"
Laboratoire d'Optique Biomédicale LOB, Prof. Theo Lasser
Swiss Federal Institute of Technology (EPFL), Lausanne |
| 1997-2001 | Web design freelancer
Commercial web design
(Project management, team work, development)
Thinkquest-contest participation
„Start your engines!“ – Winning team (2000, CH) |

Teaching and Supervision

- 2007-2010 Teaching assistant in biomicroscopy lecture for Life Science Master students
- 2007-2009 Supervision of two master projects and four semester projects
- 2005 Teaching assistant in laboratory course on electrical engineering

Publications (peer-reviewed)

M. Geissbuehler, T. Spielmann, A. Formey, I. Märki, M. Leutenegger, B. Hinz, K. Johnsson, D. Van De Ville, and T. Lasser. Triplet Imaging of Oxygen Consumption During the Contraction of a Single Smooth Muscle Cell (A7r5). *Biophysical Journal*, 98 (2): 339–349, 2010.

M. Geissbuehler, T. Spielmann, A. Formey, I. Märki, M. Leutenegger, B. Hinz, K. Johnsson, D. Van De Ville, and T. Lasser. Triplet Imaging of Oxygen Consumption During the Contraction of a Single Smooth Muscle Cell (A7r5). *Advances in Experimental Medicine and Biology – International Society on Oxygen Transport to Tissue (ISOTT) conference 2010*, in-press.

T. Spielmann, H. Blom, M. Geissbuehler, T. Lasser, and J. Widengren. Transient State Monitoring by Total Internal Reflection Fluorescence Microscopy. *Journal of Physical Chemistry B*, 114(11):4035–4046, 2010.

Patent

S. Geissbuehler, C. Dellagiacomma, M Leutenegger, M. Geissbuehler, and T. Lasser. Cumulant Microscopy. *European patent* EP 11169880.9 (pending).

Conference contributions

M. Geissbuehler, N. Bocchio, V. Shcheslavskiy, M. Leutenegger, L. Bonacina, C. Kasparian, I. Märki, J.-P. Wolf, and T. Lasser, Characterization of Nanoparticles Using Non-linear Correlation Spectroscopy. Talk presented at *ECBO 2011 – Emerging Technologies: Models and Platforms II*, Munich, Germany, May 22-26, 2011.

M. Geissbuehler, Z. Kadlecova, I. Märki, M. Matasci, D. Van De Ville, H.-A. Klok, and T. Lasser. Assessing the cellular uptake pathway for poly-Lysine analogues using triplet lifetime imaging. Poster presented at *Biophysical Society 55th Annual Meeting*, Baltimore, Maryland, USA, March 5-9, 2011.

M. Geissbuehler, T. Spielmann, A. Formey, I. Maerki, B. Hinz, K. Johnsson, D. Van de Ville, and T. Lasser. Monitoring Oxygen Consumption during Cell Contraction by Triplet State Imaging. Talk presented at *ECBO 2009 – Advanced Microscopy Techniques*, Munich, June 14-18, 2009.

M. Geissbuehler, T. Spielmann, A. Formey, I. Maerki, B. Hinz, D. Van de Ville, and T. Lasser. Triplet State Imaging. Talk presented at *BiOS 2009 – Three-Dimensional and Multidimensional Microscopy: Image Acquisition and Processing XVI*, San Jose, CA, USA, January 24-29, 2009.

M. Geissbuehler, T. Spielmann, I. Märki, A. Formey, A. Gautier, B. Hinz, K. Johnsson, D. Van De Ville, and T. Lasser. Triplet Imaging by Modulated Excitation. Poster presented at *14th International Workshop on "Single Molecule Spectroscopy and Ultra Sensitive Analysis in the Life Sciences"*, Berlin-Adlershof, Germany, September 17-19, 2008.

M. Geissbuehler, T. Spielmann, R. Vulliamy, M. Leutenegger, I. Märki, T. Sandén, G. Persson, B. Hinz, J. Widengren, and T. Lasser. Triplet imaging contrast by modulated excitation. Talk presented at *BiOS 2008 – Three-Dimensional and Multidimensional Microscopy: Image Acquisition and Processing XV*, San Jose, CA, USA, January 19-24, 2008.

M. Geissbuehler, T. Lasser, and R. A. Leitgeb. k-Microscopy: resolution beyond the diffraction limit. Talk presented at *BiOS 2008 – Three-Dimensional and Multidimensional Microscopy: Image Acquisition and Processing XV*. Poster presented at *Coherence Domain Optical Methods and Optical Coherence Tomography in Biomedicine XII*, San Jose, CA, USA, January 19-24, 2008.

Technical skills

Programming: Matlab, LabVIEW, Java, PHP, C, Mathematica, Assembler, AppleScript, BASIC
Miscellaneous: Zemax, Pro/E, Adobe Illustrator, Photoshop & InDesign, LaTeX, FileMaker, MySQL, iWork, MS Office

Languages

Swiss German: Native language
German: fluent
French: fluent (language of my studies in Lausanne, Switzerland)
English: fluent (language of my studies in Delhi, India)
Mandarin: learning (beginner level)

Extra-professional activities

Theater: Stage performances with several teams in German, French and English (1997 –2009)

Music: Singing lessons at the Conservatory of Lausanne (since 2001), Opera class lessons and performances at Institut de Ribeaupierre, Lausanne (2009-2011)

Travelling, foreign cultures, photography, cross-country skiing